Dissertation

submitted to the
Combined Faculty of Mathematics, Engineering and Natural Sciences
of Heidelberg University, Germany
for the degree of
Doctor of Natural Sciences

Put forward by

Tobias Engelhardt, M.Sc.

born in Heidelberg, Germany
Date of the oral examination: 17 December 2021

MINFLUX Nanoscopy with Interferometric Approach

Referees: Prof. Dr. Dr. h. c. mult. Stefan W. Hell
Prof. Dr. Joachim Spatz

Zusammenfassung

Die Verfolgung fluoreszenter Einzelmoleküle ist ein unverzichtbares Instrument in den Biowissenschaften, da sie ein unübertroffenes Potenzial zur Beobachtung und Untersuchung der funktionellen Dynamik (makro-)molekularer Mechanismen in lebenden Zellen auf minimal invasive Weise bietet. Der begrenzende Faktor für die räumlich-zeitliche Auflösung solcher Studien ist in der Regel die begrenzte Photonenemissionsrate einzelner fluoreszierender Moleküle. In dieser Arbeit wird untersucht, inwieweit die bemerkenswerte Lokalisierungseffizienz der MINFLUX-Nanoskopie eine höhere räumlich-zeitliche Auflösung als herkömmliche, nicht beugungsbegrenzte Ansätze zur Einzelmolekülverfolgung ermöglicht, um bisher unauflösbare subzelluläre Dynamiken aufzudecken. Zu diesem Zweck wurde der Phasenscanner entwickelt und gebaut. Er ermöglicht die interferometrische Erzeugung und das hochpräzise Verschieben verschiedener Punktspreizungsfunktionen durch elektrooptische Steuerung der Phasenverschiebung zwischen gegenseitig kohärenten Teilstrahlen, die in der hinteren Brennebene eines Mikroskopobjektivs angeordnet sind. Es wurden MINFLUX-Lokalisierungen aufgenommen, die die räumlich-zeitliche Auflösung einer idealisierten kamerabasierten Lokalisierung um mehr als das Sechsfache übertreffen. Die beispiellose Leistung des vorgestellten MINFLUX-Mikroskops wurde durch die, zum ersten Mal unter physiologischen Bedingungen mögliche Verfolgung von Kinesin-1-Motorproteinen mit fluoreszenten Einzelmolekülen demonstriert. Die Ergebnisse zeigen, dass MINFLUX die leistungsfähigste Technik ist, wenn bei der Verfolgung von Einzelmolekülen die höchste räumliche und zeitliche Auflösung erforderlich ist.

Abstract

Single molecule tracking is an indispensable tool in life sciences due to its unmatched potential to observe and investigate functional dynamics of (macro)molecular machineries in living cells in a minimally invasive manner. The limiting factor for the spatio-temporal resolution of such studies is typically the finite photon emission rate of fluorescent single molecules. This work assesses to which extent the remarkable localization efficiency of MINFLUX nanoscopy allows for a higher spatio-temporal resolution than conventional super-resolution tracking approaches to reveal previously unresolvable subcellular dynamics. To this end, the phase scanner, an innovative scanning device was designed and built. It allows to interferometrically generate and scan various point spread functions by electro-optically controlling the phase shift between mutually coherent beamlets arranged in the back focal plane of a microscope objective. MINFLUX localizations were recorded that outperform the spatio-temporal resolution of an idealized camera-based localization by more than a factor of six. The unprecedented performance of the presented MINFLUX microscope was demonstrated by tracking Kinesin-1 motor proteins for the first time under physiological conditions in a single molecule tracking study. With these results, MINFLUX emerges as the most powerful technique when the highest spatio-temporal resolution is required in single molecule tracking studies.

Contents

List of Abbreviations

1D	one dimension
2D	two dimensions
3D	three dimensions
APD	avalanche photodiode
BFP	back focal plane
CW	continuous wave
EBP	excitation beam pattern
EMCCD	electron multiplying charge-coupled device
EOD	electro optic deflector
FOV	field of view
FPGA	field programable gate array
FWHM	full width at half maximum
GSD	ground state depletion
HM-PSF	half moon PSF
IR	infrared
NA	numerical aperture
OPL	optical path length
PAINT	points accumulation for imaging in nanoscale topography
PALM	photo-activated localization microscopy
PSF	point spread function
QY	quantum yield
RESOLFT	reversible saturable optical fluorescence transitions
ROI	region of interest
RTP	rubidium titanyl phosphate
SBR	signal-to-background ratio
SLM	spatial light modulator
SMT	single molecule tracking
STED	stimulated emission depletion
STORM	stochastic optical reconstruction microscopy
STR	spatio-temporal resolution
TEM	transverse electromagnetic mode

Chapter 1

Introduction

Light microscopy continues to be an essential tool for biological and medical research as it enables the systematic study of cellular dynamics at the microscopic level. Combined with an extensive array of available orthogonal labeling and staining techniques, light microscopy facilitates the detailed analysis of cellular components *in vivo*.

In general, the stronger the resolving power of a microscope, the smaller the features which can be distinguished. However, the ability to gain insight into decisive processes and mechanisms is dependent on the capability to visualize *all* relevant elements in action. As a result of technical and methodological developments, the limit of what can be resolved and made visible by light microscopy has been substantially driven forward in the last decades. Of particular significance was the development of stimulated emission depletion microscopy (STED) in 1994, which demonstrated for the first time that the previously thought to be unbreakable diffraction limit, originally formulated by Abbe in 1873, could be overcome [1–3]. In 2006, an alternative diffraction surpassing super-resolution microscopy methodology emerged when photoactivated localization microscopy (PALM) and related techniques were invented [4–6]. These advances substantially impact biological research as features separated by a distance smaller than about half the wavelength of the excitation light were now able to be resolved.

In principal, there is no physical limit to the achievable resolution with the above-mentioned super-resolution methods. The resolution STED microscopy offers is limited by dye molecules and their resistance to photobleaching under repeated excitation and deexcitation. The precision σ with which the position of an emitter detected on camera can be determined scales with one over the square root of the number of photons N that are collected [7–10].

$$\sigma \propto \frac{1}{\sqrt{N}} \tag{1.1}$$

In practice, the barrier is set by the stability and brightness of the fluorescent dyes that are used to label the complex of interest. As a consequence, brighter dyes and anti-bleaching agents were developed that pushed the boundary further [11–13]. Still, the localization efficiency, meaning the number of photons that must be collected to reach a certain precision, prevents these methods from routinely achieving single digit nanometer resolution.

In another landmark development for the field, the introduction of 'Nanometer Resolution Imaging and Tracking of Fluorescent Molecules with Minimal Photon Fluxes' (MINFLUX) in 2019 further improved the attainable resolution down to single digit nanometer resolution [14]. The technique is able to achieve these unprecedented resolutions due to its much higher localization efficiency compared to all other known fluorescence microscopy techniques. It realizes this by using a beam intensity distribution that features a local minimum and employing a variable sequence of structured excitations. Specifically, the beam is shifted around the molecule position by steps of L/2 and the position is calculated from the relative differences in the count of photons collected during the different exposures. The localization precision in the center of the exposure pattern σ is then described by

$$\sigma = \frac{L}{4\sqrt{N}}. \tag{1.2}$$

This constitutes a paradigmatic shift in fluorescence microscopy because the strict relationship between the number of collected photons and the localization precision is broken up. Because of the inverse square root law, conventional methods demand a quadratically increasing number of photons to improve the localization precision further. With each additional photon detected the information content that the next detected photon carries gets less and less. In contrast to that, by decreasing L, MINFLUX is able to render each detected photon more informative. Iterative MINFLUX takes advantage of this fact during the localization of an emitter by decreasing L after a certain localization precision is achieved [15].

In this context, the aim of this work was to investigate to which extent the MINFLUX principle is theoretically and practically able to make more efficient use of the valuable detected photons to increase the achievable spatial and temporal resolution. Due to its novelty the main challenges of MINFLUX are still not clear. New classes of dyes might emerge as more favorable probes for biological studies, because new excitation and measurement schemes are employed.

The MINFLUX setups that were published until now are bulky and highly complex apparatuses [14, 16, 17]. To fathom the limits of the achievable localization efficiency, a simplified, yet with optimal preconditions in mind designed optical setup was required.

Thus, a MINFLUX setup with a new architecture was envisioned. Through simplification and redesign of core components a compact optical setup was constructed. To omit the need for separate beam shaping and scanning devices the phase scanner was developed. By overlapping multiple beamlets with controllable amplitude and phase in the focal plane, the phase scanner generates and scans various point spread functions (PSF) with nanometric precision on a microsecond timescale. Because the optical components can easily adapt to arbitrary wavelengths in the visible spectrum by electro-optic phase control, only a single beam path for all wavelengths was necessary. This enabled the design of a compact beam path that has a low susceptibility to environmental influences. At the same time, the phase scanner's physical concept delivers the best preconditions to optimize the localization efficiency and the achievable spatio-temporal resolution.

The resulting localization efficiency of our implementation of MINFLUX was higher than for any conventional super-resolution microscopy technique. The increased localization efficiency and therefore increased spatio-temporal resolution was highlighted by multiple single molecule tracking experiments. As proof-of-principle, tracking experiments on individual fluorophores that were moved by a motorized sample stage were conducted. In this experiment, a lateral localization precision of two nanometers in under one millisecond was achieved. Additionally, the stepping behavior of DNA origami nanorobots, that moved over a grid of discrete binding positions was investigated. In further experiments the movement of Kinesin-1 motor proteins along microtubules was studied. Previously, the stepping behavior of kinesin had to be slowed down in order to reach the necessary spatial resolution to detect discrete steps with fluorescence microscopes [18]. However using the setup described herein, the first fluorescence-based tracking experiments of kinesin at physiological ATP concentrations are shown.

1.1 Diffraction Limit

When experimenting with diffraction gratings Ernst Abbe discovered in 1873, that due to the nature of diffraction there is a fundamental limit to the minimal structure size that can be resolved by focusing light [1]. For a conventional light microscope this means when illuminating with light with wavelength λ, structures that are smaller than

$$d = \frac{\lambda}{2n \sin \alpha} = \frac{\lambda}{2NA} \tag{1.3}$$

cannot be discerned. Here, n is the refractive index of the immersion medium and α the half-opening angle of the microscope objective. The numerical aperture (NA) is defined as the product of these two quantities.

1.2 Basics of Super-Resolution Microscopy

The diffraction limit was overcome by the previously mentioned super-resolution microscopy techniques. All these methods have in common that they involve a scheme to switch fluorophores in close vicinity on or off such that only a sub-ensemble or a single molecule is emitting at a time. The way in which the position of these single emitters is established differs for coordinate-targeted and coordinate-stochastic methods [19].

1.2.1 Coordinate-Targeted Super-Resolution Microscopy

Coordinate-targeted methods utilize a spatially shaped deexcitation or deactivation beam featuring a local intensity minimum. By the sequence of unstructured excitation and structured deexcitation/activation only molecules that are close to the local minimum of the beam stay in an excitable state and are able to fluoresce [20]. As the position of the minimum is known, the collected fluorescence light can only emerge from this region. The precision with which the origin of the detected photons is known depends on the effective width of the emitter distribution in the on-state after the deexcitation or deactivation beam has illuminated a previously excited area. The resolution σ can be approximated by

$$\sigma = \frac{\sigma_{PSF}}{\sqrt{1 + I/I_s}} \tag{1.4}$$

with σ_{PSF} being the standard deviation of the Gaussian approximating the diffraction spot, I being the intensity of the deexcitation beam and I_s describing intensity at which the probability to deexcite an excited molecule is 0.5 [19, 21]. Other members of the family of coordinate-targeted methods like STED are reversible saturable optical fluorescence transitions (RESOLFT) and ground state depletion microscopy (GSD) [2, 22].

1.2.2 Coordinate-Stochastic Super-Resolution Microscopy

In contrast to coordinate-targeted approaches, coordinate-stochastic methods are based on calculating the centroid of a diffraction spot caused by focusing the collected light from an emitter on a camera. By adjusting the experimental parameters, such as the activation illumination scheme and intensity as well as the imaging buffer composition, the density of molecules in an excitable state is held low enough to have on average not more than one in an area of the size of a diffraction spot. Coordinate-stochastic methods comprise the mentioned PALM, but also stochastic optical reconstruction microscopy (STORM),

its variant direction stochastic optical reconstruction microscopy (dSTORM) as well as points accumulation for imaging in nanoscale topography (DNA-PAINT) [23, 24]. For these techniques, in an idealized case, the localization precision σ for a single emitter can be described by

$$\sigma = \frac{\sigma_{PSF}}{\sqrt{N}} \tag{1.5}$$

with σ_{PSF} being the standard deviation of the Gaussian approximating the PSF, and N describing the number of collected photons forming a diffraction spot [10]. The inverse square root law that governs conventional super-resolution techniques indicates that a slight improvement over the diffraction limited precision is possible with few collected photons. Large gains of localization precision, however, must be paid with an quadratically rising cost of fluorescence photons. Because the number of fluorescence photons is limited due to bleaching and transient molecular dark states, in practice a localization precision of 20-30 nm is rarely exceeded. To overcome this obstacle, considerable effort has been invested into the development of optimized imaging buffers and modified fluorescent dyes [11–13]. Until the advent of MINFLUX however, the underlying problem of limited localization efficiency was untouched [14].

1.3 The MINFLUX Localization Concept

In this section, an overview over the working principle of the single emitter localization scheme named MINFLUX will be given. The acronym can stand for 'Nanometer Resolution Imaging and Tracking of Fluorescent Molecules with Minimal Photon Fluxes', minimal emission fluxes by probing with a minimum of excitation light or alternatively maximally informative luminescence excitation probing [14]. First, the previously reported working principle will be explained. Subsequently, the theoretical considerations of an alternative approach to perform MINFLUX localizations in multiple spatial dimensions will be described. To illustrate the concept more closely in tune with reality the case of background limited localizations will treated and briefly compared to the performance of camera-based localization methods.

1.3.1 MINFLUX's Operating Principle Improves Localization Efficiency

As mentioned previously, the strategies to localize a fluorophore in space with a precision higher than the diffraction limit allows are typically categorized into coordinate-targeted and coordinate-stochastic methods (see Section 1.2). MINFLUX is a novel concept in which the stochastic nature of camera-based localization methods and the coordinate-targeted approach of STED are combined to increase the localization efficiency. It utilizes a beam featuring a local intensity minimum to localize single fluorophores. Because the minimum is iteratively centered on the emitter position the fluorophore is rarely probed with high intensities. Paradoxically, the molecule's position is best known when it emits no photons i.e. the molecule is located exactly in the minimum of the PSF.

The established method from Balzarotti et al employs a 2D donut shaped PSF or a 3D PSF generated by a so called top-hat phase mask [14–16, 25]. To localize the emitter, the beam with a local intensity minimum in two or three dimensions is positioned sequentially at various positions around the estimated molecule location. A maximum likelihood estimator tailored to the problem is used to calculate the most probable position from the detected photon counts. The center of the pattern is then shifted to the newly calculated position estimate and the procedure is repeated until either enough photons are collected, or the emitter is photo-bleached. In this work, a new approach where the localization of an emitter is carried out by a sequence of 1D localizations will be established. To do so, PSFs featuring a local minimum in only one of the spatial directions are created. This approach will be discussed in the following sections and is shown in Figure 1.1.

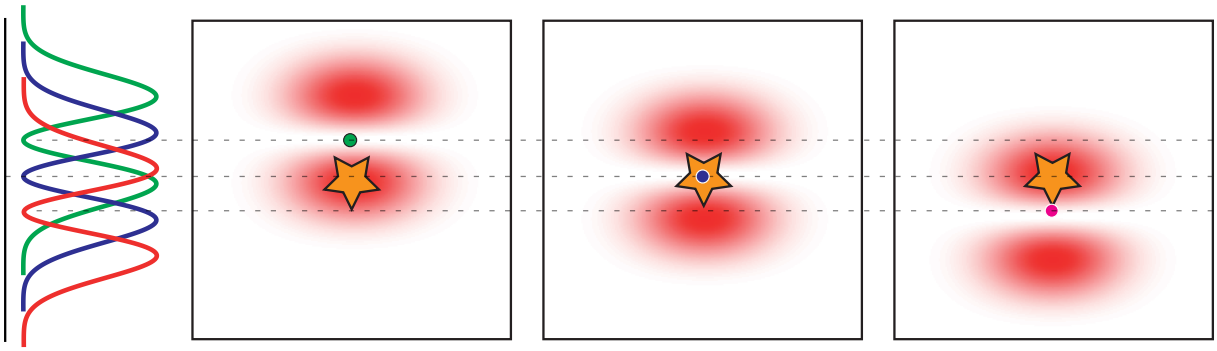

Figure 1.1: 1D localization scheme with minimum along one direction The sketch shows the 1D MINFLUX localization procedure that is introduced in this work. The lateral position is established by subsequent 1D localizations with a PSF featuring an intensity minimum along one spatial dimension. Such a 1D localization is carried out by positioning the beam in an excitation beam pattern featuring three different positions around the estimated location of the emitter. This is in contrast to the established approach where a PSF with a 2D minimum is moved in pattern that establishes x- and y-coordinate simultaneously. For visualization purposes, the size of the spatial shift L is displayed exaggerated. In practice the displacement is held as small as possible.

1.3.2 Multidimensional Localization by Subsequent 1D Localizations

In this subsection the theoretical framework of localizing an emitter in two dimensions by employing two 1D localizations will be described. One advantage of this approach is the simplified position calculation from the collected photon counts. It will be demonstrated, that instead of a complicated estimator, like for the 2D case, the position estimate will be a simple, analytic expression. This will enable us to implement the position calculation in hardware for true real-time measurement control.

In principle localizations employing the MINFLUX principle can be carried out with any beam featuring a local intensity minimum [14]. If an emitter is probed twice with excitation beams with a spatial shift of L relative to each other a certain number of photons will be collected for both exposures. Neglecting background, the number of fluorescence photons will only depend on molecule parameters e.g. the quantum yield and the fluorescence lifetime and will be proportional to the excitation intensity at the molecules position.

$$N \propto C(QY, \tau, ...) \cdot I(x_m) \tag{1.6}$$

As the intensity for the two exposures will vary, in general the numbers of photons that are collected will be different. If the intensity distribution of the excitation beam is known, the molecule position can be deduced relative to the excitation beam pattern from the fluorescence counts as good as the Poissonian photon statistics allow.

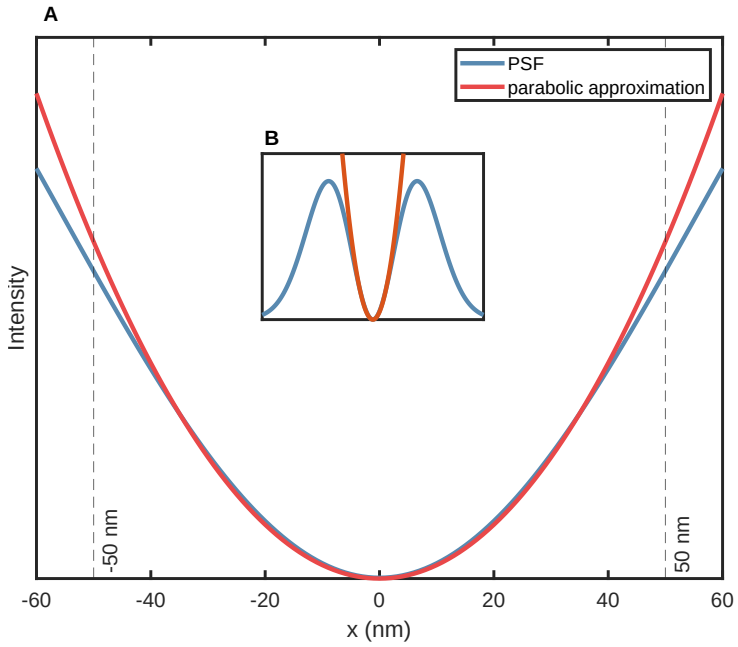

Figure 1.2: Parabolic approximation of range around PSFs minimum A shows the magnified view of **B**. The figure displays the strong similarity between the actual PSF and the parabolic approximation in range of roughly ±50 nm around the intensity minimum. It is therefore valid to use this approximation for further calculations.

In the following derivation the profile of the PSF in 1D will be approximated by a parabolic profile. The similarity of the experimental PSF and the parabolic approximation is depicted in Figure 1.2. **A** displays a magnified view of the overview in **B**. It shows that for distances smaller than 50 nm from the minimum position the PSF can be approximated very well by a parabola. Consequently, utilizing this approximation in the following calculations is valid because we will be only concerned with this range due to the iterative zoom in process. The deviation arising from the simplification is therefore negligible in this treatment. Unless noted otherwise, the calculations in the remainder of this chapter will be carried out under assumption of this approximation.

The intensity at a certain position x relative to center position x_0 of the parabola can be described by:

$$I(x) = a(x - x_0)^2 \tag{1.7}$$

The molecule at position x_m is first excited with the parabolic intensity profile at position x_1. The detected photon counts are then described by y_1. The parabolic profile is then shifted by a distance of L and fluorescence counts y_2 are collected for the second exposure. The position of the fluorophore can then be described as

$$x_m = \frac{L}{2}\frac{1+\sqrt{\frac{y_1}{y_2}}}{1-\sqrt{\frac{y_1}{y_2}}} = \frac{L}{2}\frac{2}{\sqrt{\frac{y_1}{y_2}}+1} - 1. \tag{1.8}$$

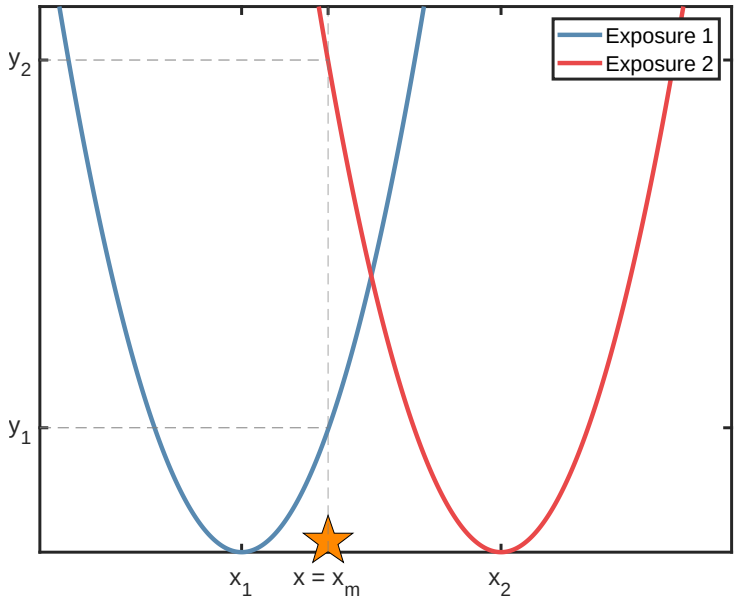

Figure 1.3: Sketch of 1D MINFLUX localization with two parabolic exposures When a MINFLUX localization is performed with two parabolic exposures at the positions x_1 and x_2 with a separation of L, the collected counts y_1 and y_2 can be described by equation 1.7.

Note that the expression for the molecule position scales linearly with the separation of the two exposures L. Independent of the number of counts that are collected and other parameters of the parabolas the uncertainty σ_{x_m} will therefore be proportional to L.

$$\sigma_{x_m} \propto L \tag{1.9}$$

This means, unlike in conventional super-resolution techniques, MINFLUX offers a possibility to increase the precision of localizations other than collecting more fluorescence photons.

1.3.3 Expansion to a Treatment Including Background

In a real-world situation, the measurement will be impacted by background photons for example photons entering the microscope objective from outside the sample, dark counts from the photon detectors or abberated excitation PSFs. To take the effect of background on the position calculate into account and make the localization more robust, the described concept will be expanded by adding a third exposure. During the additional exposure the excitation beam is pointed at the current estimated molecule position to gain more knowledge about the background and the actual molecule position. This allows to calculate the Signal-to-background ratio (SBR) of a specific localization and therefore enables the assessment of the quality of the localization. Reasons for a decreased localization precision can be for example increased local background or dyes in the imaging

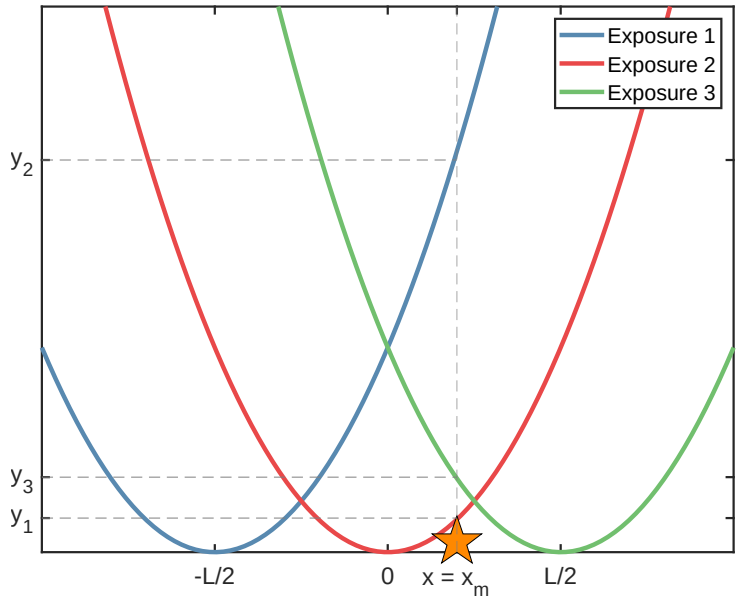

Figure 1.4: 1D MINFLUX localization scheme expanded to a third exposure By expanding the 1D Localization to three consecutive exposures at the positions $-\frac{L}{2}$, 0 and $-\frac{L}{2}$ additional information about the SBR of the individual measurement can be gained. This allows to evaluate the quality of the localization, removes ambiguities of the position calculation and makes the localization result more robust against statistical outliers.

medium diffusing through the focal volume. Using the third exposure, it is also possible to examine whether the position extracted by the MINFLUX localization converged on the actual molecule position and to discern if there was a single, or multiple emitters in the diffraction limited area. It additionally removes ambiguities in the final molecule position that can arise if the molecule position is probed with a local minimum of a low intensity sidelobe of the beam.

The molecule is now excited three times with the excitation profile shifted by L/2 after each exposure. Assuming a parabolic profile, the collected photon counts at position x for an exposure with center position x_0 can be described as

$$y = a(x - x_0)^2 + b \tag{1.10}$$

Here, a describes the curvature of the parabola which will depend on the excitation intensity and the molecule parameters C. The offset of the fluorescence counts that can arise from background photons is described by b.

The fluorescence counts that are collected for the three exposures can be described by:

$$y_1 = a(x_m - \frac{L}{2})^2 + b$$
$$y_2 = ax_m^2 + b$$
$$y_3 = a(x_m + \frac{L}{2})^2 + b$$

By solving the equation system after x_m we get the expression

$$x_m = \frac{L}{4}\frac{y_3 - y_1}{y_3 - 2y_2 + y_1} \tag{1.11}$$

for the molecule position x_m.

The uncertainty of the position estimate σ_{x_m} is the localization precision that is attainable with this measurement scheme. It can be calculated by applying Gaussian error propagation:

$$\sigma_{x_m} = \sqrt{\left(\frac{\partial x_m}{\partial y_1}\sigma_{y_1}\right)^2 + \left(\frac{\partial x_m}{\partial y_2}\sigma_{y_2}\right)^2 + \left(\frac{\partial x_m}{\partial y_3}\sigma_{y_3}\right)^2} \tag{1.12}$$

Calculating the partial derivatives of equation 1.11 and inserting it into 1.12 leads to the expression

$$\sigma_{x_m} = \frac{L}{2}\frac{\sqrt{(y_3 - y_2)^2 y_1 + (y_1 - y_3)^2 y_2 + (y_2 - y_1)^2 y_3}}{(y_1 - 2y_2 + y_3)^2} \tag{1.13}$$

Under the assumption that the molecule is positioned close to the center of the second exposure at position $x_0 = 0$, y_1 can be approximated by $y_1 \approx y_3$. When the molecule is centered and the background close to zero, y_2 can be approximated by $y_2 \approx 0$. When the sum of the fluorescence counts is written as $y_1 + y_3 = N$, the expression for the localization precision σ at the center of the FOV is

$$\sigma_{x_m} = \frac{L}{4\sqrt{N}} \tag{1.14}$$

The same equation can be derived in the multidimensional calculation shown in Reference [14]. This equation shows the central paradigm shift of the MINFLUX localization scheme in comparison to the established super-resolution microscopy techniques. The localization precision does not only depend on the square root of the number of collected photons but also scales linearly with the separation L of the MINFLUX exposures. By decreasing the size of the displacement L at a fixed number of photons, this enables MINFLUX to outperform the square root law that limits conventional super-resolution microscopy techniques in practice.

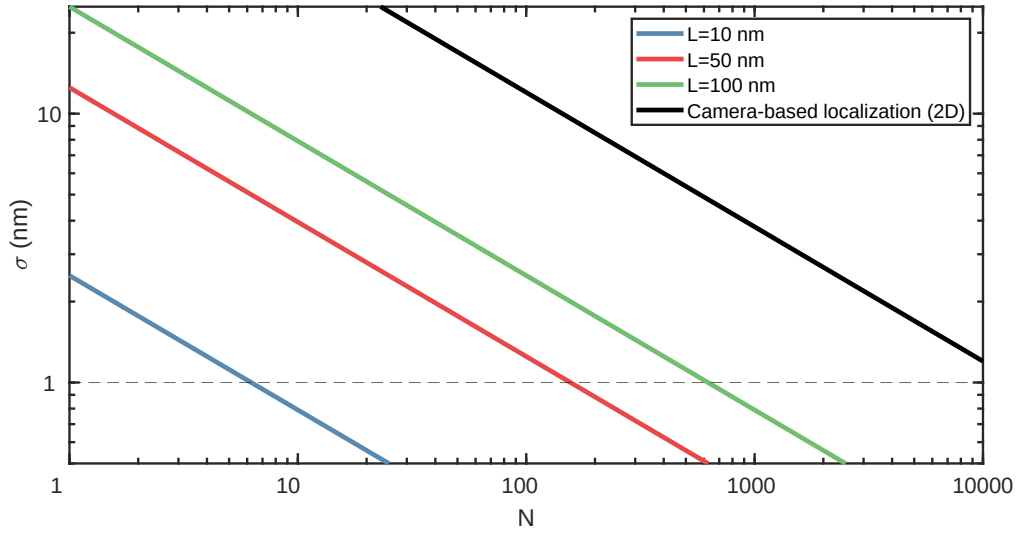

Figure 1.5: Expected Localization Precision in Dependence of the Number of Collected Photons The 1D localization precision at the center of the MINFLUX pattern is shown over the total number of collected photons for different beam separations L. Decreasing L leads to an effective improvement of the achieved localization precision. For comparison the 2D localization precision of an idealized camera is shown (black line). The data points for this curve were calculated assuming a standard deviation of the PSF of 120 nm [9]. To reach a precision of a single nanometer, in a camera-based localization a total number of 14,400 photons must be collected. When localizing with L=10 nm this number shrinks to ∼7 collected photons (per dimension). This means three orders of magnitude fewer fluorescence photons must be collected.

Assuming a background-free sample and a camera with a read-out noise of zero when localizing an unbleachable emitter, camera-based localization methods can be compared to MINFLUX under idealized conditions. In the case of camera localization, the standard deviation of the diffraction spot on the camera can be estimated to have a size of ∼120 nm if an excitation wavelength of 640 nm is used. To achieve a localization precision of 1 nm under these conditions one needs to collect 14,400 photons according to Equation 1.5. In contrast to that, only 1250 photons are necessary with MINFLUX using an L of 100 nm. Decreasing L to a size of 10 nm, the same localization precision is reached with only ∼7 photons per dimension or 14 photons for a 2D localization which is three orders of magnitude fewer than for the camera case.

This stands in contrast to the central criterion in super-resolution microscopy that the localization precision is primarily limited by the number of photons that a dye emits before bleaching. Decreasing L improves the precision of a MINFLUX localization faster than collecting additional photons. As the number of photons is not the central limiting factor for MINFLUX, it could be possible to move away from the few successful single molecule dyes that are optimized for maximal photon output to dyes that emit less photons but have other favorable properties e.g. increased solubility, photo caging for imaging or improved membrane penetration.

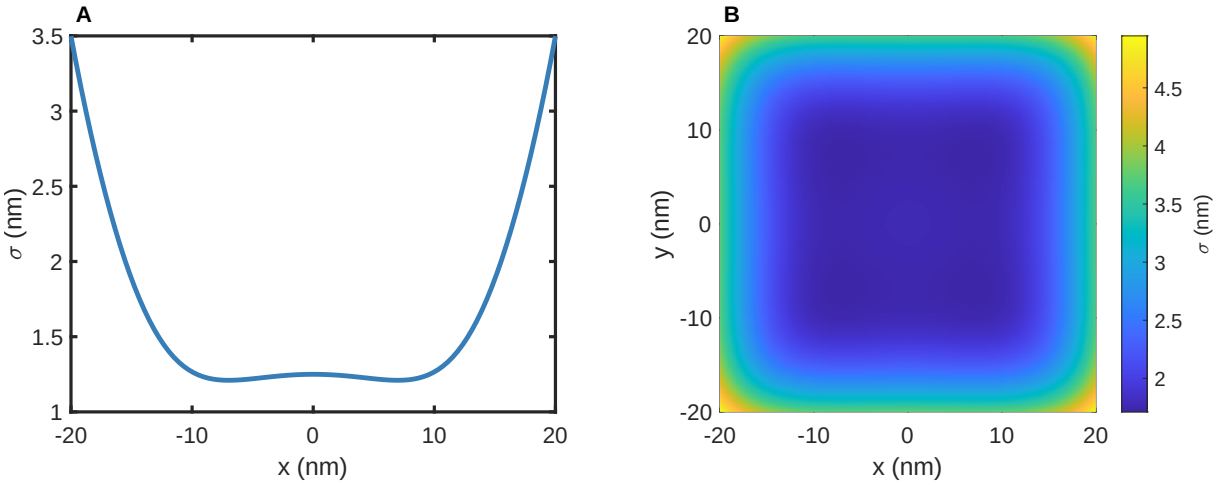

Figure 1.6: Precision over Position relative to Exposure Pattern and Localization Isotropy, **A** Localization precision σ over the position of the molecule relative to the coordinate system of the exposure pattern. The curve was calculated for L=50 nm for N=100 collected photons according to equation 1.13. The local minima at ± 8 nm emerge because the curvature of the central exposure at the molecule position is close to zero. **B** 2D-localization isotropy and range. Due to the sequential localization procedure the precision is relatively uniform in a range of $\pm\frac{L}{2}$.

To determine the FOV in which a MINFLUX localization leads to an efficient and precise position estimate, the localization precision in dependence of the x-position was calculated for the background free case in accordance with equation 1.13. The result of this calculation is depicted in Figure 1.6 **A**. The localization precision was calculated for a total number of collected photons of 100. The beam separation L was 50 nm. The two minima of the localization precision at $x = \pm 8$ nm are present because the localization precision mainly depends on the local curvature of the excitation PSF around the molecule position. As the central exposure is almost perfectly centered around the molecule position for $|x| < 10$ nm, the curvature of the central exposure is close to zero in this range.

By combining two subsequent 1D localizations with excitation PSFs featuring a local minimum in the respective direction we are able to laterally localize fluorophores. The geometric mean of the x and y localizations $\sigma = \sqrt{\sigma_x^2 + \sigma_y^2}$ in dependence of the position inside the MINFLUX excitation pattern is displayed in Figure 1.6 **B**. It shows that the localization precision is uniform in a large range around the origin and starts to increase strongly at a distance of about $\frac{L}{2}$ from it.

1.3.4 Optimal L under Realistic Conditions

In principle the localization precision could be scaled down to the Å-domain by decreasing L further and further while collecting the corresponding number of photons. In practice experimental limitations come into play. In the following paragraph, the smallest L

that is feasible when the localization precision is limited by the SBR will be considered. Reconsidering equation 1.13

$$\sigma_{x_m} = \frac{L}{2}\frac{\sqrt{(y_3-y_2)^2y_1+(y_1-y_3)^2y_2+(y_2-y_1)^2y_3}}{(y_1-2y_2+y_3)^2} \tag{1.15}$$

and assuming that the molecule is already approximately centered one can set $y_1 = y_3 = y$. This simplifies the equation to

$$\sigma_{x_m} = \frac{L}{8}\frac{\sqrt{2y}}{y-y_2} \tag{1.16}$$

We now define the SBR for an arbitrary $L = L_0$ as

$$SBR(L_0) = \frac{y(L_0)-y_2(L_0)}{y_2(L_0)} \tag{1.17}$$

And the number of photons collected as $N_{tot} = y_1+y_2+y_3$. Then the localization precision is described by

$$\sigma_{x_m} = \frac{L}{4\sqrt{N_{tot}}}\sqrt{1+\frac{3}{2SBR(L)}}\sqrt{1+\frac{1}{SBR(L)}} \tag{1.18}$$

The localization precision scales with L, with the square root of the number of collected photons and with the SBR in dependence of L. In general, the SBR will decrease if L is decreased as the number of collected photons will be smaller due to the lower effective excitation intensity at the outer exposures. This will decrease the achievable localization precision. By increasing the power to have the same fluorescence rate or number of collected photons at the outer exposures, the counts collected in the central exposure will rise too, thus preventing an improvement of the SBR.

Figure 1.7 shows σ_{x_m} for different SBRs in dependence of the selected beam separation L. The higher the SBR_0, the lower the optimal L, L_{opt} will be. SBR_0 is calculated according to Equation 1.18. For a SBR_0 of 150, L_{opt} amounts to 6.5 nm. In the case of an SBR_0 of 50 L_{opt} is 14.5 nm and for a SBR_0 of 10, an L as large as 24.9 nm should be chosen. Using this as a guideline one should note that the curvature is asymmetric around the minimum. This means for L smaller than the optimum the localization precision rises faster than for an L larger than the optimum.

Structure of this Thesis Following the introduction, Chapter 2 describes the Phase Scanner and the optical setup that was developed in the context of this thesis as wells as all other methods and materials used in this work. The approach to localize single emitters with our setup is explained in Chapter 3. There, on the example of Atto647N and Cy3B single molecules, it will be shown that MINFLUX has a higher localization efficiency than all established light microscopy methods. Various tracking experiments

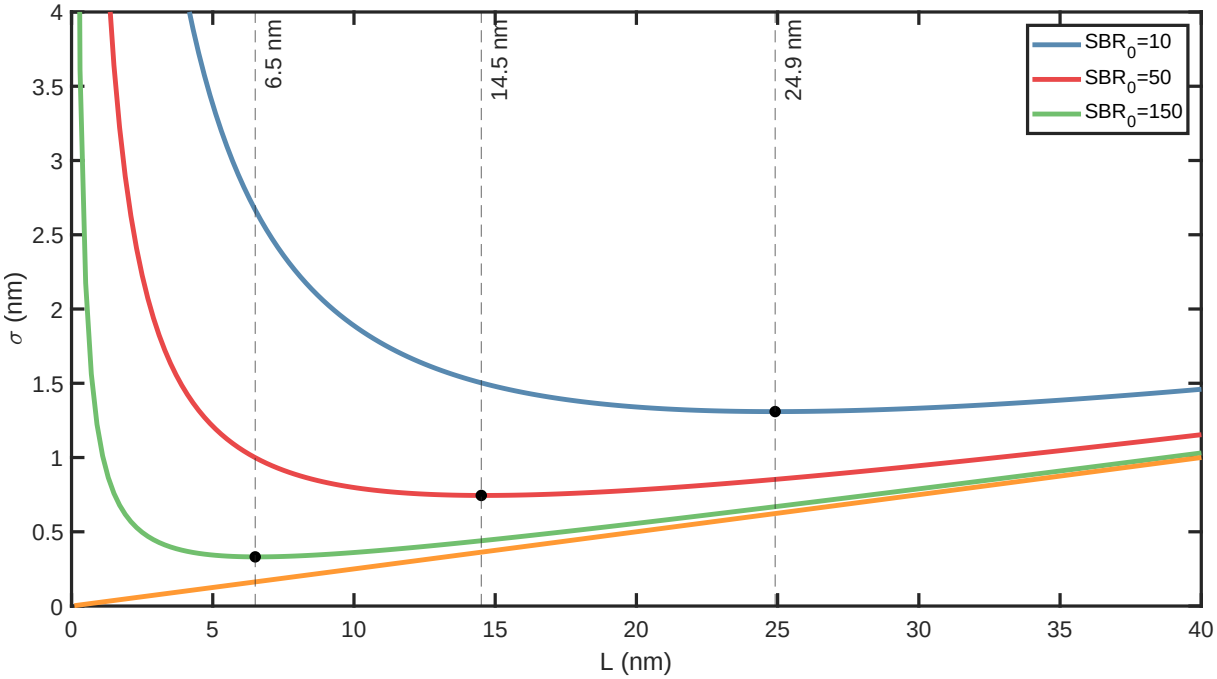

Figure 1.7: Localization precision over L for multiple SBRs Without background L can be chosen infinitesimally small to yield perfect localization precision (orange curve). If background is introduced it limits the achievable localization precision. The localization precision at a certain SBR_0 depends on the chosen L because the measured SBR decreases when L is decreased. The higher the initial SBR_0 the smaller L should be to optimize the localization precision. The optimal L for each SBR is marked additionally by the black dot and the dashed line.

are described in Chapter 4 and demonstrate the extraordinary spatio-temporal resolution that MINFLUX offers.

Chapter 2

Materials and Methods

2.1 Phase Scanner

2.1.1 Motivation and General Principle

The phase scanner is the major technical innovation and sets apart the herein presented setup from established and published MINFLUX microscopy setups employing electro-optical deflectors (EOD) for fine scanning [14, 16, 17]. In contrast to EODs, its central paradigm is creating a controllable PSF by splitting a Gaussian excitation beam into multiple coherent beamlets in the back focal plane (BFP) with individually controllable phase. By modulating the phase difference of the beamlets, it is possible to control the interference pattern, that results when the beamlets are focused by the microscope objective, and therefore shape or move the PSF. It allows for sub-microsecond fast changes of the PSF and can be readily programmed for all wavelengths.

To carry out MINFLUX localizations, one of the central tasks of a microscope is the generation of a PSF with an intensity minimum. In order to test the physical limits of the localization approach it is necessary to optimize the determining parameters. One central factor is the curvature of the point spread function around the probing minimum. The SBR improves with an increasing curvature of the intensity profile around its minimum. Equation 1.18 shows that the consequence is a higher localization precision for the same number of collected photons. It is therefore highly desirable to generate a PSF with maximized curvature around the probing minimum to optimize the achieved SBR.

The setup must further be able to scan this PSF with high speed and precision around the molecules estimated coordinates in order to position the beam in the desired pattern

for localizations with multiple exposures.

As stated in Section 1.3, MINFLUX provides a higher photon efficiency than any established microscopy technique. It is therefore possible to deploy dyes with lower photon output without compromising the microscope performance. To assess the suitability of dyes over a wide spectral range, a setup that enables the straightforward implementation of additional excitation wavelengths without hardware changes is very convenient.

To address these requirements, we developed the phase scanner. It is a device that creates a variable PSF by individually modulating the phase and amplitude of beamlets. The TEM 01 mode has the greatest possible steepness around a minimum of a PSF in a single objective arrangement [3]. It is created by overlapping two separate beamlets with a phase difference of π in the focal spot. The higher the effective numerical apertures of the two beams the steeper it will be. This mode will be called Half-Moon (HM) PSF. As rapid switching between wavelengths, PSFs and scanning positions is required, we chose electro-optic modulators as optical means to introduce phase and amplitude modulations. By applying voltages in a range below 1 kV, fast changes of the respective parameters are possible. The phase scanner is able to perform a fine scan by shifting the minimum of the PSF relative to the PSF center. This fine scanning is used to position the PSF's minimum in the desired MINFLUX pattern.

In this section the physical concept behind the device, as well as the experimental implementation in our setup will be explained. Our novel approach will be further compared to the established one based on PSF creation with spatial light modulators or phase masks combined with scanning with electro-optic deflectors.

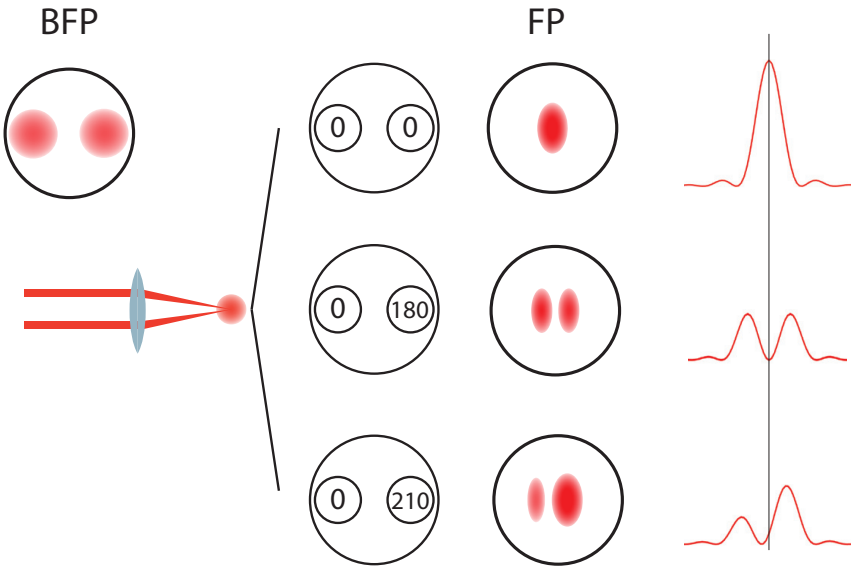

Figure 2.1: Basic Scheme of the phase scanner The phase scanner is able to generate and scan various PSFs. The two beamlets in the BFP are overlapped by focusing them with the objective lens. When the beamlets are coherent they will interfere and the resulting intensity distribution depends on their phase difference. In the first case the phase difference is zero and the beams interfere constructively. Due to the asymmetric filling of the BFP the resulting PSF will be slightly elongated along the y direction. The corresponding intensity profile is depicted on the right side. If the phase difference is π the two beams interfere destructively in the focal plane. This creates a local intensity minimum in the center of the resulting PSF. By tuning the phase difference around this point the position of the local minimum can be shifted spatially inside of the diffraction limited spot. According to PSF calculations the intensity in the minimum stays zero irrespective of the applied phase difference. This can be employed to carry out MINFLUX localizations

In Figure 2.1 the general operating principle is shown, with two beams featuring an offset relative to each other in x direction in the back focal plane of the microscope objective. By focusing them with the objective lens, the beamlets overlap in the focal plane and interfere. The intensity distribution of the interference pattern depends on the phase difference of the partial beams. If the phase difference of the beams is a multiple of 2π, the interference will be constructive in the center of the focal plane creating a spot with maximal light intensity. If the phase difference is an uneven multiple of π, the interference will be destructive at this position, resulting in a local intensity minimum. By fine tuning the phase difference in a range around this point it is possible to control and scan the position of the local minimum with high precision in the focal plane. This local minimum is used as probe to localize emitters with the MINFLUX localization approach.

2.1.2 Physical Principles

We chose electro-optic modulators to control the phases of the beamlets because of their versatility and fast switching speed. In the following, some theoretical aspects of the phase control with these modulators will be discussed. First, the Pockels effect will be explained as it is the central physical effect describing the phenomenon of voltage induced creation and change of birefringence and therefore enables the phase control. Subsequently, it will be shown how crystals displaying the Pockels effect can be arranged to manipulate phase and amplitude of laser beams. In the following sections how this application of the Pockels effect enables PSF engineering and fine scanning in different scenarios.

Pockels Effect

The Pockels effect describes the phenomenon of voltage- or electric field induced creation or change of birefringence in certain crystalline materials. It is also known as linear electro-optic effect as the relative change of the refractive indices is in first order proportional to the change of the applied electric field [26].

The refractive index $n(E)$ is given by

$$n(E) = n - \frac{1}{2} r n^3 E \tag{2.1}$$

with the field-free refractive index n, the applied electric field E and the electro-optic coefficient r typically being in the range of $\sim 10\,\mathrm{pm/V}$. This change of the refractive index influences the optical path length (OPL) of a laser beam that passes through a medium exhibiting the Pockels effect. The phase shift induced by the OPL change can be described as

$$\Delta\Phi = -\frac{\pi r n^3 E l}{\lambda} \tag{2.2}$$

With l being the length of the medium and λ the wavelength of the laser beam. By creating a phase difference between modulated and unmodulated beamlets, the resulting interference pattern can be controlled. In the technical implementation the strength of the phase shift depends on the electric field strength and the length of the employed crystal. To characterize the modulator, the so-called half-wave voltage is defined. It describes the voltage that must be applied to generate a phase shift of π:

$$V_\pi = \frac{\lambda d}{n^3 r l} \tag{2.3}$$

Manipulation of Beam Polarization Ellipticity

To change the polarization of a linearly polarized beam via the Pockels effect the input polarization must be rotated 45° to the crystal's z-axis, which is defined by the electric field direction. The input light can then be described as superposition of two perpendicularly polarized components, of which one is oriented parallel to the z axis and the other one is perpendicular to z axis. Due to the birefringence of the optical crystals, the two components will travel different OPLs in the material and will therefore accumulate a phase difference. This difference can be controlled by the applied voltage as the refractive indices the two components experience are varied by the electric field. If the phase difference is 0° or 180°, the resulting beam polarization is linear. For all other values the polarization is elliptical.

If such a modulator is positioned between parallel polarizers, it is possible to modulate the output power of the laser beam as the intensity of the polarization component that is transmitted can be controlled by the applied voltage.

In our experimental setup such a modulator is installed to control the phase difference between two interfering beams. After modulation the components are split up and brought to interference. The interference pattern then depends on the phase shift between the two components created by the polarization modulator. For more details refer to Section 2.1.4.

2.1.3 PSF Engineering by Phase-Controlled Interference

The following subsections elaborate on the potential of PSF engineering by splitting the beam into parts with different, modulateable phases that was described in general in Section 2.1.1. First the generation of 2D PSFs created by interference of two beamlets will be discussed. The experimental realization will comprise few component and will offer easy control. Second, the possibilities for creating a PSF with a local minimum with three beams that are positioned asymmetrically in the BFP are examined. Last the generation of 2D PSFs created by four beamlets with full power and phase control is elucidated.

Two Beamlets with Symmetrical Position in the BFP

In the presented setup, at each point in time, the beams are steered such that there are either two beams with x separation or two beams with y separation in the BFP. With two beams, only the phase difference between these two needs to be controlled. As shown in Figure 2.2, this can either lead to a spot or a centered $HM_{X/Y}$ PSF. Additionally a $HM_{X/Y}$

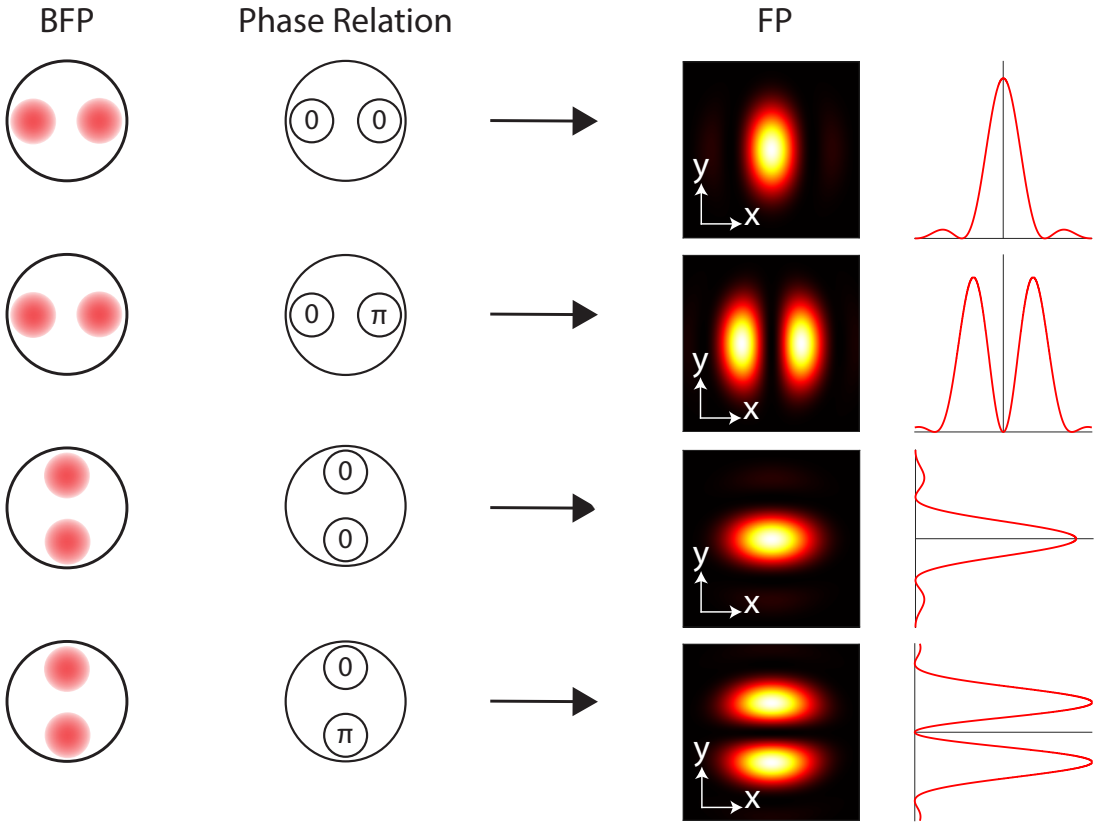

Figure 2.2: Possible PSFs for Two Beamlets with Symmetric Arrangement The PSFs that are possible in the presented setup. The technical realization will be explained in Section 2.1.4. At the displayed phase relation the corresponding PSF in the focal plane will be generated. The last column shows the intensity profile along the x axis and the y axis, respectively. Analogous to the case of two beamlets in x direction that create a PSF with local intensity minimum in x direction it is possible to create a PSF featuring a minimum in y direction. For all PSFs a small change in the phase relation between the interfering beams enables fine scanning of the generated PSF. Figure 2.13 shows the relation between the applied phase shift and the displacement of the intensity minimum.

PSF with a shifted minimum position can be generated when the phase difference is not a multiple of π. To record a 2D MINFLUX localization with such a PSF, a MINFLUX localization is performed first in x direction with the HM_X-PSF. Subsequently the PSF is switched to HM_Y and a 1D localization in y direction follows. By combining these two 1D localizations the 2D position of the emitter in the sample space is obtained.

Three Beamlets with Asymmetrical Position in the BFP

The PSFs mentioned above, that feature a local minimum, can be used to laterally localize a fluorophore as their intensity minima are located in the xy-plane. In biological samples, 3D information about a structure is highly relevant. Thus, acquiring localizations in all three spatial dimensions is an important task for the scanner of a MINFLUX setup.

For a scanner employing EODs, a PSF featuring an intensity minimum in all three dimensions is essential as fast switching between different PSFs is not possible. The most commonly used PSF of this kind is created by a so-called top-hat phase mask. The destructive interference leads to a minimum in all three spatial dimensions, which however strongly varies in the achieved curvatures along the different axes (Figure 2.3**A**). This is explained in further detail in Section 2.1.5. For shifting the position in z-direction, an additional scanning mechanism is required. Varifocal lenses move the focal plane in z-direction but suffer from multiple drawbacks (e.g. multiple millisecond wait time for new axial position and chromatic aberrations due to single lens design).

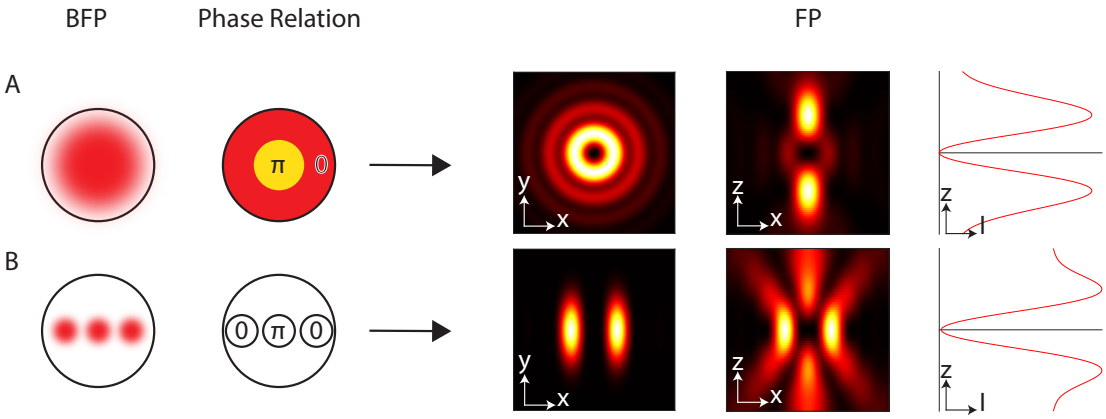

Figure 2.3: Different methods to generate axial intensity minimum A The established method to generate a axial minimum from [15] is to create an excitation PSF with the so-called Top-Hat phase mask. When passing the phase mask, the inner segment of the excitation beam is phase shifted by π. In the xy-plane this generates a donut with multiple sidelobes. In the xz-view the intensity minimum along z is shown. The different curvatures of the PSF for the lateral and axial direction around the intensity minimum lead to an anisotropic localization sensivity. **B** When positioning three beams with the depicted arrangement and phase relation in the BFP of the microscope objective a PSF with a minimum along the axial direction can be generated. For full destructive interference the intensity of the central beam must be ~ 1.9 times higher than for the two outer beams. Due to the sequential localization approach, for each 1D localization a PSF with the optimal curvature can be employed.

The phase scanner can create a local minimum in z-direction in an arrangement with two off-axis and one on-axis beam in the BFP. A calculation of the corresponding PSF is depicted in Figure 2.3 **B**. Analogous to the described localization scheme in the xy-plane, this PSF can be used to perform axial MINFLUX localizations. A slight shift of the phase difference allows scanning of the local minimum along the z axis. The position of the minimum can be shifted on a microsecond timescale.To finally gain full 3D position information, sequential x, y and z localizations must be acquired.

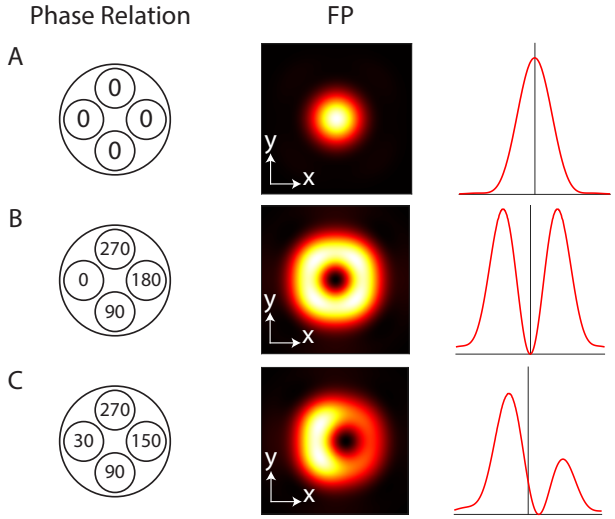

Figure 2.4: Generation of donut PSF out of four phase controlled beamlets, All phase relation specifications are stated in degree. **A** By overlapping the four beamlets without phase shift a 2D Gaussian shaped PSF is created per constructive interference. **B** shows the creation of a donut PSF by tuning the phase such, that each beam has a phase shift of π or 180° to the opposing beam in the BFP. Additionally, the phase relation between neighboring beams is $\frac{\pi}{2}$ or 90°. Combined with a circular polarization, this leads to destructive interference and therefore an intensity minimum in the center of the PSF. **C** shows, that by shifting the phase difference of opposing beams by the same amount, the point of destructive interference can be shifted. This allows to scan the location of the minimum in this direction.

Four Beamlets

By overlapping four beams in the BFP without phase shift, it is possible to create a focal spot in the sample plane that is approximately Gaussian shaped, as the beams will interfere constructively in the center of the focal spot (Figure 2.4 **A**). Changing the phase differences between the four beams in a certain way allows for the generation of other non-gaussian PSFs.

Typically, a PSF with a donut-shaped intensity profile is created by using a vortex phase plate. After passing a vortex phase plate, each beam segment has a counterpart on the opposing side of the optical axis that features exactly π phase difference. Therefore all beam segments interfere, such that there is a local minimum along the optical axis, if circular polarization is used. It was shown that a donut-PSF can also be created by using a wave plate featuring only four discrete segments which creates a phase difference like the one depicted in Figure 2.4 **B** [27]. The same feat is possible by using the phase scanner to tune the phases of the four beams in the BFP accordingly. Similar to the two beam case, it is possible to scan the local minimum over the point of interest by fine tuning the phases around the donut set point and thus to perform MINFLUX localizations (Figure 2.4 **C**).

Synthesis of Arbitrary PSFs by Beamlet Interference

The concept of increasing the number of beamlets in the BFP and therefore the degrees of freedom can be extended further. In principle, by employing arbitrarily high number of beamlets with full power and phase control, arbitrary PSFs can be switched, formed and scanned on a microsecond timescale. When fast switching is required, such a device could potentially replace deformable mirrors and spatial light modulators, the gold standard of adaptive optics in light microscopy. The costs to pay include an increasing complexity and higher requirements on the optical quality of the beam splitting and phase modulating components.

2.1.4 Experimental Implementation

The setup that was used to conduct the measurements in the Chapters 3 and 4 employed optical devices to control four beamlets with two independent phases for localizations in x and y directions, as explained in Subsection 2.1.3. It will be described in detail in this subsection and is shown in Figure 2.5.

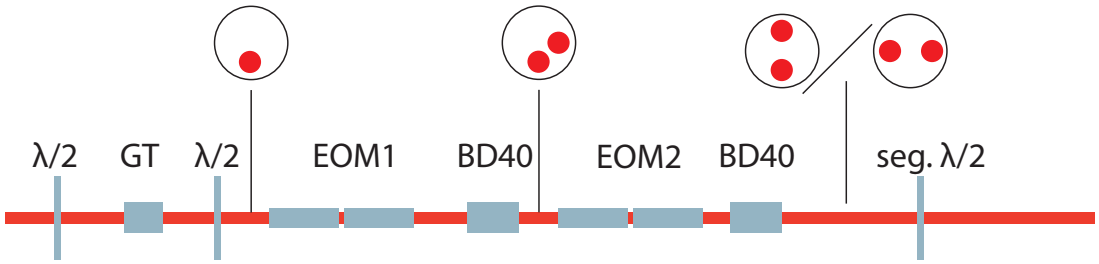

Figure 2.5: Sketch of the experimental implementation of the phase scanner All meausuremts in the context of this thesis were recorded with the depicted setup. It enables the generation of a spot-like PSF as well as $HM_{X/Y}$-PSFs. The input laser beam is first polarization rotated and filtered. Then it is rotated again to match the crystal axis of the phase modulator crystal (EOM1). The BD40 calcite beam displacers splits the beam by its polarization components. The split beams then pass the amplitude or polarization modulator crystal (EOM2). Depending on the voltage that is applied to this modulator, the polarization is rotated such that either an x-PSF or a y-PSF is created. The segmented half-wave plate rotates the polarization to restore the ability of the beamlets to inferfere.

The polarization of the laser light that emerges from the optical single-mode fiber (see Figure 2.14) is first rotated by a half-wave plate and cleaned by a Glan-Thompson-Polarizer to ensure high polarization purity. The beam is then polarized horizontally by a half-wave plate sitting in a motorized rotation mount. This mount allows for the fine tuning of the power balance of the two interfering beams that are created by polarization splitting as the power balance depends on the input polarization of the phase scanner system. (see following sections)

Afterwards, the beam passes the custom-built electro-optic phase modulator (EOM1) which consists of two RTP crystals (custom manufactured by Cristal Laser, P.A. du Breuil, France) with dimensions of 3.5x3.5x25 mm, which are oriented perpendicular to each other. The crystals are mounted in a 45° angle to the optical table establishing a 45° angle between the birefringent crystal axis and the polarization axis of the laser beam. By applying an electric field through a custom-built high voltage amplifier, the polarization component parallel to the field axis can be retarded in respect to the perpendicular component. This will later lead to a phase difference of the interfering beam components.

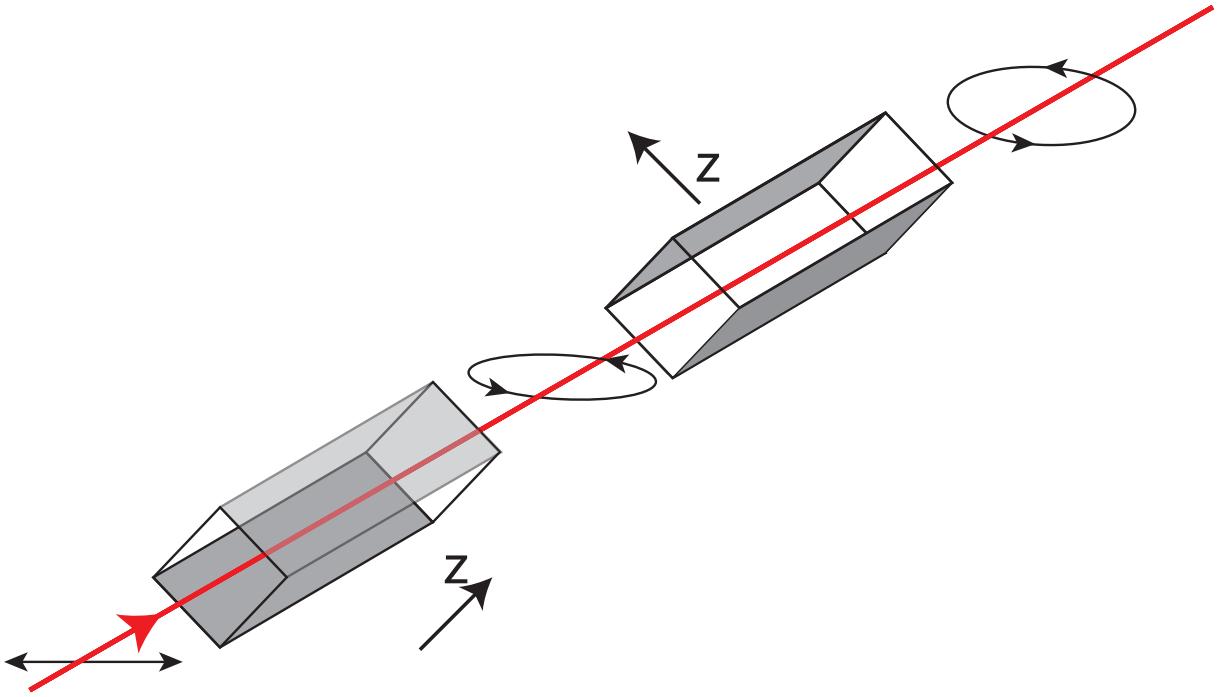

Figure 2.6: Electro-optic phase modulator consisting of two RTP crystals The phase modulator consists of two RTP crystals. Through the electrodes on the surfaces of the crystals a voltage can be applied to generate an electric field. The modulators are passed by the beam subsequently. Because the polarization is oriented 45° to the z-axis of the first crystal, the phase difference that is accumulated by the polarization components can be controlled by the applied voltage. The components are later split by a beam displacer and the controllable phase difference allows to steer the PSF that is generated.

To create separate beamlets out of single input beam, the beam is passed through a birefringent calcite displacer (BD40, Thorlabs Inc. Newton, USA). The displacer splits the beam by polarization and fills the second pupil segment along the optical axis. Subsequently, the two beams pass a second custom built electro-optic modulator (EOM2). It consists of two RTP crystals with dimensions of 8x8x25 mm, which are again oriented perpendicular to each other. One crystal is mounted parallel and the other crystal perpendicular to the electric field axis and to the optical table surface. As the polarization of the incoming beams is 45° to these axes, the Pockels effect leads again to a controllable ellipticity of the beam polarizations. The beams then pass a second calcite displacer, structurally identical to the first one, displacing the beams depending on their polariza-

tion.

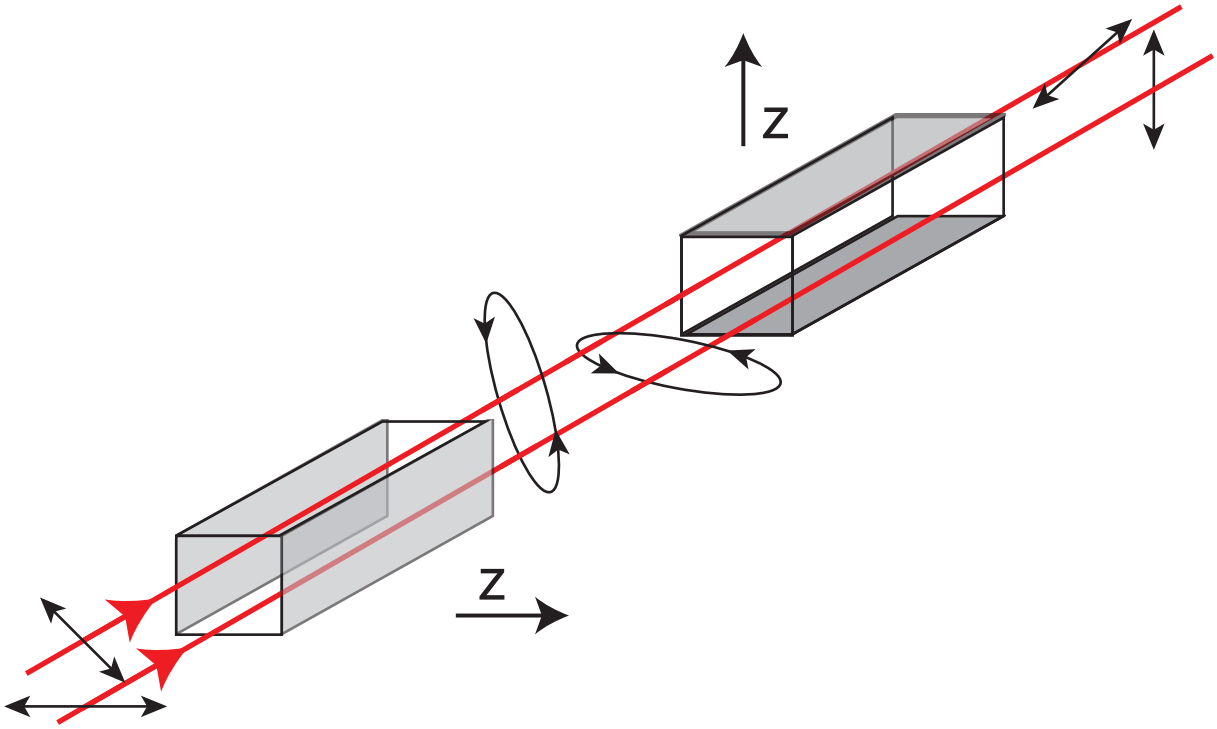

Figure 2.7: Electro-optic polarization modulator After the beams are phase modulated and split up by polarization components they pass the second electro-optic modulator. The beam polarization angles are oriented 45° to the z-axis of the first RTP crystal. This leads to a different retardation of the polarization components, depending on the voltage that is applied to the electrodes on the crystals surfaces (gray). The retardation changes the ellipticity of the beams polarization. If the applied electric field is large enough, the output polarization will be linear again but rotated 90° with respect to the input polarization of the modulator.

Taken together, this assembly of electro-optic modulators and the calcite displacers steers the beamlets into the left and right (resulting in an x PSF Spot/HM_X) or into top and bottom pupil segment (resulting in an y PSF) via voltage changes. Whether the PSF features a local minimum (HM-PSF) or not (Gaussian-shaped/Spot PSF) depends on the phase difference that the two beamlets have accumulated in the first modulator. Finally, the beams pass a segmented half-wave plate to align the polarizations of the beamlets, such that they are able to interfere.

This experimental implementation enables fast 2D localizations in the xy-plane by subsequently switching between HM_X and HM_Y PSFs. This makes it possible to track emitter movements in a diffraction limited spot with sub-millisecond speed and nanometer precision. The PSFs that were used to carry out the experiments presented in this work are shown in Figure 2.8. Because the assembly is very compact the phase shift caused by thermal drift between the optical pathways is minimized. As both modulators consist of two crystals with perpendicular orientation, thermal drift of the modulating crystals themselves and consequentially a shift of the OPLs in the modulators will be compen-

sated by the assembly. An additional advantage is that all beamlets pass the same optical components. Any change of the beam pointing will therefore act on all beamlets in the same manner and will only lead to a slight shift of the FOV but not to distortions inside the FOV.

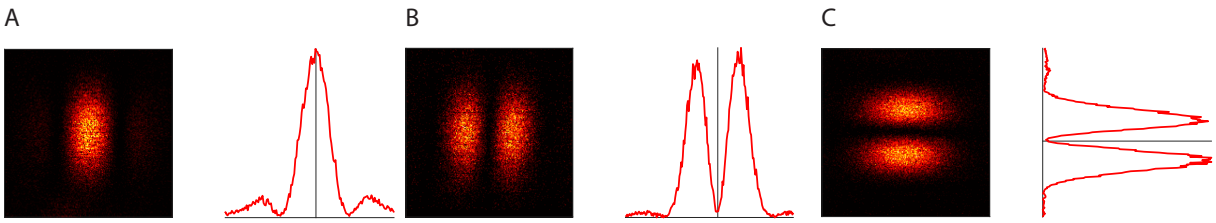

Figure 2.8: Experimental PSFs generated by the phase scanner The Figure shows the different PSFs and corresponding profiles that were used in the experiments presented in this work: **A** Spot$_x$ PSF **B** HM_X PSF featuring a intensity minimum along x **C** HM_Y PSF with minimum along y axis.

2.1.5 General Advantages of the Phase Scanner

Higher Curvature of PSF around Intensity Minimum

As described in Chapter 1, the precision of a MINFLUX localization depends on various parameters, among others the SBR. The higher the SBR, the better the localization precision will be if all other parameters are kept constant. It is therefore desirable to achieve the highest SBR possible at a certain L. The achieved SBR is strongly dependent on the curvature of the PSF around the minimum. A higher curvature leads to a better sensitivity and depends on the numerical aperture of the microscope objective, the laser wavelength and the method of PSF generation. Figure 2.9 shows a PSF calculation according to Richards and Wolf of multiple beam profiles [28].

For xy-localizations, the PSF created by the phase scanner with a beam distance of 4 mm in the BFP and a beam diameter of 2 mm has an up to 35% higher intensity around the minimum than a donut PSF created by a phase mask or a spatial light modulator when a beam filling the whole aperture ($FWHM \approx 5$ mm) is employed if all other beam parameters are held constant. The PSF calculation also shows that, according to equation 1.18, the improvement of the SBR leads to an improvement in the localization precision of up to 12%.

In an implementation that allows z-localizations, the phase scanner has a further advantage. As mentioned above, the current state of the art for performing 3D localizations is to use a PSF created by a top hat phase mask. Due to the severely inhomogeneous PSF

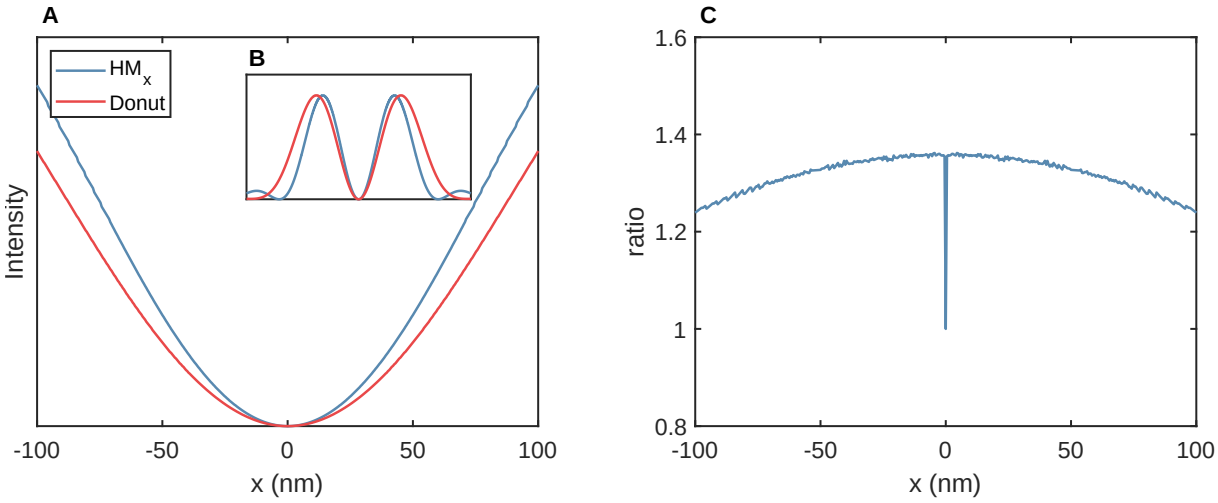

Figure 2.9: Comparison of steepness around the minimum for HM_X and donut profile, **A** PSF Calculations show that the intensity of the profile of a HM_X-PSF (blue line) rises significantly faster than for the donut profile (red line). In **B** the ratio of intensities $I(HM_X)/I(Donut)$ is depicted. The graph shows that close to the minimum the intensity of HM_x is up to 35%.

curvature (see Subsection 2.1.3), an elaborate calibration process is necessary to gain reliable localizations in all three dimensions. By instead employing a localization procedure that consists of three subsequent localizations for the three dimensions, three PSFs with similar curvatures and a simpler, real-time capable calculating algorithm can be used. This procedure not only enables nearly isotropic localization precision in all dimensions but can also be executed on the FPGA board. As the position of the local minimum can be controlled by modulating the phase of one of the interfering beams, shifting the PSF along z with a varifocal lens is not necessary.

Wavelength independence and simplicity of the setup

Compared to the published MINFLUX setups [14, 16, 17], the phase scanner features a number of advantages such as the simplicity and compactness of the setup, and the possibility to implement additional excitation wavelengths simply by coupling another laser into the excitation fiber. In all the established MINFLUX setups, each additional excitation wavelengths requires one additional beam path per excitation wavelength that features either an SLM or a phase mask tailored to the respective wavelength to create the donut PSF. Individual SLMs are necessary as they can only be switched on a millisecond time scale. In contrast to that, the phase scanner is able to switch between different excitation wavelengths on a microsecond time scale. By controlling the various laser powers with an AOTF or electro-optic amplitude modulators the desired laser is selected. The phase scanner then accounts for the different wavelengths only by changing the voltages that are applied to the two electro-optical modulators.

Although it is possible to perform multicolor imaging with a single excitation wavelength using spectral separation of the emitters in the detection pathway [15, 16], a setup with multiple excitation wavelengths is advantageous. As described, MINFLUX is inherently more photon-efficient than conventional fluorescence nanoscopy techniques. It is generally not bound to the brightest dyes available, but its resolution is limited by background. Additional excitation wavelengths allow for the use of excitation bands, in which autofluorescence and phosphorescence, as well as fluorescence from optical glasses in the beam path are weaker. Due to the fast switching between excitation wavelengths, it is possible to perform multicolor tracking of non-blinking dyes with highest precision and time resolution.

With the ability to switch between spot like PSFs and PSFs with a local minimum, the need to align individual Gaussian and donut-shaped beams is omitted, and thus the setup simplicity increases while maintenance effort decreases. As the same beam is modulated to form either one of the profiles, the overlap is always perfect and no adjustment of mirrors or other optical components is necessary.

2.1.6 Calibration Procedure

The voltages that must be applied to the electro-optic modulators depend among others on the wavelength of the modulated light, the dimensions of the employed phase modulator crystals, the temperature of the crystals and the optical path lengths that are subject to thermal drift. To account for changes of these parameters, we developed an automatized calibration procedure that can be carried out in a matter of seconds. When changing between the different possible PSFs, the voltages of the electro-optic modulator switching between x and y beams must be adjusted precisely. It is vital to minimize the intensity of the non-desired beams, as any residual intensity leads to a raised background in the local minimum, presumably decreasing the attainable SBR. Scanning precisely with the phase scanner also requires exact knowledge of the relation between voltage adjustment and displacement of the minimum position.

Switching Modulator Calibration

To calibrate the modulator that changes between x-PSF and y-PSF, the applied voltage is modulated over the range from $-400\,\mathrm{V}$ to $400\,\mathrm{V}$ and images of the laser intensity distribution in the BFP are recorded on a CCD camera. The images contain information about the intensity distribution of the four beams for every applied voltage. The individual images of the beams are first added up, resulting in an image showing all four spots (see

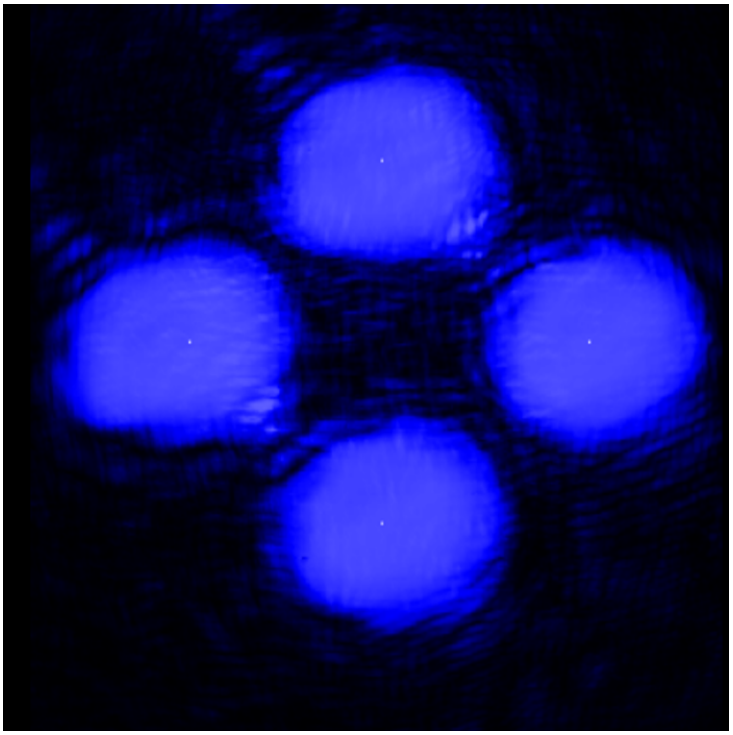

Figure 2.10: Sum of images for calibration of switching modulator When sweeping the voltage applied to the switching modulator (EOM2) all images of camera 1 (see Figure 2.14) are recorded and summed up. The image is rotated by 45° and split into four segments along the axis defined by the center of mass of the image. The integrated intensities of the four segments are calculated to form for individual curves for further evaluation (see Figure 2.11).

Figure 2.10). The image is rotated by 45° and the center of mass of the intensities is calculated. Subsequently, the image is split along x and y direction by the coordinate of the center of mass, resulting in four segments. The intensity over the applied voltage is then extracted for each segment. These curves feature a parabolic minimum at a certain voltage, which is fitted with a polynomial function with grade 2 to extract the exact voltage. Due to parasitic beams and reflections, the minima in the two segments corresponding to the x-beams will not be located at exactly the same voltage, therefore the mean of the two fitted minima is calculated and used as reference point for the HM_x-PSF and vice versa.

Phase Modulator Calibration

The voltage that is applied to the electro-optic modulator is calculated based on two parameters, each with separate calibration procedures. The first parameter is the change of phase difference in dependence of the voltage that is applied to the electro-optic phase modulator $\frac{d\phi}{dU}$ and will be called frequency. The second one describes the spatial displacement in dependence of the angle of phase difference between the two interfering beams $\frac{dX}{d\phi}$.

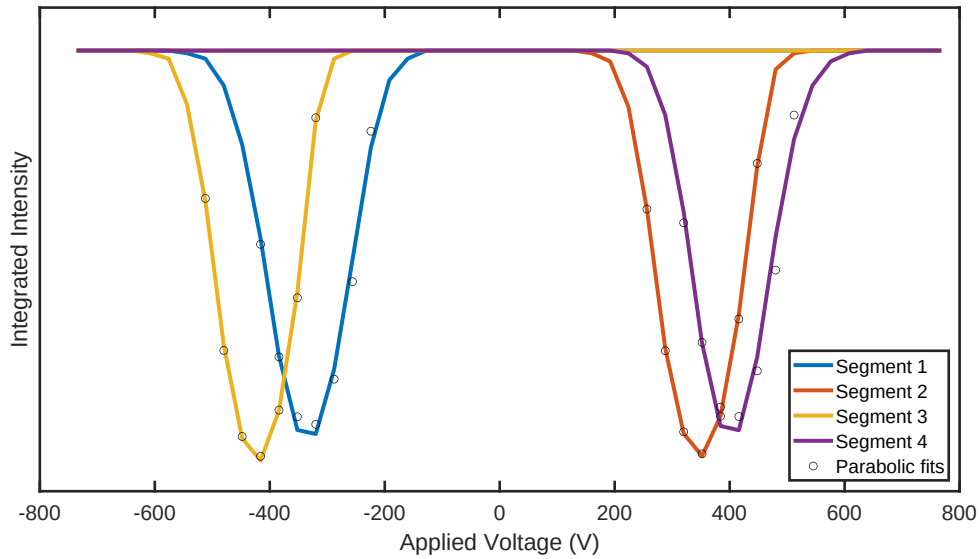

Figure 2.11: Intensity in the different segments over the voltage applied at EOM2 To generate the lowest intensity minimum available it is crucial to minimize the intensity in the non-desired beamlets. To find the voltage corresponding to this minimal intensity, the individual intensities are evaluated in dependence of the applied voltages. Due to various confounding factors the minima of the curves corresponding to the x-beams or y-beams are slightly offset. As a compromise, the minima of the curve are fitted with a parabolic curve and the mean of the two voltages with minimal intensity are saved as reference point.

Frequency Calibration To calibrate the frequency $\frac{d\phi}{dU}$ that describes the dependence of phase shift on the applied voltage either the x- or the y-beams are switched on with EOM 2. The voltage on EOM 1 is then modulated from $-400\,\mathrm{V}$ to $400\,\mathrm{V}$ in increments of $1\,\mathrm{V}$. For each voltage, the image on camera 2 is recorded. As the laser beam is focused on camera 2 it captures an image similar to the intensity distribution in the focal spot, but with lower NA. To evaluate the image stack, the images are summed up and the point with maximal intensity is fitted with a Gaussian distribution. Subsequently, the intensity at this point is evaluated over the range of the modulated voltage. The resulting data points are fitted using a non-linear fit calculated by the Levenberg-Marquardt method with the function $\sin^2 I(U)$ [29, 30]. From the period length of the fitted function, $\frac{d\phi}{dU}$ can be calculated. Additionally, the point with minimum intensity is calculated from the fit, as the voltage at this point creates destructive interference. Thus, this voltage is used as reference point. Setting the phase modulator voltage to this value will result in the HM_X/Y-PSF with the minimum position centered in the diffraction limited spot. The setting for the reference point and the frequency are saved in a text file containing all relevant calibration parameters. The procedure is then repeated for the second direction.

Calibration of the Spatial Displacement in Dependence of Phase $\frac{dX}{d\phi}$ PSF calculations revealed a linear relationship between the phase difference of the beamlets and the position of local minima of the HM_X/Y-PSF. Figure 2.13 **A** displays the calculated

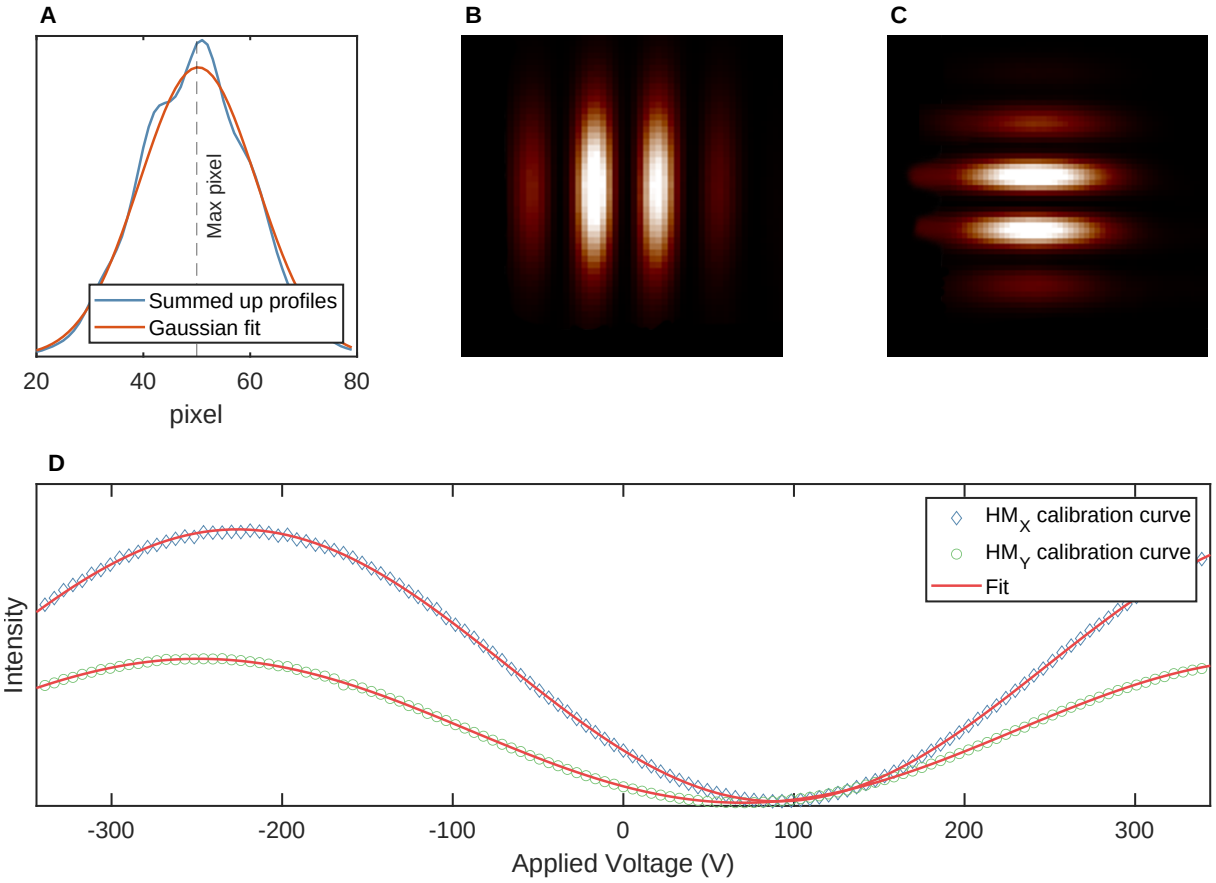

Figure 2.12: Phase scanner frequency calibration procedure, **A** All image profiles of one dimension (B/C) on camera 1 during a voltage sweep are recorded and added up to. The resulting curve has a clear maximum which corresponds to the center of the PSF on camera 2. The curve is fitted with a Gaussian distribution to find the pixel of maximal intensity more precisely. The intensity at this pixel over the voltage is analyzed further. An example curve is shown in **D**. The frequency of the resulting sinusoidal curve is fitted with a function of the form $\sin^2 I(U)$. The point of minimal intensity is calculated from the fit result and represents the reference point which creates the HM_X/Y-PSF with the minimum located in the center of the diffraction spot that is targeted with the galvanometer scanner. The procedure is then repeated for the second direction.

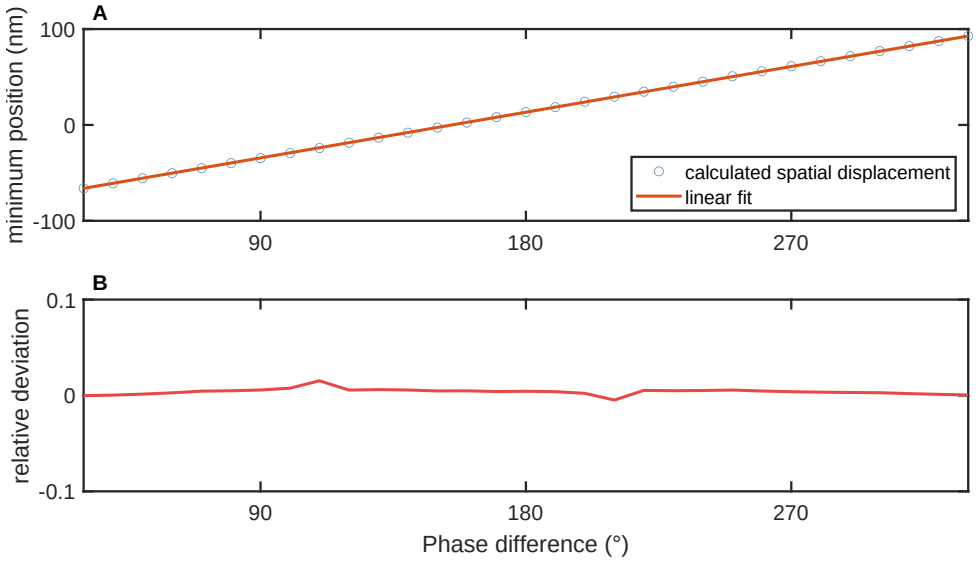

Figure 2.13: Linear relationship between spatial displacement and phase difference, **A** displays a calculation that suggests an almost perfect linear relationship between the phase difference of two beamlets in the phase scanner and the displacement of the intensity minimum's position. To evaluate the deviation from a linear relationship a linear curve was fitted to the data in **A** and the relative deviation of the data points and the linear fit is depicted in **B**. The maximum deviation between the two curves is below 5%. The asymmetric nature of the two spikes suggests that this could be an artifact of the integration grid of the PSF calculation.

minimum position over the phase difference as well as a linear fit to the data. Figure 2.13 **B** shows the relative deviation from the linear fit. Its maximum value is around 5% which presumably is caused by the finite precision of the calculating grid.

The extent of the spatial displacement of the PSF's minimum, resulting from a shift of the phase difference, depends on multiple parameters e.g. the diameters of the individual beams, their position in the back focal plane, beam intensity distribution, numerical aperture, beam polarization and the laser wavelength. As some of these parameters are subject to thermal drift and fluctuations, $\frac{dX}{d\phi}$ was not calculated but determined experimentally. For this purpose a program was implemented that modulates the position of the sample stage periodically with a controllable amplitude. To tune $\frac{dX}{d\phi}$, MINFLUX tracking on beads was performed while the sample stage alternated periodically between two positions 10 nm apart. Fluorescent beads (20 or 40 nm) or gold nano particles (40 nm diameter) showing fluorescence were used. Finally, the measured step size was compared with the programmed step size and $\frac{dX}{d\phi}$ was adjusted accordingly.

2.1.7 Daily Alignment

As the components of the setup are subject to thermal drift, daily fine adjustments of some parameters are necessary to ensure a decent localization performance. To assess the

quality of the local minimum, MINFLUX tracking of 20 nm fluorescent beads (FluoSpheres 0.02 µm(660/680), Invitrogen Life Technologies, Waltham, USA) was performed. The quality can be improved by adjusting the power balance between the different beams, which in turn is achieved by fine tuning the angle of the half-wave plate 1 and by adapting beam position in the BFP with the galvanometer scanner. The half-wave plate modulates the power distribution between the beamlets. By changing the center scan position, fringe regions of the individual beams can be cut off, which allows for decreasing or increasing of the individual beam power. The usual aim was a measured SBR of 2-3 in both directions when performing MINFLUX localizations using $L = 30\,\text{nm}$.

2.2 Experimental Setup

To implement technical innovations presented in the previous sections that promise to improve the performance of MINFLUX measurements, a new scanning light microscope was built. The main components are schematically depicted in Figure 2.14.

For excitation, three single frequency CW Lasers are available. They deliver laser light with a wavelength of 642 nm (Cobolt Bolero, $P_{max} = 500mW$), 561 nm (Cobolt Jive, $P_{max} = 500mW$) and 488 nm (Cobolt Calypso, $P_{max} = 50mW$, all from Cobolt AB, Solda, Sweden). Various parameters, such as laser power and mode lock state, can be read out and controlled via a USB-Serial interface. For fast power control, an acousto optical filter (*AOTF*, 97-01776-0, EQPhotonics, Paolo Alto, USA) is employed. The polarization angle of the laser beam is tuned by half-wave plates ($\lambda/2$, achromatic half-wave plate, B.Halle, Berlin, Germany) to match it to the fiber polarization axis. The lasers are overlapped with dichroic beam splitters and coupled into a single mode polarization maintaining optical fiber (Thorlabs P1-405BPM-FC-5, Thorlabs Inc. Newton, USA) to ensure a clean single mode output PSF and sufficient parallelism of the multiple excitation wavelengths.

The phase scanner creates the desired PSFs and enables high-speed scanning with sub-nanometer precision.

After passing the phase scanner, the excitation beam is split with a 90:10 (R:T) non polarizing beam splitter cube (*BS1*, Thorlabs BS076, Thorlabs Inc. Newton, USA). The transmitted beam is again split by a glass plate and the transmitted beam is directed onto a power meter to monitor the laser power during the measurement procedure. The reflected beam is also split up again and the transmitted part of the beam is directed onto a CCD camera (*Cam 1*, Basler Ace acA1920-155um, Basler AG, Ahrensburg, Germany), showing an analog of the beam shape and position in the BFP of the microscope objective.

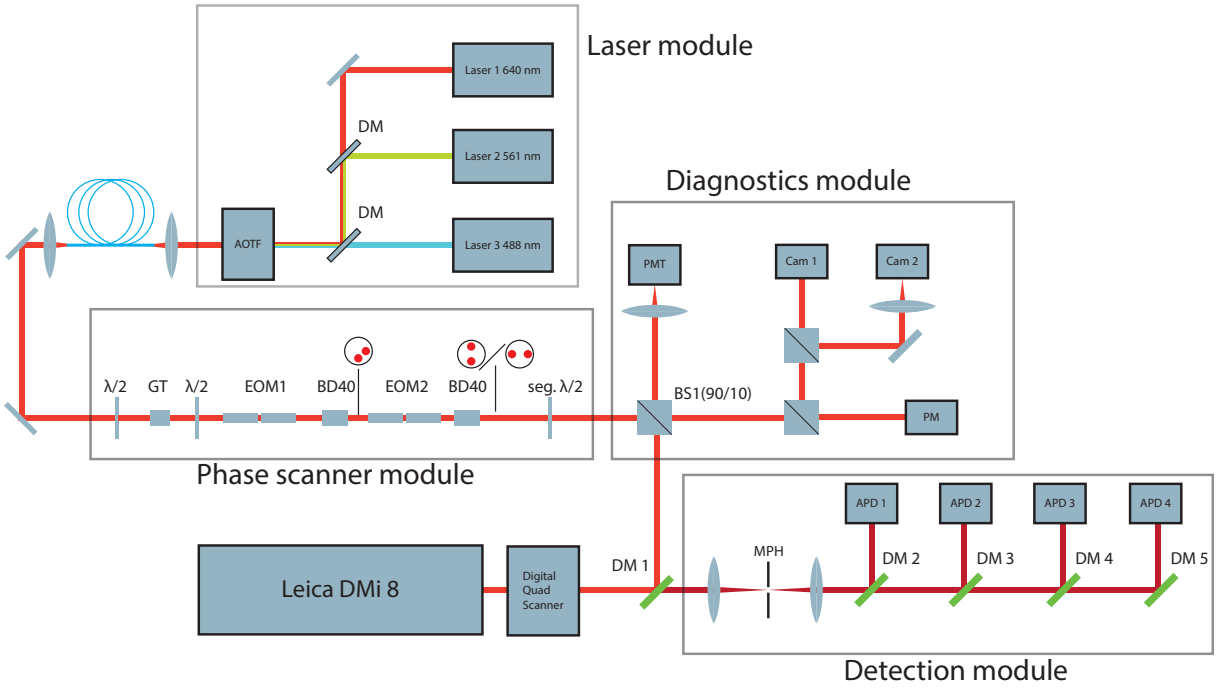

Figure 2.14: Scheme of the custom-built experimental MINFLUX setup
Laser module: optical bench with multiple excitation laser lines and fast intensity control via acousto optic tunable filter (AOTF), **Phase scanner module**: generation and fine scan of desired PSFs in a diffraction limited area, **Beam diagnostics module**: Power meter (PM) and cameras to monitor various beam parameters (position and intensity) of the beamlets. photon multiplier tube (PMT) to collect reflex light, **Digital galvanometer quad scanner**: enables scans with large FOV, up to 35x35 µm, **Leica DMi8**: microscope body for sample inspection with beam path coupled in by the rear infinity port, **Detector Module**: shielded box with motorized pinhole (MPH) and avalanche photon diode detectors (APD), **Hardware control**: computer running custom-written LabView software for data recording and parameter control, field programmable gate array (FPGA) board for real time measurement control (not depicted)

The reflected beam is focused onto a second CCD Camera (*Cam 2*, Basler Ace acA1920-155um), delievering a low NA equivalent of the PSF that is created in the focal plane.

The beam that is initially reflected by the first beam splitter cube (BS1, 90:10) is coupled into the microscope beam path by a quad band dichroic mirror (*DM1*, ZET 405/488/561/640m-TRFv2, Chroma Technology, Bellows Falls, USA) and is directed into the galvanometer scanner. It contains four galvanometric scanning units with high resolution digital sensors and encoders (GM-1015 with Ag mirrors, Canon Precision Optical Industry Co. Ltd., Tokyo, Japan) in a QuadScanner geometry encased in a custom-designed and custom-built brass mount [31, 32]. Brass is preferred in comparison to other materials due to its higher density leading to lower resonance frequencies and higher heat capacity. The additional mass reduces the momentum that is transmitted to the optical table when the scanners perform fast changes of the scanning position e.g. when the flyback of a confocal scan is initiated. The galvanometer scanners are steered by two controllers (Canon GC-211), each powering one x and one y galvanometer for better load distribution. The

resolution of the galvanometers digital encoders is below 1 nm with respect to the object space. The positional jitter of the feedback regulation is about 0.5 nm in the object space. The galvanometric scanning unit was used to perform confocal scans for finding molecules of interest in a FOV of $\sim$ 35x35 µm.

The beam that emerges from the QuadScanner is coupled into the rear infinity port of the Leica DMi8 microscope body (Leica Microsystems, Wetzlar, Germany) which provides an extra wide chromatic correction range. For all measurements within the context of this thesis, a Leica HC PL Apo 1.44 100x Objective Lens (Leica Microsystems, Wetzlar, Germany) was used.

The sample is placed on a custom-built sample stage powered by piezo linear-actuators (SLC1730, Smaract GmbH, Oldenburg, Germany). Their positioning resolution is below 1 nm at a maximum travel distance of 21 mm. The fluorescence light that is collected by the objective travels back the beam path, passes the quad band dichroic mirror (Figure 2.14, DM1) and is focused into a motorized pinhole device (*MPH*, Thorlabs MPH16-A, Thorlabs Inc. Newton, USA). The pinhole size can be adjusted from 25 µm to 2 mm corresponding to 125 nm to 10 µm in the object space. It allows to control the level of confocal blocking of out-of-plane light. The beam is collimated at the output of the MPH and split into different fluorescence channels by a cascade of dichroic filters. For optimal laser blocking, two of each filter type are installed in front of the corresponding detector (Table 2.1). For detecting the fluorescence light avalanche photo diode detectors (*APD*, SPCM-AQRH-13-ND, Excelitas Technologies Corp, Waltham, USA) are employed.

Table 2.1: Overview of bandpass filters that are used at low angle of incidence, acting as dichroics in the filter cascade All filters were manufactured by Idex Corp., Lake Forest, USA

Channel 1 (blue)	DM 2	417 – 477 nm	Semrock 447/60 BrightLine HC
Channel 2 (green)	DM 3	500 – 550 nm	Semrock 525/50 Brightline HC
Channel 3 (yellow)	DM 4	574 – 626 nm	Semrock 600/52 Brightline HC
Channel 4 (red)	DM 5	662 – 800 nm	Semrock 731/137 Brightline HC

Scattered or reflected laser light emerging from the sample is reflected by the quad band filter DM1, passes the beam splitter cube (*BS1*) and is focused into a 50 µm pinhole. The light that passes the pinhole is collected by a photon multiplier tube (*PMT*, H14119-40, Hamamatsu Photonics, Hamamatsu, Japan). The scattered/reflected light image contains information about local changes of the refractive index of the sample in contact with the cover slip. It also helps to find the imaging plane by focusing on the coverslip/sample interface reflex.

Due to the fast measurement procedure, a field programmable gate array board (*FPGA*, PCIe-R7852r, National Instruments, Austin, USA) with a base clock of 100 MHz is em-

ployed for real-time control of the data acquisition. It features eight analog outputs (AO) with a precision of 16 bit updating at 1 MHz refresh rate, eight analog inputs (AI) with 16 bit precision and a refresh rate of 750 kHz as well as 96 digital in/outputs (DIO) to control all components involved in the measurement procedure e.g. HVAs controlling the electro-optic voltages, the AOTF for laser power control and APDs to collect and accumulate photon counts of the different detection channels. It is programmed with LabView (National Instruments) FPGA such that after each localization it is able to calculate a new emitter position. Then it adjusts the hardware parameters accordingly. The measurement configuration is controlled via a custom-written LabView software that communicates with the FPGA board. An additional software reads out the first-in-first-out (FIFO) memories of the FPGA that contains the localization data and various system parameters.

2.3 Estimator Considerations

To calculate the 1D position from the measured counts during a MINFLUX measurement different estimators were applied depending on the situation at hand. In imaging situations and for the real-time position estimation on the FPGA board we used the explicit formulation of a parabolic fit. When evaluating single molecule traces in post-processing the collected counts were analyzed with a modified estimator that included ensemble information about the trace into the position estimate. We called it 'Fixed-Curvature Estimator'.

2.3.1 Parabolic Fit

For imaging experiments and the position calculation on the FPGA board we used a deterministic estimator that follows from equation

$$x_m = \frac{y_3 - y_1}{y_3 - 2y_2 + y_1} \tag{2.4}$$

For the derivation refer to Section 1.3.3. This estimator has the advantage that it is quick to calculate and implementable in hardware. It returns a position estimate from a single measurement consisting of the three exposures at $x_m - \frac{L}{2}$, x_m and $x_m + \frac{L}{2}$. Its disadvantage is its disposition to produce bad correction estimates in certain situations. This occurs if the denominator of the fraction diverges in low contrast situations. To make the measurement, and therefore the centering of the molecule by correcting the position more robust against outliers we limited the range of the correction x_m that the FPGA board performs during a measurement to a maximum value of $\frac{L}{2}$. This decreases the negative effect of short time blinking of a dye during which the collected counts $y_{1,2,3}$ are random counts generated by the background. Without this limitation arbitrarily large calculated corrections can occur which will deteriorate the quality of following localization attempts.

2.3.2 Fixed-Curvature Estimator

For the post-processing data evaluation of tracking experiments, we used a modified estimator which we call the Fixed-Curvature Estimator. This estimator assumes that the curvature of the convolution of excitation PSF and the single molecules fluorescence response will be the same over the whole single molecule trace. Under this assumption it is possible to use more than just the information of the current three exposures to calculate

the 1D position. First the average curvature over all localizations $i = 1, \ldots, N$ of a single molecule trace is calculated:

$$\overline{c} = \frac{1}{N} \sum_{i=1}^{N} \frac{2(y_{1,i} + y_{3,i} - 2y_{2,i})}{L^2} \tag{2.5}$$

The correction for an individual measurement then amounts to

$$x_m = \frac{y_3 - y_1}{4L\overline{c}}. \tag{2.6}$$

As more information is included, the measurement becomes more robust in comparison to the direct estimator. The individual measurements of y_2 do not enter the calculation. This is especially beneficial in low contrast situations or when less than 10 photons per localization are collected. Under these circumstances the parabolic fit estimator tends to become less precise or diverges because a small fluctuation of the measured counts of the central exposure y_2 can have a large influence on the position estimate. Because the curvature is calculated from the ensemble of all 1D localizations, the high sensitivity to fluctuations of y_2 is omitted.

2.4 Additional Methods

2.4.1 Emitter Position Calculation from Confocal Scan

To find suited emitters to perform MINFLUX localizations typically a confocal scans on the sample of interest was carried out. The collected data was evaluated with the custom-written LabView *VI find positions.vi*. Its purpose is to extract positions of emitters (fluorescent beads/single molecules or gold nano particles) from the confocal scan by fitting 2D Gaussian distributions around spots of high intensity. The extracted positions were filtered by amplitude and distribution width of the Gaussian fit. Additionally, the distances between the found positions were calculated and emitters with a separation of less than 500 nm were excluded. Thereby having multiple emitters fluorescing simultaneously in a diffraction limited area could be prevented.

2.4.2 Fitting of Discrete Steps in Tracking Experiments

The tracking experiments described in Sections 4.4.2 and 4.4.3 investigate position traces of the complexes of interest that feature discrete steps. To find abrupt changes in the recorded position data the Matlab function *ischange* was employed [33, 34]. It detects

change points of a vector of data A if the vector can be split into two segments A_1 and A_2 if the inequality specified by

$$C(A_1) + C(A_2) + \tau < C(A) \tag{2.7}$$

is fulfilled with τ being a threshold parameter and C representing a cost function. The cost function measures the difference between the mean of a segment A_i and the segment itself. To determine the number of change points k and their locations, *ischange* iteratively minimizes the sum of cost functions to fulfill the inequality

$$C(A_1) + C(A_2) + ... + C(A_k) + k\tau < C(A). \tag{2.8}$$

To detect steps in the experimental data with *ischange* the parameter 'MaxNumChanges' was set. This limits the amount of change points to the specified number. The function automatically calculates a suited threshold parameter τ to accommodate to the setting of 'MaxNumChanges'. For the nanorobot tracking experiments in Section 4.4.2 'MaxNumChanges' was set to an average number of expected steps, that was calculated from the trace length and the expected stepping frequency. When reviewing the traces individually no large errors were found when choosing the parameter in this way. For the kinesin tracking experiments in Section 4.4.3 the approximate number of steps was calculated from the separation between the start and end position of a trace Δ_x after the formula $N = \frac{\Delta_x}{16\,\mathrm{nm}} + o$. This was chosen, as the expected step size of the kinesin heads was $\sim$16 nm. The offset o was added to take the possibility of smaller step sizes into account. o was varied and the number of detected change points was most consistent for $o = 3$. All traces were evaluated with these parameters and reviewed individually to check the suitability of the chosen parameters. Overall, a good agreement of the step fit with the position traces was found.

2.4.3 Beam Multiplexing

As described in Section 1.3, during a MINFLUX localization the position of the probing minimum is rapidly moved around the estimated molecule position. After a triplet of exposures at positions $-L/2$, 0 and $L/2$ relative to the current position, a new molecule position along the probed axis is calculated from the collected photon counts. Typically, the time for an exposure is chosen such that 10 – 30 photons are collected per 1D localization. For this reason, dwell times in the range of some tens of microseconds to some hundred microseconds are used. During this time span it is possible that the molecule transfers to a longer lived dark-state. If a molecule is centered well and emitting con-

stantly, the counts collected during the two outer exposures are similar. However, if the molecule transfers to a dark state it can occur that although the molecule is already centered, the collected photon counts can show a large disparity due to the temporal sequence they are measured in. This is depicted in Figure 2.15.

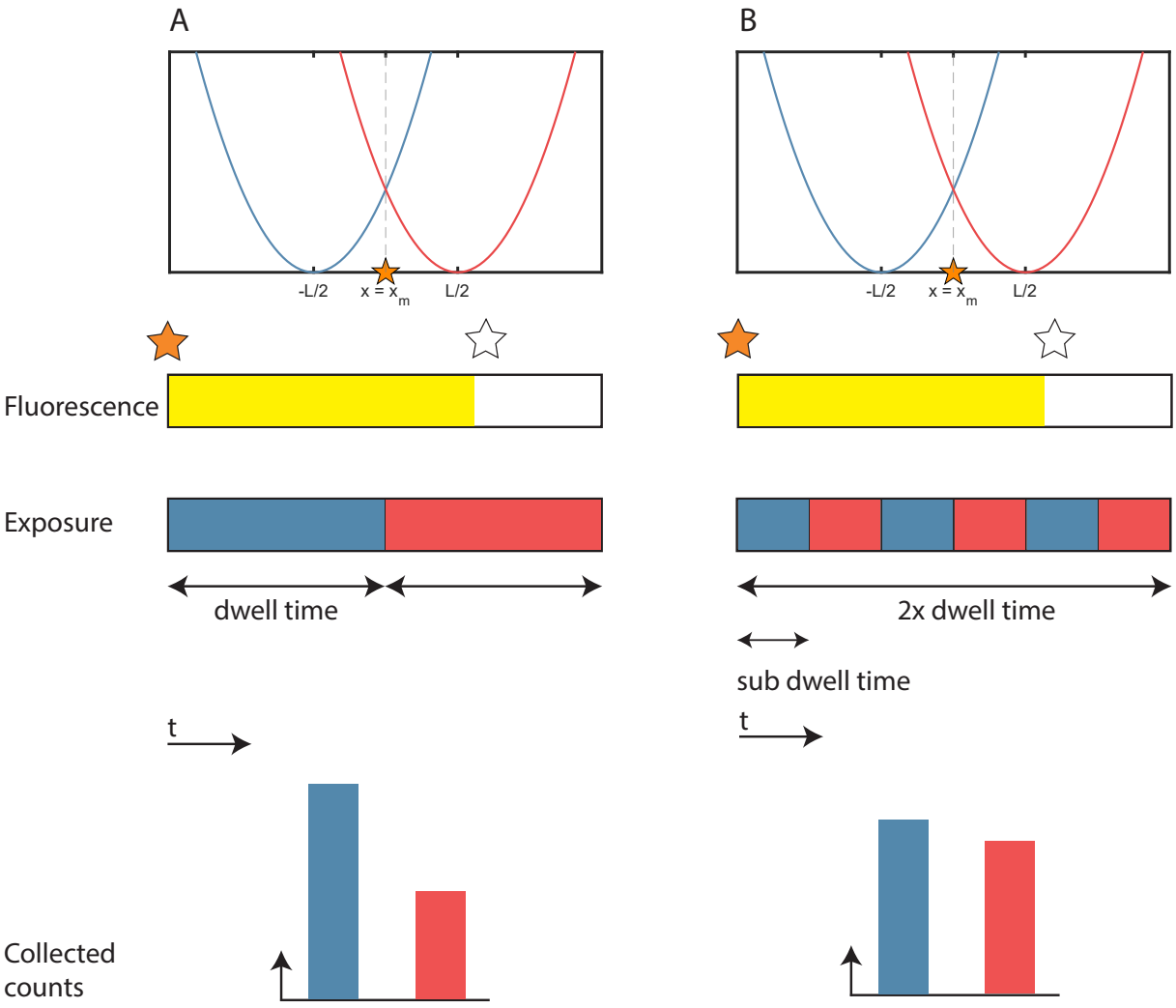

Figure 2.15: Beam multiplexing reduces position estimation errors when fluorophore turns dark, **A** If a fluorophore transitions to a dark state the effective dwell time for the two outer exposures can differ strongly. Even if the molecule is perfectly centered in the MINFLUX pattern and the same number of detected photons is expected, a large imbalance can result. The calculated position estimate can be skewed due to the temporal sequence of the different exposures. To reduce the negative influence of this effect the measurement scheme in **B** was applied. Instead of exciting the molecule continuously for one dwell time at the first beam position and then continuously for a second dwell time at the second beam position, the excitation PSF's minimum position is alternated in rapid succession between the two. Through this approach, the off-time of the fluorophore is distributed more evenly and the error of the calculated position is reduced. To increase the comprehensibility, the central exposure was omitted in this explanation because the influence of the counts collected during the central exposure is minor.

The potential error in the calculated position can be arbitrarily large. To reduce this position calculation error, a routine was implemented in the FPGA control software that allows to switch with high frequency between the three exposure positions and collect counts for a certain number of repeats of a sub-dwell time without calculating a position correction and repositioning the scanner accordingly. The relative error was then limited to the ratio of sub-dwell time and dwell time. By multiplexing faster than the collected fluorescence rate the error could be reduced such that the maximum disparity for a centered emitter position is a single photon. This multiplexing process was used to reduce the effect of dark-states during the single emitter measurements. Because there are measurements where multiplexing is unfeasible, we additionally limited the maximum correction to $\frac{L}{2}$.

2.5 Sample Preparation

In the following, the sample preparation for the samples measured in Chapter 3 and 4 will be laid out.

2.5.1 Coverslip Preparation

Cleaning Procedure

Cover slips (170 µm, No 1.5H, Paul Marienfeld GmbH & Co. KG, Lauda-Königshofen, Germany) with widths from 15-18 mm were used. First they were wiped with lint-free cloth sprayed with acetone. Subsequently they were wiped with a cloth sprayed with Isopropanol. After rinsing with Isopropanol the cover slips were dried under nitrogen flow. Afterwards they were plasma cleaned (oxygen) for 5 minutes at 200 W.

Flow Chamber Construction

For easy exchange of incubation solutions during preparation, as well as change of buffers in between experiments, flow chambers were prepared. For this purpose, two narrow strips of double-sided tape (Scotch Double Sided Tape, 3M, Saint-Paul, USA) were glued onto an object carrier to form a channel with a width of ∼5 mm. A cleaned coverslip was put on top of the tape and attached by applying light pressure.

PLL-PEG-bt-stv Surface Functionalization

The procedure was developed by Lukas Scheiderer[1].

The polymer layer that is formed by the PLL-PEG-bt-stv construct prevents dye molecules from sticking to the glass surface. Surface sticking can potentially restrain the rotational degrees of freedom of the single molecules. This could arrest the electric dipoles of the fluorophores to a certain orientation. Such a fixed orientation would result in an asymmetric excitability for the two perpendicularly polarized excitation beam axes and the localizations precisions would differ strongly for x and y. First the coverslip is coated with PLL-PEG (PLL: Poly-L-Lysin and PEG: Polyethylene glycol) and functionalized with Biotin (bt). For this purpose, the flow chamber is incubated with 10 µl of a solution with PLL-PEG-bt (0.2 mg/mL) and 1%Vol Tween (P20) for 5 min. The flow chamber is then washed with 100 µl PBS to remove the functionalization solution. Then the chamber is incubated with 2x10 µl Streptavidin (1 mg/ml 1:100 in PBS) for 5 minutes. Afterwards the chamber is again washed with 100 µl PBS. The chamber is then ready for further preparation.

2.5.2 Preparation of Atto647N Single Molecules

The single molecule samples were prepared with a surface functionalization according to Section 2.5.1. The chambers were then incubated with 2x10 µl Atto647N-biotin conjugate (Atto647N-bt) for 5 min. Typically concentrations of 10 pM in PBS were used. Subsequently the chambers were washed three times with 100 µl PBS. For imaging or tracking experiments the flow chambers was then filled with a mixture of PBS+1% VectaCell (Vector Laboratories Inc., Burlingame, USA). VectaCell contains the antioxidant Trolox in filtered ethanol and prevents the formation of reactive oxygen species such as Singlet Oxygen $^1O_2$ [35].

2.5.3 Preparation of Cy3B Single Molecules

The samples were prepared according to the protocol for Atto647N single molecules. Instead of biotinylated Atto647N, a Cy3B-biotin conjugate was used with a concentration of 10 pM.

[1]Department for Optical Nanoscopy, Max-Planck-Institute for Medical Research, Heidelberg, Germany

2.5.4 Preparation of DNA Origami Nanorobots

The samples were prepared by Dr. Jessica Matthias[1].

Flow chambers were prepared with functionalized coverslips according to Section 2.5.1. After washing with 100 µl PBS the flow chambers were incubated two times for 5 min with 10 µl of a solution containing the baseplate DNA origami (30 nM), diluted 1:500 in 1x TAE Buffer containing 20 mM $MgCl_2$ (TAE-$MgCl_2$) for stabilization of the DNA origami. Subsequently they were washed with 100 µl TAE-$MgCl_2$. The chambers were then incubated with 2x10 µl of the solution containing the DNA origami Nanorobots (100 µM diluted 1:5000k in TAE-$MgCl_2$). After washing two times with 100 µl TAE-$MgCl_2$ the flow chambers were filled with TAE-$MgCl_2$ containing 1% VectaCell as imaging buffer.

2.5.5 Preparation of Kinesin-1 Samples

The following protocols were developed by Lukas Scheiderer[1] who also prepared the kinesin samples for the measurements shown in Section 4.4.3.

Expression of Kinesin A cysteine-light truncated (∼560 residues per monomer) human kinesin construct was expressed in E. coli using a mutated plasmid (K560CLM T324C, #24460, Addgene, Watertown, USA) as described by Tomishige et al [36]. The construct contains a single solvent-exposed cysteine at amino acid position 324 on the kinesin head and a C-terminal His6-Tag. The expressed protein was aliquoted, flash frozen in liquid nitrogen and subsequently stored at −80° C.

Labeling of Kinesin Kinesin was reacted with Atto 647N maleimide (Atto-Tec GmbH, Siegen, Germany) over night at 4° C. Excess dye was removed from the labeled protein fraction by size-exclusion chromatography (PD MiniTrap™ G-25 Sample Preparation Column, Cytiva Life-Science, Marlborough, USA). The degree of labelling (DOL) was determined by UV-Vis spectroscopy (DS-11+ Spectrophotometer, DeNovix, Wilmington, USA). Sucrose (Sigma Aldrich, St. Louis, USA) was added to a concentration of 10% (w/v) and aliquots were flash-frozen in liquid nitrogen and stored at −80°C.

Preparation of Microtubules Functionalized and fluorescent microtubules were polymerized from purified tubulin (88% Cycled Tubulin, 10% bt-Tubulin, 2% AF488-Tubulin).

[1]Department for Optical Nanoscopy, Max-Planck-Institute for Medical Research, Heidelberg, Germany

The lyophilized tubulin was suspended in PEM80 buffer (80 mM Pipes, 0.5 mM EGTA, 2 mM $MgCl_2$, pH 7.4) with 1 mM GMPCPP (Jena Bioscience, Jena, Germany). The solution was incubated for 30 min in a water bath (37° C) and polymerized microtubules were centrifuged off at 21,000x g in a bench-top centrifuge (Thermo Scientific™ Fresco™ 21 microcentrifuge, Thermo Fisher Scientific, Waltham, USA) for 15 min, washed with PEM and centrifuged off at 21,000x g for 15 min. The microtubule pellet was resuspended in PEM80, aliquoted, flash-frozen in liquid nitrogen and stored at −80° C.

Preparation of Microtubule Assay A flow chamber was constructed according to the procedure described in Section 2.5.1. The chamber was incubated with PLL-PEG-biotin (Susos AG Inc., Duebendorf, Switzerland), 0.2 mg/mL, ddH2O, 1% (v/v) Tween® 20 (Sigma Aldrich)) for 15 min, rinsed with PEM80, incubated with NVD, rinsed with PEM80, incubated with microtubules, rinsed with PEM80, blocked with BSA-bt and rinsed with PM15 (15 mM Pipes, 2 mM $MgCl_2$, pH 7.4). Labeled kinesin in measuring buffer (1 mM DTT, 1 mM Paclitaxel, 10 µg/ml BSA-bt, 1 mM methyl viologen, 1 mM ascorbic acid, ATP, PM15) was added in a hypoxia chamber and sealed with two-component sealant (picodent twinsil™, picodent Gmbh, Wipperfuerth, Germany) or nail polish.

Chapter 3

Single Emitter Localization Measurements

3.1 Introduction

To confirm that the phase scanner delivers an improved localization performance, we carried out test localizations on fluorescent single molecules. First, the localization scheme of single emitters will be described on a procedural and subsequently on a technical level. Second, the results of single molecule position traces recorded with Atto647N and Cy3B single molecules will be displayed. These two dyes were chosen because they are among the most photostable dyes in the main excitation bands of the setup (561 nm and 642 nm). In the experimental results it will be shown that the lateral localization efficiency in the last step of the iterative localization process is higher than possible for any conventional super-resolution microscopy technique. To evaluate the localization performance in comparison to the theoretical limits the contributions from different technical and environmental influences on the setup and the localization precision will be analyzed.

3.1.1 Data Acquisition

We started each measurement by performing a confocal pre-scan. To find the positions of fluorescent emitters the resulting image was analyzed with the custom-written LabView Vi *find positions.vi*. For details refer to Section 2.4.1.

All suitable emitter positions were sequentially targeted with the galvanometer scanner and MINFLUX traces were recorded. Using the phase scanner for the fine positioning

of the beam, we employed an iterative localization scheme. After a two-step zoom in process with larger beam separation L the step with the smallest L was repeated for a configurable number of iterations (N). When a 2D localization was completed the position of the probing intensity minimum was modified to the newly calculated position. This leads to a position trace with N data points containing the measured lateral position. In a tracking experiment these traces reveal the trajectory of the emitter. In the case of imaging the predominantly static position traces show the location of a single emitter. The standard deviation of the trace of immobile emitters allows to quantify the localization precision. To gain an image with sub-diffraction spot resolution, the localization approach must be combined with a molecular switching scheme [14, 19].

3.2 Experimental Results

3.2.1 Atto647N

For test localizations in the red excitation band we chose Atto647N because it is one of the most versatile and photostable single molecule dyes.

We first performed a confocal scan of 10x10 µm at a pixel size of 50 nm and a dwell time of 100 µs per pixel. We used laser 1 (640 nm) as excitation laser. The Atto647N single molecules were prepared as described in Section 2.5.2. The concentration was low (1-10 pM) in order to ensure that only a single dye molecule was located inside a diffraction limited spot.

In total 331 single molecule traces were recorded with the sequence described in Section 3.1.1. The dwell time per exposure was set to 100 µs. Including setup times, this resulted in a sampling time of 625 µs per 2D localization. We used a sub-dwell time of 10 µs resulting in a maximum error due to blinking of 10%. A three-step iterative MINFLUX procedure with beam separations L of 100, 60 and 16 nm was used. The last MINFLUX step was repeated 1000 times, resulting in 1000 2D position data points per trace. The collected counts were evaluated with the fixed-curvature estimator described in Section 2.3.2.

A representative example of such a trace is shown in Figure 3.1. Figure 3.1 **A** displays the position traces of x and y. The measured standard deviation was 2.20 and 2.21 nm in x direction and y direction. The trace was recorded at mean SBRs of 2.2 in both dimensions. The number of collected photons for the two localization directions are shown in Figure 3.1 **B**. The mean photon counts per localization were 14 and 16 respectively. Calculating

the theoretical optimum of the localization precision for the SBR in the present case according to formula 1.13 yields a standard deviation of 1.7 and 1.6 nm respectively. A deviation of roughly 30% can be explained by various environmental influences. Those will be discussed in detail in Section 3.3.

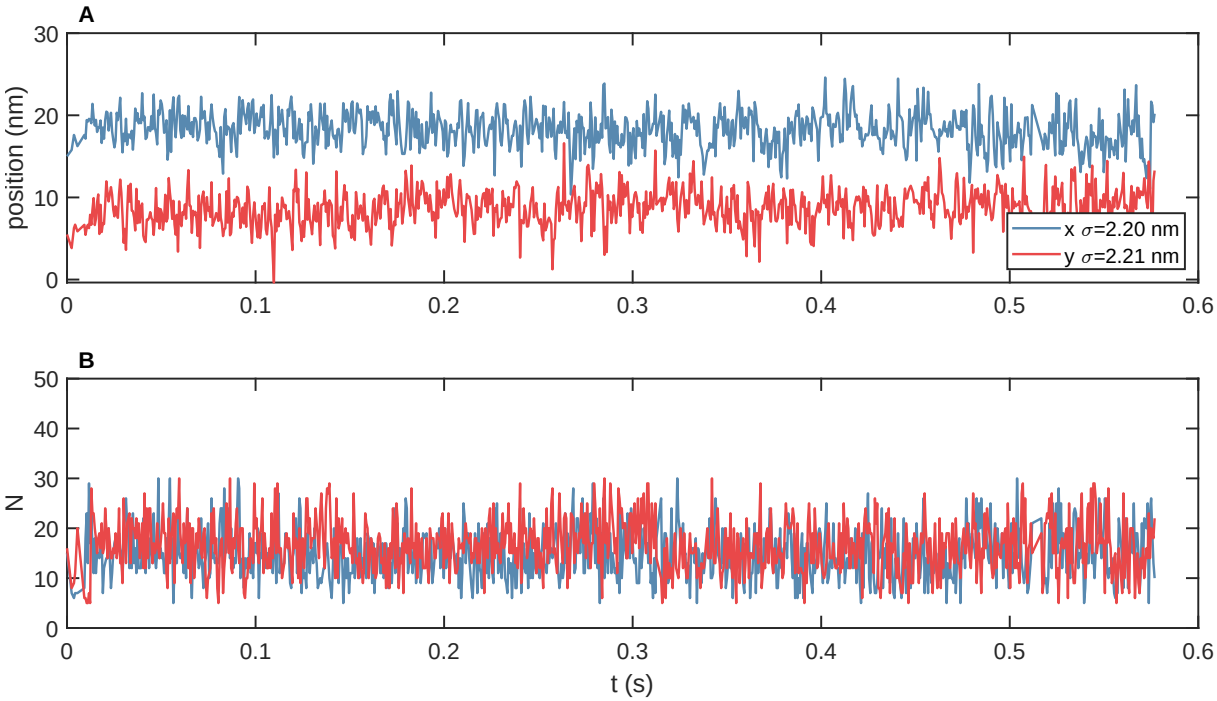

Figure 3.1: Representative MINFLUX trace of Atto647N single molecule, **A** shows the position trace for the alternating x(blue) and y(red) localizations. The trace was recorded with zoom in steps with L of 100 and 60 nm. The last step was repeated 1000 times with L=16 nm. The standard deviations in x and y are 2.20 and 2.21 nm respectively. The recorded photon counts are depicted in **B**. The average for x(blue) and y(red) was 14 and 16 respectively.

An overview of the experiment with n=331 such traces is shown in Figure 3.2. Here, only traces with an SBR≥1 were evaluated which resulted in a total of 312 traces. We calculated the standard deviation σ for the x and y position traces separately for each molecule trace. This includes all environmental influences like mechanical vibrations, sound and thermal drift during the measurement time. We also calculated the mean photon counts of all repeats in a trace. The standard deviation σ for each molecule trace is plotted over the average number of counts in the corresponding trace in a double-logarithmic plot to enable the assessment of the localization efficiency. Each of these localizations is represented by a data point in Figure 3.2 **A** for the x localizations and Figure 3.2 **C** for the y localizations. A curve of the form $\Sigma = \frac{a}{4\sqrt{N}}$ was fitted to all data points to showcase the average efficiency. For each trace, we also evaluated the mean SBR. An overview over their distribution is shown in Figures 3.2 **B** and **D** for x and y respectively. To enable a comparison to the theoretically achievable localization efficiency a curve that can be described by equation 1.13 was added. The deviation to the maximum efficiency amounts to roughly 43.4% in x-direction and 47.0% in y-direction . This can be

explained by non-negligible environmental influences. Those will be discussed in detail in Section 3.3.

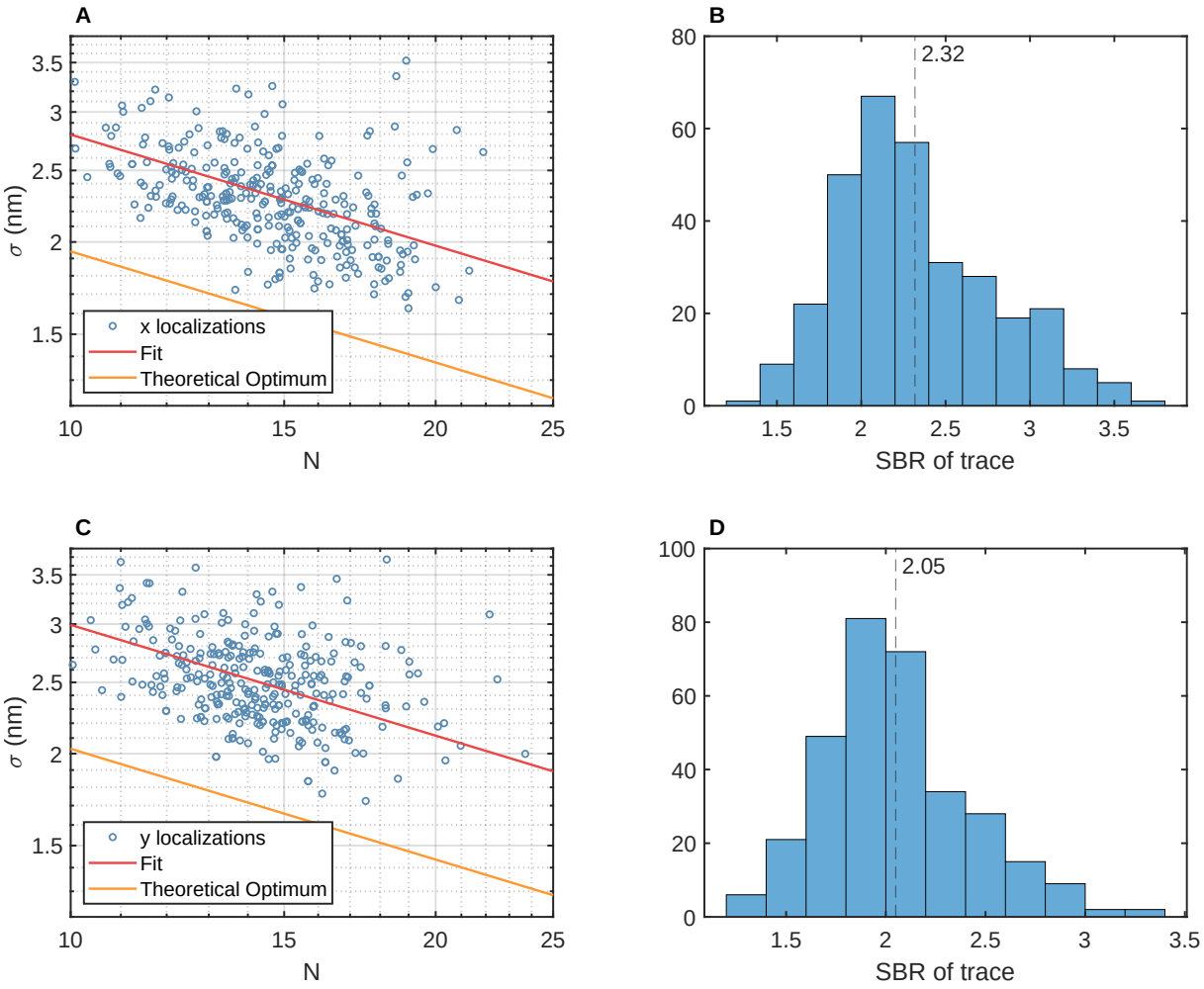

Figure 3.2: Overview over measurement series on Atto647N to assess localization efficiency Overall 331 single molecule traces were recorded with an iterative MINFLUX localization approach. The chosen dwell time per exposure was 100 µs which resulted, including the setup times, in a time per 2D localization of 625 µs. The last MINFLUX step was performed with $L = 16$ nm and was repeated 1000 times. Only traces with a mean SBR≥1 were included. **A** shows the mean standard deviation of the x-positions of each individual trace (blue circles) as well as a fit of the form $\frac{a}{\sqrt{N}}$ to the data points to reveal the average localization precision of the measurement series. The yellow curve depicts the best localization precision possible for the measured average SBR. An analogous Figure shows the data for the y-direction in **C**. Figures **B** and **D** depict a histogram of the measured SBR for the individual traces. The mean SBR was 2.32 for the x direction and 2.05 for the y direction. In x direction an average localization precision of 2.80 nm for 10 photons and 1.98 nm for 20 photons was reached. For the y direction a photon count of 10 yields a precision of 2.99 nm and a photon count of 20 a precision of 2.12 nm. In comparison to the theoretical optimum the precision in x and y direction are decreased by 43.4% and 47.0%. Possible reasons are discussed in Section 3.3.

3.2.2 Cy3B

To assess the localization efficiency in the second excitation band of our setup (561nm), we repeated the previously described experiment with immobilized Cy3B single molecules. We chose Cy3B, as it proved to be one of the most photostable dyes with an absorption maximum around 561 nm.

The samples were prepared according to the protocol in Section 2.5.3. The result of the experiment is depicted in Figure 3.3. A total of 273 traces with an SBR≥1 are shown. The traces were recorded with $L = 20\,\text{nm}$ in the last step. Figure 3.3 **A** displays the standard deviations of the individual traces in x-direction over the corresponding average number of collected photons. The result for the y-direction of the traces is depicted in Figure 3.3 **C**. **B** and **D** show the corresponding distribution of the SBR. The average SBR was 1.77 in x-direction and 1.78 in y-direction. When collecting 10 photons per direction an average precision of 2.68 nm and 3.56 nm was reached, respectively.

Again, curves of the form $\Sigma = \frac{a}{\sqrt{N}}$ were fitted individually to the data points of both directions. In comparison to the theoretical optimum at the measured SBR (yellow curve), the localization efficiency was decreased by about 22.4% and 32.8%, respectively. The large number of data points located below the optimum curve stem from the large width of the SBR distribution (1.0 - 5.9). As the curve shows the optimum for the average SBR, single data points can exceed this average optimum.

In comparison to the data set that was recorded on Atto647N single molecules, the localization efficiency was slightly lower. The predominant reason for this was the lower SBR for the Cy3B data and the resulting larger L that was used. The SBR can be decreased by a higher residual intensity in the PSF's minimum. Because the excitation wavelength, the detector path and the employed APD differ for the two experiments, additional background contributions from outside the sample can also play a role. On top of that, Cy3B exhibited much stronger molecular blinking and short intermittencies of the fluorescence. Despite the multiplexing approach described in Section 2.4.3, this can lead to a decreased localization precision of the position trace. In comparison to the data for Atto647N the deviation from the theoretical optimum was smaller for Cy3B. This has multiple reasons. The equation for this curve takes the lower SBR into account. Additionally the overall lower precision due to the lower SBR and fewer detected photons masks the noise floor that stems from positional jitter caused by factors from outside and inside the setup. Those will be discussed in the Section 3.3.

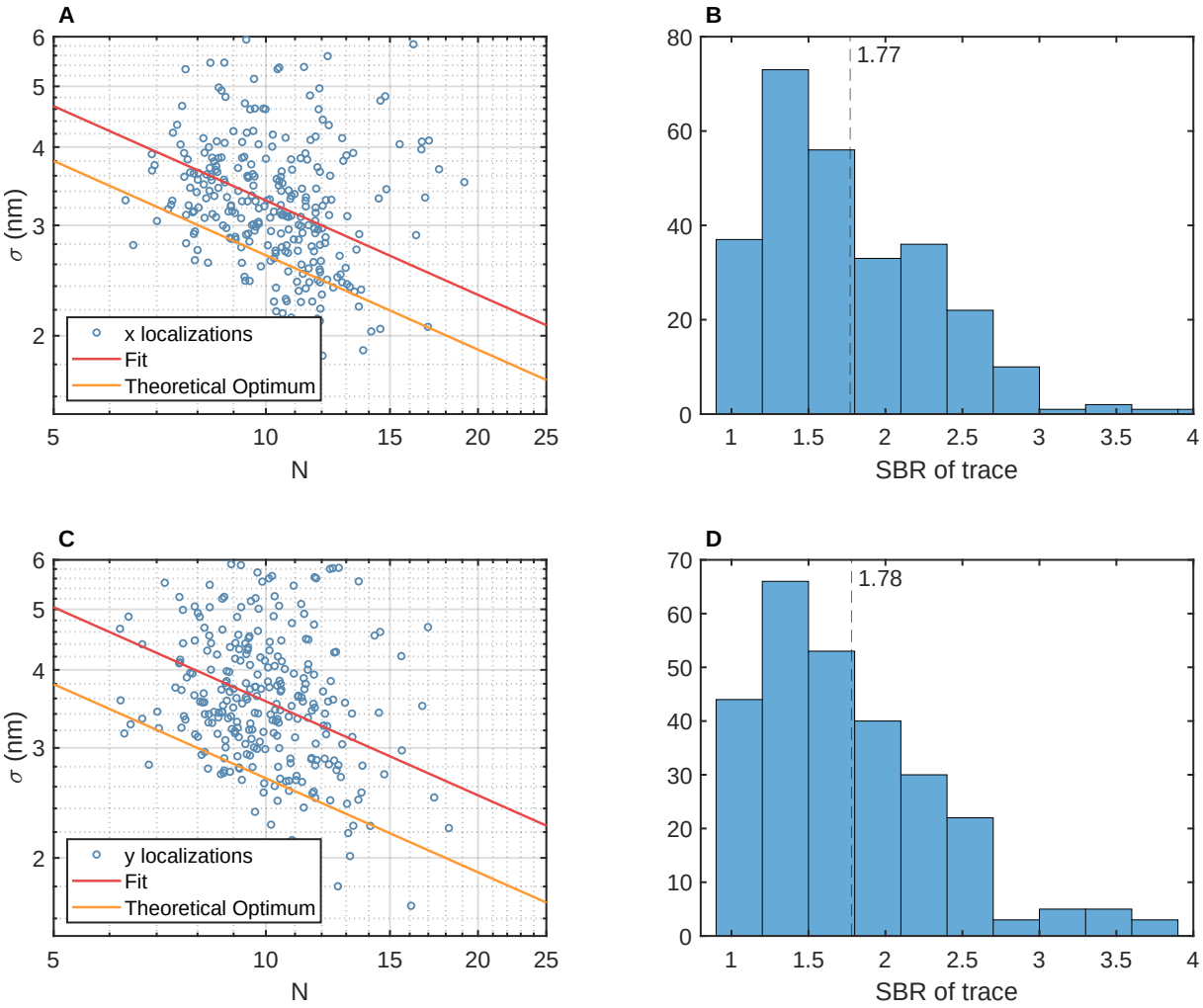

Figure 3.3: Overview over measurement series on Cy3B to assess localization efficiency For this measurement 273 single molecule traces recorded with an iterative MINFLUX localization approach were evaluated. The chosen dwell time per 2D localization was 625 µs. The last MINFLUX step was performed with $L = 20$ nm for 1000 repeats. Again, only traces with a mean SBR≥1 were included. **A** displays the mean standard deviation of the x-positions of each individual trace (blue circles) as well as a fit of the form $\frac{a}{\sqrt{N}}$ that describes the average localization precision of the measurement series. The yellow curve depicts the best localization precision possible for the measured average SBR. An equivalent to the Figure showing the data for the y-direction is displayed in **C**. Figures **B** and **D** depict a histogram of the measured SBR for the individual traces. The mean SBRs for x and y were 1.77 and 1.78, respectively. The average localization precision for N=10 collected photons was 3.29 nm and 3.56 nm for x and y direction. The curve for theoretical optimum is calculated for the mean SBR of the localizations of the corresponding dimensions. Due to the large spread of SBRs (1.0 to 5.9) for Cy3B, some of the data points can reach a precision that is better than the theoretical optimum of the ensemble.

3.2.3 Summary and Discussion

It was shown that, using our setup we were able to localize single molecule emitters with high precision and efficiency. For the case of Atto647N single molecules the best traces reached a standard deviation of <2 nm with 13-20 collected photons per dimension. When localizing Cy3B single molecules, a standard deviation of <3 nm was achieved when collecting 12-20 photons per dimension. Due to the slightly worse SBR that was reached the localization efficiency was not as high as in the case of 4Pi-MINFLUX [37]. The SBR was presumably decreased by residual position jitter and non-negligible intensity in the PSF's minimum. Due to limited rigidity of the construct that immobilizes the emitter, it is possible for the emitter to wiggle around stochastically in a range of multiple nanometers with high frequency. If this movement is much faster than the sampling frequency of the measurement, it is not resolved. The localization then shows the center-of-mass of the jitter. Nonetheless, this movement can decrease the SBR, because even when perfectly centered in the minimum, the molecule can shortly move into regions with higher excitation intensity. The main source of background is most likely the non-zero intensity in the local minimum of the excitation PSF. PSF calculations show that this can arise if the beams that are overlapped to create the probing PSF have unequal laser power. Then the destructive interference cannot lead to an total extinction. Another reason are wavefront distortions of the beamlets that emerge when they pass the various optical components. The local divergence from a flat wavefront can further decrease the extinction efficiency.

Nonetheless, the shown measurements showcase the remarkable localization efficiency that MINFLUX enables for yellow-fluorescing, as well as red-fluorescing single molecules. Small improvements in the SBR could allow to reach a localization precision below one nanometer with only 20 collected photons per dimension.

3.3 Environmental Influences on the Localization Precision

A number of environmental influences can lead to a decreased localization precision in comparison to the theoretically achievable optimum. In general the assessment of the multicausal individual noise sources and their impact on the measurements are difficult to disentangle and quantify. In the following, only the predominant sources and counter measures are considered.

3.3.1 Vibrations Originating from Building

One major noise source are vibrations caused by people moving about near the laboratory. Instruments or devices like vacuum pumps or components of the ventilation system that are located close to the microscope can also introduce additional noise. These vibrations are mainly in the low frequency region from 0.5 Hz to 80 Hz. Higher frequencies are attenuated and not transmitted via the building walls and doors [38]. To reduce the influence of the residual transmitted disturbances, we moved the MINFLUX microscope to a basement laboratory. Here building vibrations are lower as the surrounding walls and the floors are in direct contact with the foundation and therefore dampened further. To minimize the number of people working in the vicinity, the microscope is the only setup in the laboratory. By placing the whole optical table on pneumatic active vibration isolation supports (PTS601, Thorlabs) low frequency vibrations are prevented from coupling into the setup.

3.3.2 Vibrations Originating from Inside the Laboratory

To evaluate the most prominent noise frequencies we recorded MINFLUX traces with high spatio-temporal resolution on fluorescent beads or gold nanoparticles. Due to their higher photostability they can be excited with higher laser power and yield higher fluorescence or scattering rates. We applied a fast Fourier transformation (FFT) to the position traces. The result shows the amplitude of noise over the vibration frequency. By sequentially turning off devices, the peaks that disappear from the noise spectrum were assigned to the corresponding device. Resonant vibrations of surfaces or constructions can be dampened by attaching viscoelastic material with high density. All devices with noticeable fan volume were replaced with low-noise equivalents or passively cooled devices. The encapsulation of the optical setup was covered with noise reducing foam mats with butyl cover (PurSkin, Sonatech, Ungerhausen, Germany).

The sample stage was further encapsulated in a Plexiglas box to increase the temperature stability as well as shield the sample stage and the sample. An additional layer of dampening and darkening material was added for noise reduction.

3.3.3 Vibrations Originating from the Setup

The galvanometers of the quad scanner setup have a certain positioning precision depending on the precision of the galvanometer sensors regulation. The larger the optical path

length between the galvanometer mirrors and the intermediate image in the center of the scanner setup, the larger the position jitter that is created by the regulation's fluctuations will be. In our setup the distance of the furthest mirror to the intermediate image was 25.0 mm. The angular accuracy in the high precision mode of the Canon Galvanometer controllers is stated to be 0.51 µrad. As the focal length of the lenses creating the intermediate image is f=200 mm this results in a position jitter of ∼1 nm.

3.3.4 Resonant Oscillation of Stage and Stage Controller

Although the positioning resolution of the encoder of the SmarAct piezo stage is about one nanometer, we found a significant residual jitter. The feedback regulation of the stage excited a resonant oscillation of the sample stage construction. This limited the achievable localization precision to ∼ 2 nm. We set the regulation parameters such that after positioning the sample stage, the dynamic feedback loop was turned off. Going forward, the piezo actuators simply held the voltage to keep the stage position from drifting. To limit the impact of the resonant oscillation of the sample stage being excited by sound and vibrations, we attached viscoelastic rubber material with high density for dissipation.

3.3.5 Dye Linker Length and Rigidity

To prevent direct electronic interaction and steric hindrance fluorophores are often attached with flexible linkers for example C6 hexamethlyen [39]. Their length can be up to 2 nm. The fluorophores can diffuse around, held in the vicinity to their attachment point by the linker. This movement typically occurs on a time scale far below the sampling frequency. Nonetheless, it can lead to a decreased SBR, because during a single exposure the molecule repeatedly moves away from the low intensity minimum of the probing PSF. The strength of the effect depends on the oscillation amplitude.

3.4 Summary and Discussion

In this chapter, the measurement procedure that was employed to assess the localization precision and the localization efficiency of the presented setup was described. We showed that when localizing Atto647N single molecules on average a localization precision of about 2.28 nm for 15 collected photons in x-direction or 2.44 nm for 15 collected photons in y-direction was achieved. The best localizations reached a precision of 1.63 nm for 19

collected photons in x-direction and 1.72 nm for 18 photons in y direction. In comparison to the theoretical optimum given the measured SBR the average localization efficiency was about decreased by about 43.4% in x-direction and 47.0% in y-direction.

For the experiment on Cy3B single molecules, an average localization precision of 3.29 nm in x-direction and 3.56 nm in y-direction when collecting 10 photons was achieved. The traces with the highest precision reached 1.43 nm at 18 collected photons in x-direction and 1.67 nm for 16 collected photons in y-direction. At the average measured SBR of 1.78 and 1.77 for x- and y-direction the mean localization precision was about 22.4% and 32.8%, respectively lower than the theoretical optimum. It should be noted that a camera-based method would require to collect more than 3000 photons to achieve a precision of 2 nm.

We attribute the deviations from the theoretical poisson noise limited localization precision to various environmental influences. Those were discussed in detail in Section 3.3. The most important contributors are vibrations coupling into the setup from the building, the laboratory and from components inside of the optical setup. Through various measures we could decrease the influence of these adverse impacts. Further improvement of the stability is necessary to reach the localization precision range below a single nanometer without averaging over longer measurement times. Replacing the galvanometer scanner with a piezo-electrically powered scanner could lead to a better high frequency stability of the beam position because no constant feedback regulation is necessary to hold a position. The drawbacks are a slower scanning speed and a smaller FOV. A stage that is overall more rigid and without strongly resonant parts will be required. Special attention must also be paid to the rigidity and lengths of the linkers attaching the fluorescent single molecules to the immobilizing construct or the complexx of interest in a sample. The Brownian motion of a freely swinging fluorophore tethered by a linker to the surface must be limited as much as possible to gain the ultimate localization precision.

Chapter 4

MINFLUX Tracking

The previous chapters described the implemented MINFLUX localization approach and emphasized the remarkable increase in localization efficiency in comparison to conventional super-resolution microscopy techniques. As MINFLUX requires drastically fewer photons to gain a certain localization precision, photons can be spent to increase the temporal resolution.

This chapter presents the consequent application of this high efficiency: MINFLUX tracking provides access to spatio-temporal resolutions (STR) that were so far unattainable by fluorescence nanoscopy. We have demonstrated that MINFLUX advances single molecule tracking to hitherto inaccessible areas.

First, the current state of single molecule tracking is discussed in general. Second, the theoretical boundaries of the MINFLUX localization approach and how it compares to camera-based tracking methods, the most common tracking method, are reconsidered. The theory promises a large increase of the spatio-temporal resolving power by MINFLUX. Third, proof-of-principle experiments are displayed which confirm that the theoretical superiority also translates to remarkably improved experimental results. Last, but not least the analysis of these experiments compares the achieved STR to the theoretical optimum as well as to an idealized camera-based tracking experiment.

We carried out basic tracking experiments of surface-immobilized Atto647N fluorophores that were translocated by the piezo-electric sample stage to verify the performance of our MINFLUX tracking approach. Afterwards, we followed the dynamics of DNA origami nanorobots, visualizing the nanorobots taking discrete steps along predefined positions on a DNA track. Finally, we mapped the stepping behavior of Kinesin-1, a motor protein taking discrete steps along microtubules to transport intracellular cargo [40]. We recorded Kinesin-1 dynamics with unprecedented STR under physiological conditions.

4.1 Fluorescence Tracking Enables Important Life Science Studies

Cells are the building blocks of life, but already by themselves highly complex and organized machineries with innumerable amounts of dynamic molecular processes. Their structures are in constant change in respect to location, conformation and kinetics. Ensemble measurements of these dynamics like Fluorescence Return After Photo-bleaching (FRAP) or Fluorescence Correlation Spectroscopy (FCS) as well as cell-lysate based studies can hide functional heterogeneities of molecule species and protein complexes [41–43]. Seeing is believing – Single Molecule Tracking (SMT) enables the direct observation and investigation of functional dynamics of molecular machineries and networks on a molecular scale and delivers important information about the inner workings of life.

The higher the available STR, the more information can be gained with greater precision. Therefore, the advances in the field of super-resolution tracking have always led to novel biological insights. Using live-cell fluorescence tracking, Irvine et al uncovered that the sensitivity of certain T cells is high enough to respond with a transient calcium signal when exposed to a single agonist ligand [44]. Reyes-Lamothe et al investigated the stoichiometry and architecture of the active DNA replication machinery in *Escherichia coli* with high resolution single molecule tracking. The study uncovered the replisome's true composition with three replicative polymerases and refuted the historically accepted view that counted only two active molecules [45]. Motor proteins like Kinesin play a central role in intracellular transport and are therefore another important field of medical and biological research. Malfunction of this processes can lead to serious consequences like motor neuron disease by disruption of fast axonal transport, hereditary spastic paraplegia (SPG10) or Amyotrophic Lateral Sclerosis (ALS) [46–48].

4.2 State of the Art

The aforementioned advantages of SMT boosted a number of technological developments in recent years.

The concept of feedback tracking comprises a number of techniques that establish the trajectory of a single particle by repeatedly localizing the emitter and subsequently moving either sample stage or the probe to center the molecule. The stage or beam positions over time yield the information about the tracked path. In tetrahedral confocal based 3D tracking, the single emitter's coordinates are calculated from the signal of four individual

detectors with detection volumes tetrahedrally arranged in sample space. They detect fluorescence signal from two different positions in two different imaging planes with equal spacing of roughly 50 µm. A piezo stage repositions the sample such that the emitter always stays in the center of the combined detection volume [49]. The time resolution of this approach is about 5 ms with a spatial resolution of roughly 50 nm in x/y and 80 nm in z direction.

An adapted version of this approach was coined 'Tracking Single Particles using Nonlinear and Multiplexed Illumination' (TSUNAMI). To create four excitation beams pointing in a tetrahedral pattern around the emitter's position a pulsed laser beam from a Ti:Sa infared laser is split up into four beams with delays of up to 9 ns. The detected photons are then assigned to the individual excitation PSFs by their time of arrival and the piezo stage is repositioned according to the derived emitter location. Because it utilizes two photon excitation, this technique is able to localize emitters at large penetration depths. The attained lateral and axial resolution reaches 22 nm and 90 nm, respectively, with a time resolution of down to 50 µs depending on the fluorescence rate [50, 51].

In orbital scanning, a confocal excitation beam is scanned in a 3D orbit around the emitter's position. The feedback system is based on an algorithm that uses a Fast Fourier Transformation (FFT) evaluating the temporal sequence of the fluorescence counts and thus the emitter's coordinates to control the scanner position. The precision reached with this approach is about 6 nm in lateral and 34 nm in axial direction at a time resolution in the millisecond range [52, 53].

Sahl et al presented a confocal tracking approach without feedback, which collects the fluorescence signal with three densely packed optical fibers connected to APDs [54]. The spot of maximum detection efficiency is slightly shifted laterally for each fiber. From the different signal amplitudes in the three detection channels, the position of the emitter is calculated relative to the excitation spot. The method offers a spatial resolution of $<$30 nm and temporal resolution of $<$1 ms.

Instead of tracking the emitter's position by repositioning the sample stage or the excitation beam, alternative methods confine the emitter in an optical or electrophoretic trap.

The 'Anti-Brownian Electrophoretic Trap' (ABEL) is a microfluidic system that actively cancels the positional drift of an emitter or particle in solution by applying voltages on different electrodes. The generated electrophoretic forces trap the particle and a CCD camera records its position. Based on the feedback voltages, the emitter's pseudo-free trajectory can be reconstructed [55].

Optical Tweezers are a powerful tool to carry out SMT or single particle tracking experiments. The (macro)molecule of interest is attached to a nanosphere made from gold, polystyrene or germanium. This nanosphere is then trapped in the focus of a high-powered laser beam. By measuring the displacement of the nanosphere from the center of the focal spot, for example by imaging it with a CCD camera, the acting forces can be infered. Due to the strong scattering cross section of the relatively large beads and the resulting high photon counts, the method reaches exceptionally high STRs. Because the restoring forces that are trapping the nanosphere can be in the same order of magnitude as the forces generated by the movement of the (macro)molecule itself, Optical Tweezers may disturb the (macro)molecule's native behavior [56].

The majority of SMT methods are camera-based. In contrast to trapping methods these approaches do not require the presence of nanospheres, but instead only labeling single molecule emitter (e.g. organic dyes or fluorescent proteins) and thus do interfere significantly less with the natural dynamics. PALM and STORM measurements routinely reach a spatial resolution of 20-50 nm at a time resolution of some tens of milliseconds. To increase the localization precision, it is necessary to collect more photons by either increasing the excitation power at the cost of faster photobleaching or by extending the exposure time at the cost of the sampling frequency. With 'Fluorescence Imaging with One Nanometer Accuracy' (FIONA) Yildiz et al optimized the camera-based localization approaches with respect to technical background and photostability of the utilized dyes, reaching a single molecule localization precision below 10 nm at exposure times of 0.2 – 0.5 seconds [18].

One advantage of camera-based methods is their high parallelization. Depending on the optical setup, FOVs of 50x50 µm can be imaged at a time, allowing for tracking of a large number of particles in parallel. However, due to the limited photon-efficiency of the centroid localization, the STR is limited and thus many protein and (macro)molecular dynamics cannot be resolved.

Dark field microscopy also relies on a camera to localize single particles with a high scattering efficiency. To increase the SBR, the beam path contains an optical device that allows scattered but not reflected light to reach the camera. Applying high laser powers in the range of up to 10 mW, a remarkable STR can be achieved as the high scattering photon counts are detected. Isojima et al report a spatial precision of 1.3 nm at 55 µs temporal resolution with 40 nm gold nano particles [57]. One of the drawbacks is the high power, which can be detrimental to the study of living samples. Furthermore, the technique requires relatively large scattering probes, which are ten to hundred times larger than the actual molecule of interest. The native processes and dynamics can potentially be altered by steric hindrance and increased hydrodynamic drag such that the study of

the complex of interest under physiological conditions is inhibited. Therefore, methods that are able to employ fluorescent single molecules for labeling are preferable.

4.3 MINFLUX Enables Tracking Studies Under Physiological Conditions

Many open questions in biological and medical research can only be answered if real-time tracking of single molecules or small (macro)molecular complexes becomes feasible under physiological conditions at a single-digit nanometer resolution.

Most single molecule fluorophores yield a maximum fluorescence photon rate of some ten to some hundred kilohertz over an extended period of time. In general, the more photons are collected from a single emitter, the more precisely it can be localized. Thus, to increase the precision, the integration time must be increased at the cost of a decreased temporal resolution. Due to these photophysical properties, the trade off between spatial and temporal resolution is inherent.

The product

$$STR = \delta\sqrt{\tau} \tag{4.1}$$

quantifies the spatio-temporal resolution (STR) of a technique at a certain fluorescence count rate. It describes the smallest detetable step size δ and/or the shortest time interval than can be resolved τ [58]. This measure clearly showcases the increased localization efficiency of MINFLUX.

We define the detection threshold for a step with size δ for a single measurement as

$$\delta = 3 \cdot \sigma \tag{4.2}$$

with σ being the standard deviation of the position trace. Assuming a normal distribution, a single position measurement deviating δ from the mean value by this size has a probability of <0.3% to be an outlier of the original distribution. Thus, the probability that the actual position of the emitter has changed is >99.7% [59]. In practice, many processes will create sustained changes of the emitter position. By averaging the position information over multiple dwell times and decreasing temporal resolution, position changes much smaller than δ can be resolved.

Assuming a constant fluorescence rate the improvement in STR of MINFLUX over camera-based single molecule localizations can be calculated. We reconsider equation 1.5. As

described in Section 1.2, the precision σ with which the lateral position of an emitter that is detected on a camera under ideal circumstances, can be calculated by the formula

$$\sigma_{cam} = \frac{\sigma_{PSF}}{\sqrt{N}} \tag{4.3}$$

with σ_{PSF} being the standard deviation of the Gaussian approximation of the diffraction spot σ_{PSF} and N the number of collected photons. For an excitation wavelength of 640 nm σ_{PSF} will be $\sim$ 120 nm [9]. If we assume an integration time of 300 µs and a detected fluorescence rate of 100 kHz the number of collected photons N will be 30. This leads to an theoretical STR of

$$\delta\sqrt{\tau} = 3 \cdot \frac{120\,\text{nm}}{\sqrt{30}} \cdot \sqrt{300\,\mu\text{s}} = 1.14 \cdot 10^{-9} m\sqrt{s}. \tag{4.4}$$

As described in Section 1.3, the precision of a MINFLUX localization in 1D is described by

$$\sigma_{MF} = \frac{L}{4\sqrt{N}} \tag{4.5}$$

with L typically ranging from 15 and to 100 nm. For tracking experiment during which the emitter is confined to an area smaller than the diffraction limit an $L = 30$ nm is appropriate. If again assuming an integration time of 300 µs at at detected fluorescence rate of 100 kHz and thus 30 collected photons (15 per 1D localization), the STR is

$$\delta\sqrt{\tau} = 3 \cdot \frac{30\,\text{nm}}{3\sqrt{15}} \cdot \sqrt{300\,\mu\text{s}} = 1.01 \cdot 10^{-10} m\sqrt{s}. \tag{4.6}$$

Remarkably, applying the MINFLUX concept improves the STR more than one order of magnitude in comparison to the camera-based localization scheme.

The increased photon efficiency that MINFLUX offers allows for the use of conventional fluorophores for ultra-fast localization and tracking with molecular resolution. Staining constructs like large nanospheres or chains of antibodies that are required by camera-based approaches for providing numerous photons, are not necessary as bright, fluorescent molecules deliver sufficient photons for MINFLUX. In contrast to methods like dark field microscopy or optical traps, disturbing the biological system of interest is thus considerable less likely.

Until now three studies employing MINFLUX for tracking of fluorescent single molecules were published. In the publication introducing MINFLUX, single 30s ribosomal protein subunits that were fused to the switchable protein mEos2 were tracked in E. coli bacteria. At a sampling frequency of 8 kHz, corresponding to a measurement time of 125 µs an average tracking error of 48 nm was reported [14]. The resulting STR is $1.61 \cdot 10^{-9} m\sqrt{s}$. The average detected photon rate in this experiment was about 70 kHz. As proof-of-

principle for the feasibility of carrying out MINFLUX microscopy and tracking with a standard microscope body, Schmidt et al studied the movement of fluorescent lipid analogs in a defect free support lipid bilayer on coverglass. The lipid analogs were marked with Atto647N single molecules and the detected photon rate was about 200 kHz. In this experiment, a localization precision of $\sim$ 20 nm was reached at a mean sampling time of 125 µs [17]. The resulting spatio temporal resolution amounts to $6.49 \cdot 10^{-10} m\sqrt{s}$. In the MINFLUX tracking experiment conducted by Eilers et al on Atto647N a localization precision of 2.4 nm was reached at a sampling time of 400 µs, resulting in a STR of $1.44 \cdot 10^{-10} m\sqrt{s}$. This high STR could be reached due to the large average photon rate of $\sim$ 350 kHz [25].

4.4 Theoretical Superiority Translates into Experimental Results

To showcase the STR of our MINFLUX microscope we carried out three proof-of-principle experiments. First, we evaluated the tracking capability of our setup for fluorophores in a highly controlled environment, by tracking single molecules while moving the sample stage in a preprogrammed pattern. Next, we performed tracking experiments with DNA origami nanorobots that can step along predefined track positions. Last, we applied the MINFLUX tracking approach to investigate the stepping behavior of Kinesin-1.

4.4.1 Stage Tracking Experiments

To evaluate the tracking capability of our setup, we continuously localized single molecules residing in a highly controlled environment while moving the sample stage in a preprogrammed pattern. Atto647N molecules were immobilized on a cover slip surface with a PLL-PEG-STV-BT/Atto647N construct according to the protocol in Section 2.5.2.

To initially find the emitter positions, we performed confocal scans with a FOV of 10x10 µm and extracted the emitter positions with the LabView VI *find positions.vi* which is described in Section 3.1.1. The galvanometer was then pointed to the first emitter position and the preprogrammed stage movement was started. The stage was moved with high precision in various different patterns in x and y direction. The molecule was repeatedly localized with an iterative MINFLUX sequence until photo-bleaching occurred (for details see procedure described in Section 3.1.1). Subsequently, the next molecule position was targeted and the MINFLUX sequence repeated. Position data were evaluated with

the fixed curvature estimator (see Section 2.3.2).

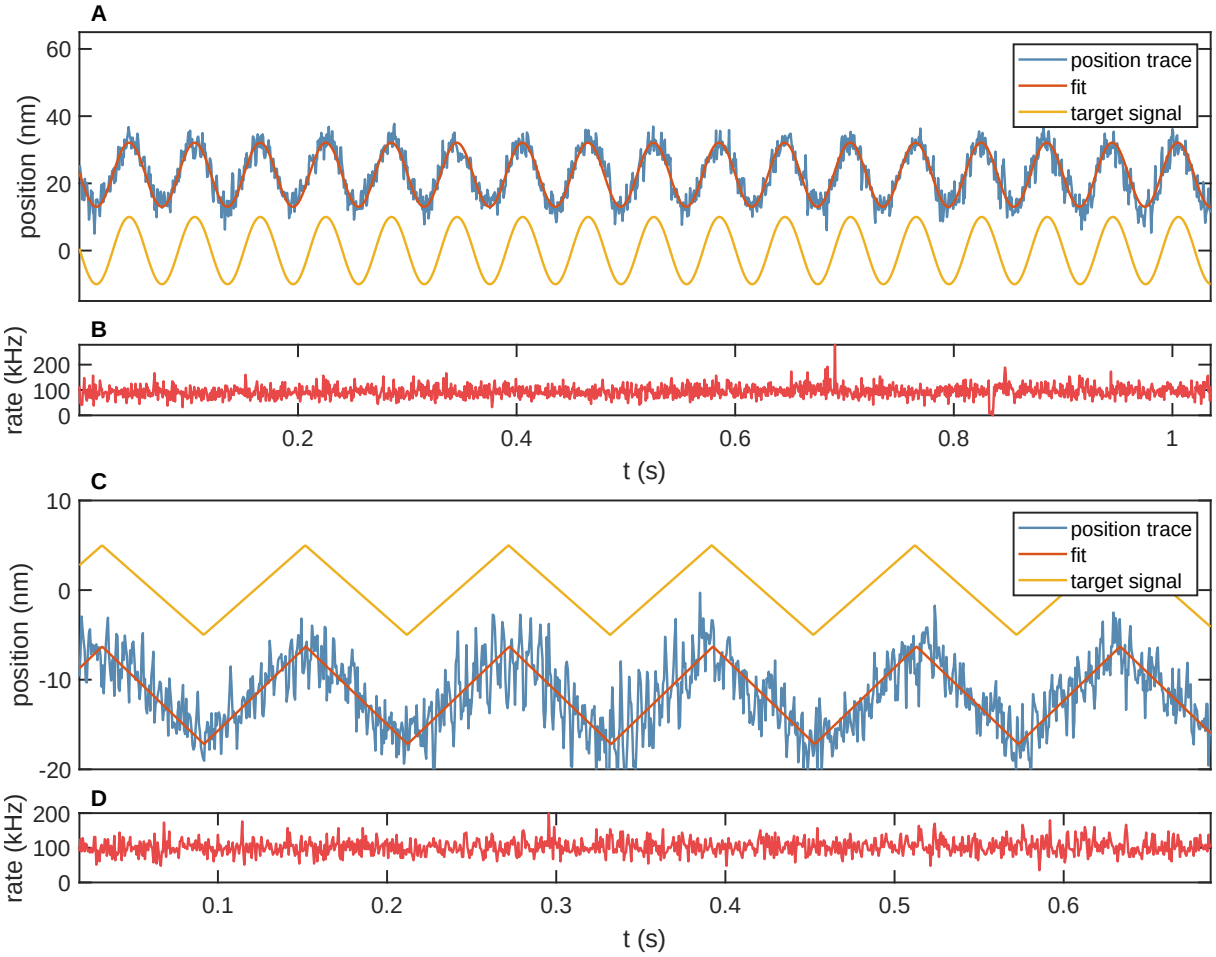

Figure 4.1: Tracking of sinusoidal and triangular stage translocation Tracking of Atto647N single molecules verifies the fidelity of the position traces generated by our MINFLUX setup. In **A** and **C** the blue data points represent the MINFLUX position trace that was recorded. For comparison a sinusoidal and triangular curve was fitted to the data and is shown (red curves). The programmed stage translocation signal is displayed by the yellow curve. For both traces, target signal and MINFLUX trace show a high agreement. The detected photon rates are depicted in **B** and **D**. The mean localization precision of the position traces was 2.70 nm ($\overline{N}$ = 29.2, 1D) for the sinusoidal movement and 2.43 nm ($\overline{N}$ = 32.0, 1D) for the triangular movement. For the discussion of the STR refer to Table 4.1.

The results of two of these experiment are visible in Figure 4.1. In Figure 4.1 **A** a measurement of a sinusoidal target signal is shown. To assess the localization efficiency, we calculated the STR of the movement-free traces according to equation 4.1. To obtain this corrected trace, we fitted the recorded position trace with a corresponding function and subtracted this fit from the trace. Frequency and amplitude of the position trace follow the target signal very well. For the sinusoidal movement the localization precision was 2.70 nm and the SBR at L=30 nm was 2.99. The traces were recorded with a sampling time per 2D localization of 625 µs. The STR was $2.02 \cdot 10^{-10}\ m\sqrt{s}$. All results are summarized in Table 4.1. Figure 4.1 **C** depicts a position trace following a triangular target signal, which is again reproduced very well. The detected fluorescence rate is shown in Figure 4.1 **D**

and was about 100 kHz. The localization precision in x-direction was 2.43 nm. The SBR at L=30 nm was 5.8. At a sampling time of 625 µs this resulted in a STR of $1.83 \cdot 10^{-10}$ $m\sqrt{s}$.

Table 4.1: Overview of tracking precision and STR for stage tracking experiments All photon counts are stated per dimension. The corresponding traces are depicted in Figures 4.1 and 4.2. In the last MINFLUX step $L = 30$ nm was used. The deviation from the theoretical optimum varied between 31.5% and 51.2%. Possible reasons were discussed in detail in Section 3.3. The STRs for all three shown traces were between 5.8 and 6.4 times better than the best STR that would be achievable with camera-based tracking methods.

Measurement	$\overline{\sigma}$ (nm)	Sampling Time (μs)	$\overline{SBR}$	STR MINFLUX ($m\sqrt{s}$)	Theoretical Optimum STR_{MF} ($m\sqrt{s}$)	Expected idealized STR_{cam} ($m\sqrt{s}$)
Sinusoidal movement Fig. 4.1 A/B	2.70 @$\overline{N} = 29.2$ (1D)	625	2.99	$2.02 \cdot 10^{-10}$	$1.47 \cdot 10^{-10}$	$1.18 \cdot 10^{-9}$ @N=58.4 (2D)
Rectangular movement Fig. 4.1 C/D	2.43 @$\overline{N} = 32.0$ (1D)	625	5.80	$1.83 \cdot 10^{-10}$	$1.21 \cdot 10^{-10}$	$1.13 \cdot 10^{-9}$ @N=64.0 (2D)
Circular movement Fig. 4.2	2.67±0.22 @$\overline{N} = 24.9$ (1D)	625	3.52	$2.00 \cdot 10^{-10}$ $\pm 1.67 \cdot 10^{-11}$	$1.52 \cdot 10^{-10}$	$1.28 \cdot 10^{-9}$ @N=59.8 (2D)

For the experiment shown in Figure 4.2, we programmed the stage to move in a circular 2D pattern with a radius of 10 nm. As expected, a phase shift between the sinusoidal patterns in x and y direction was observed (Figure 4.2**A**). Plotting the corresponding 2D localizations clearly resolves the circular movement with the preset radius (Figure 4.2 **B**). The mean SBR of x and y localizations at L=30 nm was 3.52. The collected photon rate is shown in Figure 4.2 **C**. On average 24.9 photons were collected per dimension. Figure 4.2 **D** shows the fluorophore's track color coded according to time of localization. To depict the temporal progression of the fluorophore's position, consecutive localizations are connected by a gray line. The position trace shown was cut after a single revolution of the stage movement to increase plot clarity.

In all experiments the stage movement was reproduced with large localization accuracy and precision. To assess the potential for further improvement of the measurement results, we calculated the theoretical optimum of the STR. For comparison, the achievable localization precision and the corresponding STR for a camera-based tracking was calculated. Here, we assumed ideal conditions, meaning a background-free sample and a camera with

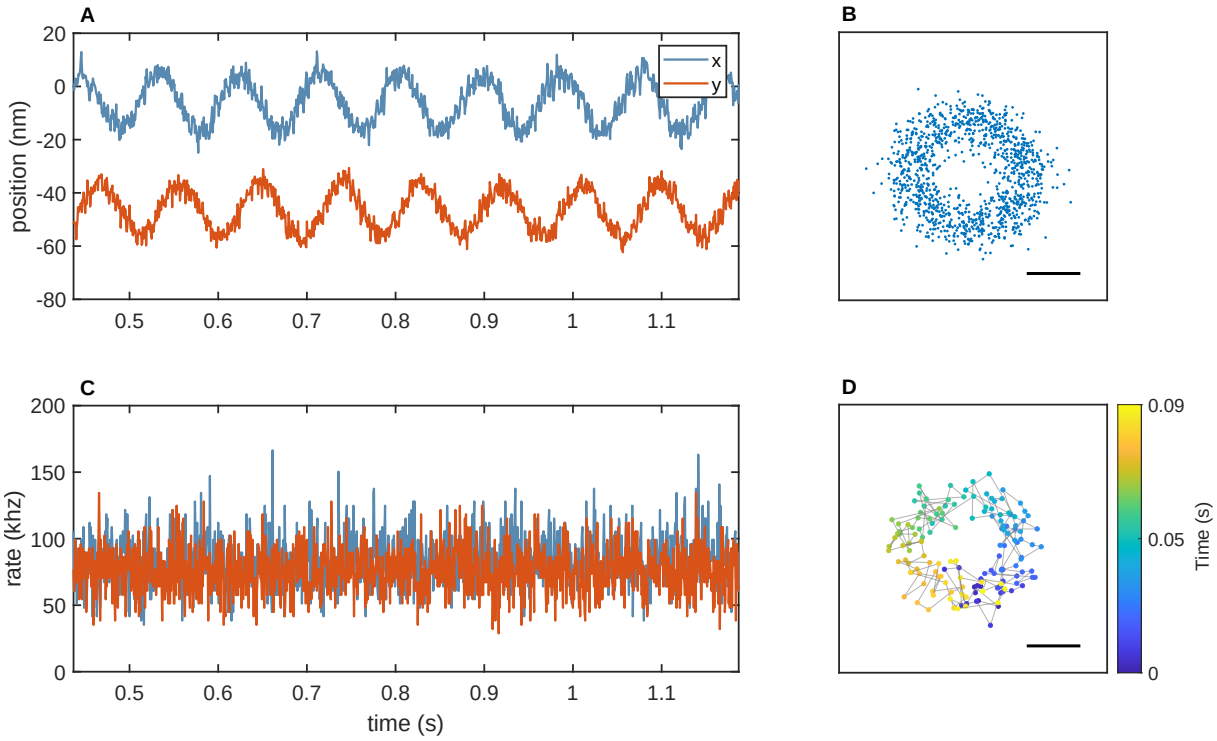

Figure 4.2: Tracking of circular stage translocation The radius of the stage movement was set to 10 nm. The position traces for x and y direction are shown in **A**. The photon rate for the two dimensions was $\sim$ 80 kHz. The set phase shift to generate a circular pattern is clearly visible. A scatter plot of the localizations in 2D showing the circular arrangement of the positions is depicted in **B**. To show the temporal sequence of the localizations the colors of the data points in the 2D view in **D** are coded according to the colorbar representing the time of localization. Consecutive localizations are connected with a gray line. For clarity the trace was shortened to a single revolution of the circular movement. Scale bars, 10 nm

SBR=∞. All results are given in Table 4.1.

For tracking of the sinusoidal target signal, the STR was about 37% below the theoretical optimum. In comparison to the experimental localization performance of MINFLUX, a camera under ideal conditions would deliver a STR that is ab 5.8 times worse. A similar trend holds true for experiments tracking the triangular and the circular target signal. Here, the experimental localization performance deviates by 51.2 and 31.2% from the theoretical poisson noise limited optimum. In comparison to the camera-based localization the experimental performance is about 6.2 and 6.4 times better.

The comparison to camera-based localization methods highlights the superior localization efficiency of MINFLUX. Due to the limited update time, acceleration and velocity of the piezo electric stage, we were not able to reliably produce faster stage movements. However, the data quality of the presented measurements suggests that our MINFLUX microscope is capable of tracking even faster movements.

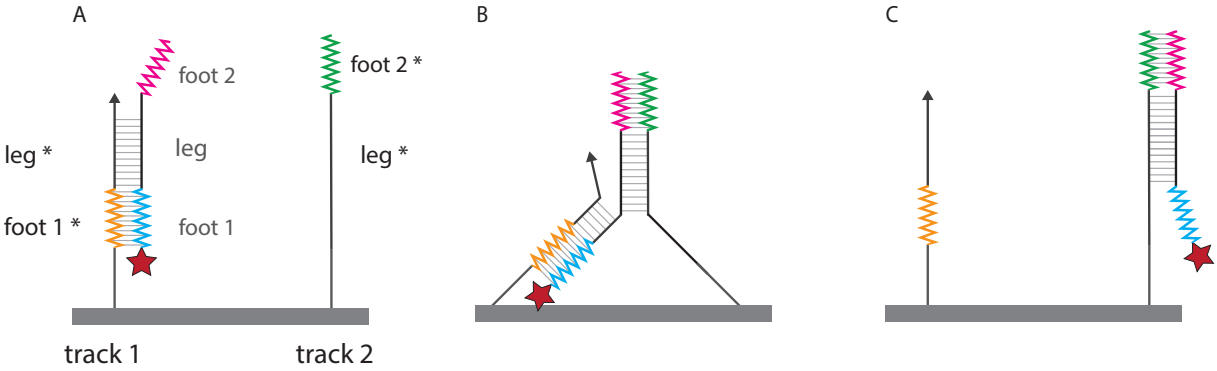

Figure 4.3: Sketch of the nanorobot walkin mechanism The nanorobot takes step automatically through the complementary ssDNA sequences of the track and the robot itself. **A** The nanorobot is attached to track 1 by the complementary DNA strands leg/leg* and foot/foot1* with foot 2 hanging free. **B** Due to the residual mobility of foot 2, the nanorobot can move to the proximity of track 2 where the complementary DNA strand foot 2* and leg* are located and attaches there. **C** By detaching completely from track 1 the nanorobot can complete its step and is fully bound to track 2. This again leaves foot 1 free to attach to close by track 1 DNA strands and so forth.

4.4.2 DNA Origami Nanorobots

In a next step, we searched for a biotechnological test system offering some prior knowledge about the system's behavior to further substantiate the performance of our setup in more complex SMT experiments. The aim was to show that unknown movement patterns can be tracked while still having the chance to verify whether the resulting traces are in reasonable agreement with the expected behavior. To do so, we decided to track DNA nanorobots designed together with Prof. Dr. Lulu Qian[1], Prof. Dr. Erik Winfree[1] and Namita Sarraf[1]. The system is inspired by a publication of Thubagere et al [60]. The strands were ordered with Integrated DNA Technologies and folded in-house by Dr. Jessica Matthias[2]. The samples were prepared according to the protocol in Section 2.5.4.

The nanorobots as well as the individual track positions (track 1 and track 2) consist of single-stranded DNA (ssDNA). Track 1 and track 2 are fixed to a DNA baseplate and spaced by 6 nm, while the nanorobot randomly 'walks' along the track positions without requiring additional power. The walking mechanism is based on complementary stretches of ssDNA between nanorobot and the track positions. The nanorobot consists of three distinct sequences, namely leg, foot 1 and foot 2. While both track positions share the complementary sequence to the nanorobot's leg domain (leg*), track 1 and track 2 each additionally comprise the complementary sequence to the nanorobot's foot 1 or foot 2 domain (foot 1* oder foot 2*), respectively. The walking mechanism is schematically depicted in Figure 4.3. Through complementary base pairing, the nanorobot transiently

[1]California Institute of Technology, Pasadena, USA
[2]Department for Optical Nanoscopy, Max-Planck-Institute for Medical Research, Heidelberg, Germany

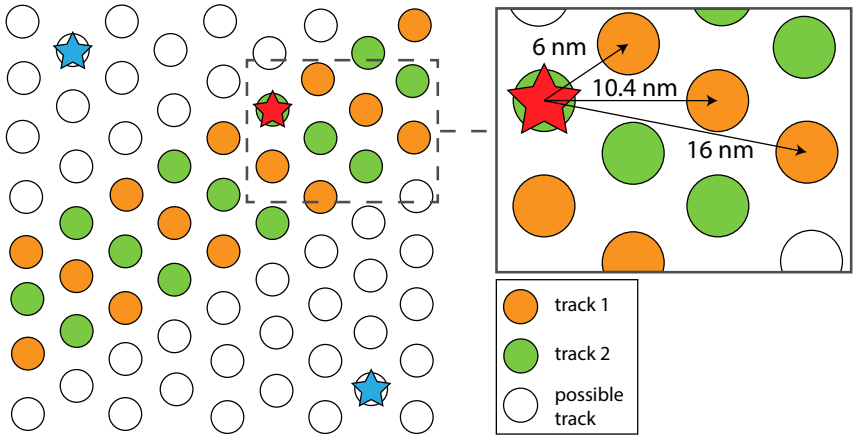

Figure 4.4: Sketch of the nanorobot walking track The different DNA strands are connected to a DNA origami sheet that is immobilized on the cover glass surface. The two species of track positions (orange and green) are arranged in interleaved rows of three. Through the mechanism described in Figure 4.3 the nanorobots can step between binding sites of the two species. Alexa 488 fluorophores are depicted by blue stars. Figure not to scale.

binds to track 1(track 2) leaving the foot 2(foot 1) unoccupied. As the system is not entirely rigid, the nanorobot/track1(track 2) complex and track 2(track 1) can reach close enough proximity for the nanorobot to partially attach to track 2(track 1) via foot 2(foot 1), giving rise to a hybrid intermediate construct in which the nanorobot is temporarily bound to both track positions. The nanorobot completes its step by entirely detaching from track 1(track 2) and fully attaching to track 2(track 1), leaving foot 1(foot 2) unbound to initiate the next step. Thus, the DNA origami design allows the nanorobots to only take steps from track 1 to track 2 and vice versa but not between track positions of the same kind.

To track the steps, an Atto647N single molecule was attached either at foot1 (nanorobot 3F) or at foot2 (nanorobot 5f). The baseplate was additionally marked at two corners with Alexa488 single molecules and immobilized via biotin/neutravidin interaction. The track positions were arranged in a hexagonal pattern on the baseplate forming a three positions-wide diagonal with track 1 and track 2 alternating (Figure 4.4). Due to the geometry and stepping restrictions (no stepping between track positions of the same kind) we expected step sizes of 6 nm (nearest-neighbor distance), 10.4 nm and $\sim$ 16 nm.

MINFLUX Tracking of Nanorobots

During the sample preparation the density of detected Alexa Fluor 488 markers was checked to ensure sufficient separation between the nanorobot tracks. The nanorobots were then added to the sample medium in very low concentration, such that on average less than a single nanorobot was bound per baseplate. To identify suited nanorobot positions,

we performed a 10x10 µm confocal scan with an excitation wavelength of 640 nm at low powers and extracted emitter positions with the *find positions.vi* described in Section 2.4.1. The galvanometer scanner was pointed at a found emitter location and an iterative MINFLUX tracking procedure was started. In the last MINFLUX step $L = 40\,\text{nm}$ was used.

Results

A representative example trace can be seen in Figure 4.5. The x and y position traces and the corresponding recorded fluorescence count rate are depicted in Figure 4.5 **A** and **B**. In Figure 4.5 **C** the temporal sequence of the nanorobot movement is depicted in a scatter plot with the time of the localization color coded. The opaque grey lines indicate the sequence of localizations. The pattern of the track positions becomes apparent in which the nanorobot resided over extended periods of time. The strong imbalance between the number of localizations per resting position arises from the stochastic nature of the stepping behavior.

For the scatter plot in Figure 4.5 **D** we have applied a *dbscan* clustering algorithm to infer the center of mass of the different clusters, allowing us to calculate the cluster-to-cluster distances as displayed in 4.6 [33, 61]. The observed stepping distances agree well with the theoretically predicted spacing of track positions described in the previous section. Small deviations can be explained by sample drift during the measurement time, imperfections of the DNA baseplate and a certain system flexibility. As we only gain 2D information, we cannot exclude the track to be distorted on the cover slide surface, such that geometrical relations are slightly altered.

Additional traces can be seen in Figure 4.7 and in the Appendix. We have evaluated the localization precision of these 20 traces (shown here and in the Appendix) further and compared it to the theoretically achievable precision of MINFLUX and the camera-based localization approach. The results are summarized in Table 4.2.

Calculating the movement-free localization precision as described in Section 4.4.1, we reached a mean precision of 2.18±0.37 nm when collecting on average 58.6 photons per dimension. With a mean sampling time of 3.1 ms, the resulting STR was $3.64 \cdot 10^{-10} \pm 7.37 \cdot 10^{-11}\ m\sqrt{s}$. The theoretical boundary for the MINFLUX localization precision at the measured SBR of 6.9 lies at 1.61 nm, implying an hypothetical STR of $8.96 \cdot 10^{-11}\ m\sqrt{s}$. Possible reasons for the decreased precision of the experimental data in comparison to the theory are sample drift, vibrations that coupled from outside into the setup as well as a certain flexibility between DNA baseplate and the track positions that is inherent by

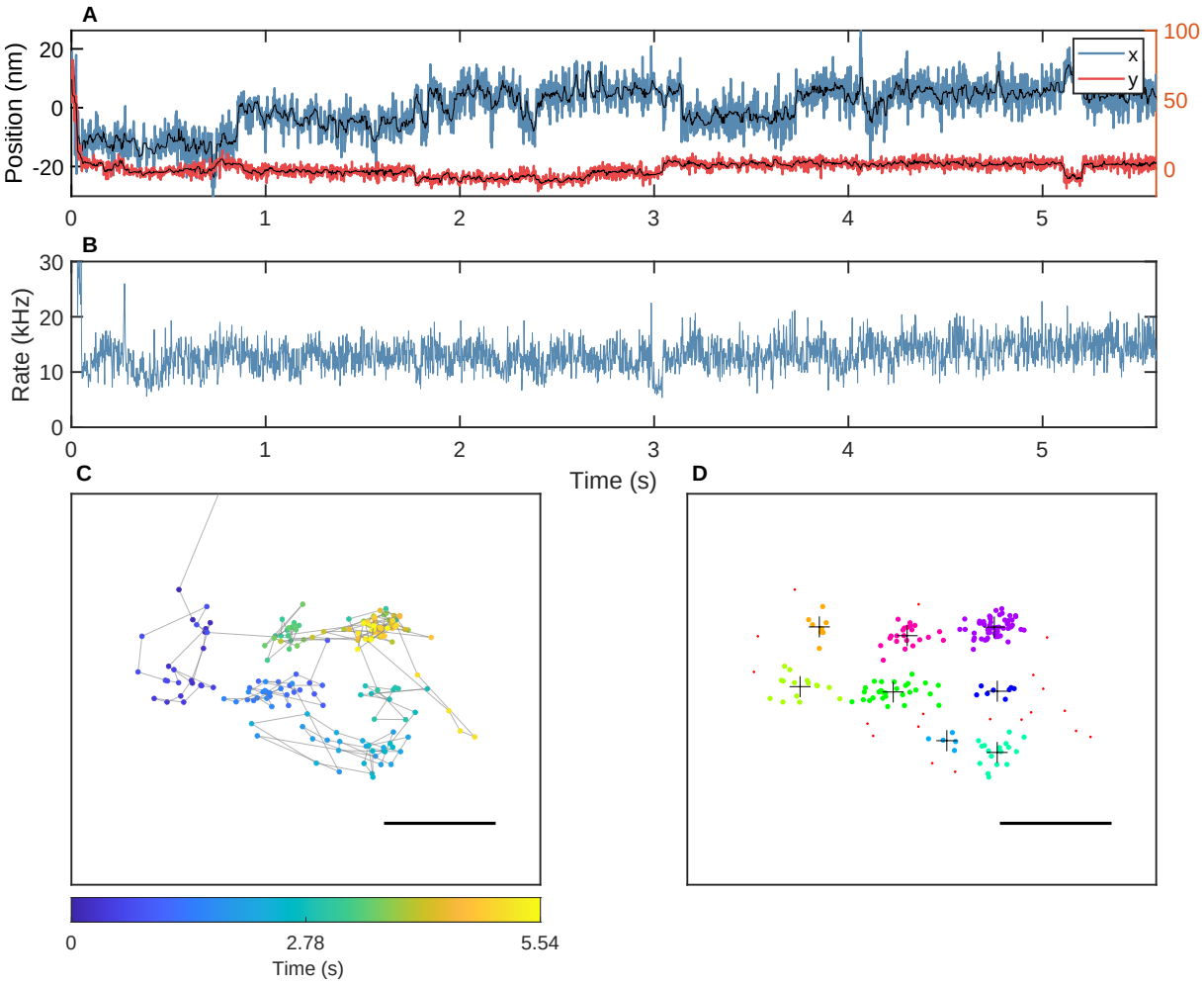

Figure 4.5: Representative 3f nanorobot stepping trace A The x and y position traces are depicted in blue and red. Additionally a median filter of rank 10 was applied to the traces and is shown by the black curve. The corresponding detected photon rate is shown in **B**. In **C** the time of localization is depicted by the color of the data points according to the colorbar on the right-hand side to reveal the path taken by the nanorobot. Consecutive localizations are connected by a gray line as visual guidance. A scatter plot of the filtered and binned localizations is shown in **D**. A *dbscan* clustering algorithm was applied and the belonging to the individual clusters is shown by the color of the data points. The centers-of-mass of the individual clusters are shown by the cross. Scale bars, 10 nm.

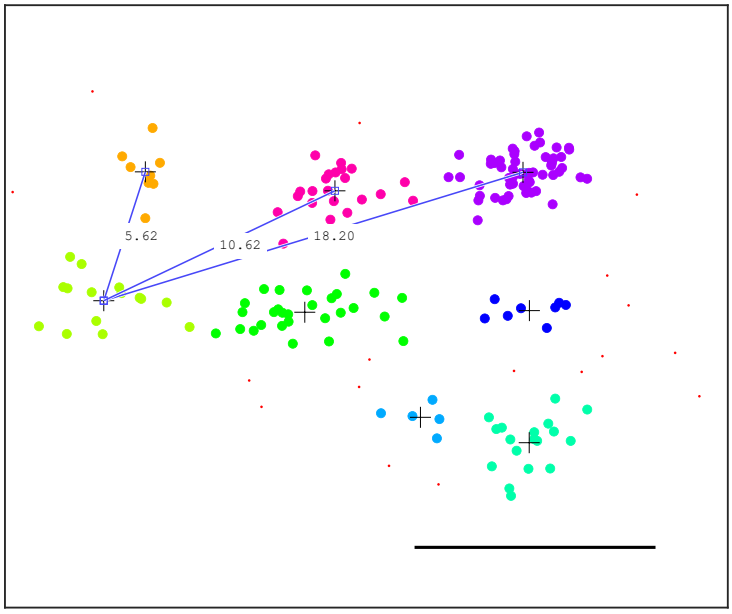

Figure 4.6: Distances between clustered localization points of nanorobot stepping All given distances in nanometer. The localizations were clustered using a dbscan clustering algorithm with the Matlab function *dbscan*. The formed clusters can be recognized by the data point's color. The distances between cluster show a reasonable agreement with the expected separations of 6 nm, 10.4 nm and ∼16 nm. Scale bar, 10 nm

Table 4.2: Localization precision and STR for nanorobot traces The mean localization precision and STR of the movement free traces is displayed for the experimental results of the nanorobot traces and compared to the theoretical optimum that is achievable with MINFLUX at the measured photon count and SBR as well as to the performance of an idealized camera-based localization. The average detected photon rate was 24.9 ± 5.8 kHz.

	MINFLUX Experimental Results	MINFLUX Theoretical Optimum	Expected Idealized Camera-based Localization
$\overline{\sigma}$ (nm)	2.18 ± 0.37 @N=54.8 (1D) @SBR=6.9	1.61 @N=54.8 (1D) @SBR=6.9	14.3 @N=109.6 (2D) @SBR=∞
$\overline{STR}$ ($m\sqrt{s}$)	$3.64 \cdot 10^{-10} \pm 7.36 \cdot 10^{-11}$	$8.96 \cdot 10^{-11}$	$2.39 \cdot 10^{-9}$

design and necessary for the nanorobot to move from one track position to the other. For an elaborate discussion of detrimental influences refer to Section 3.3.

To compare the improvement MINFLUX offers, we calculated the localization precision that can be theoretically reached with a camera-based method. At the measured photon count and in a background-free sample using a perfect camera with a readout-noise of zero, the ideal localization precision is 14.3 nm. The corresponding STR is $2.39 \cdot 10^{-9}$ $m\sqrt{s}$ or about 6.6 times worse than the experimental data acquired with MINFLUX. The comparison emphasizes that even under experimental conditions, MINFLUX outperforms

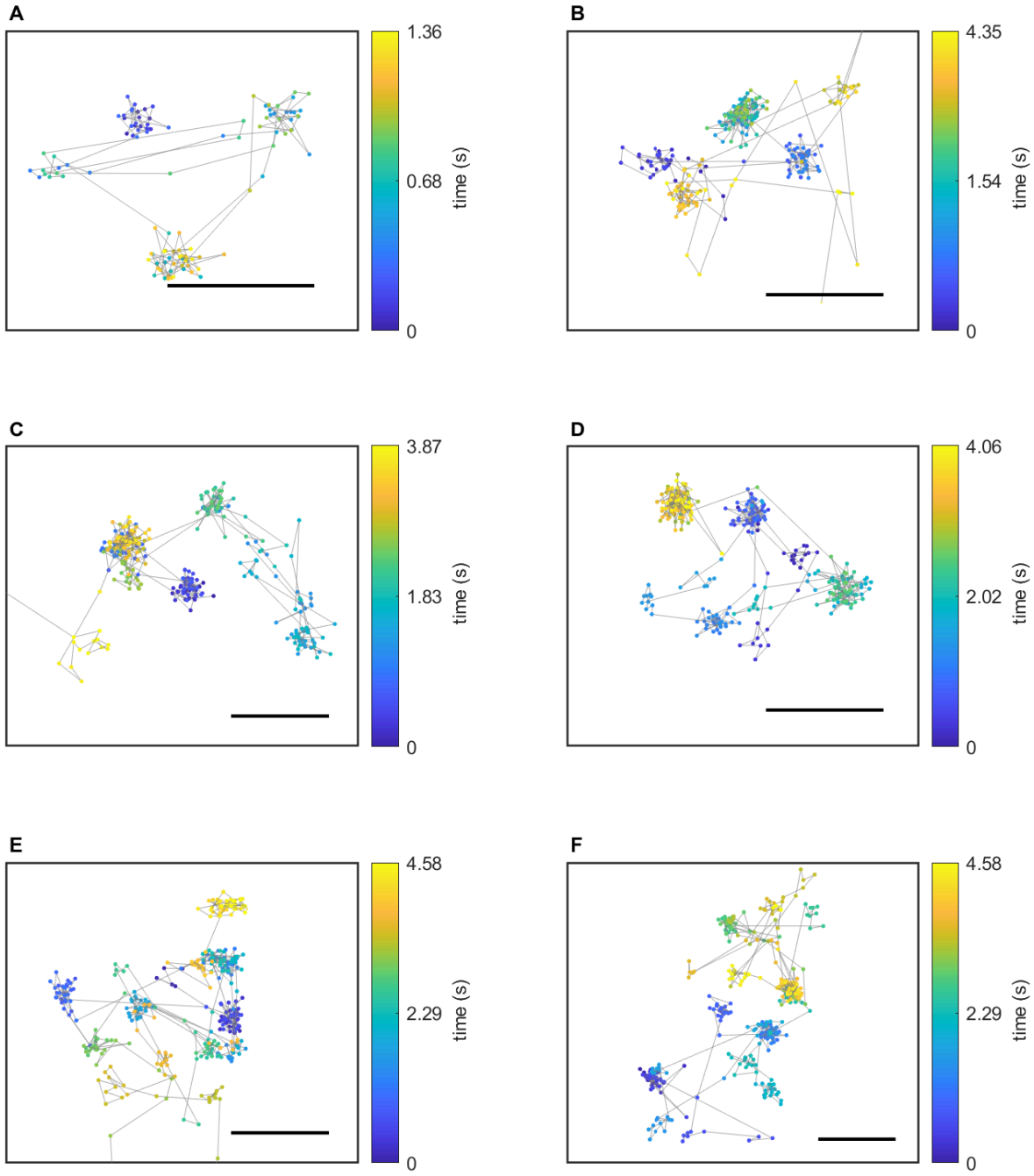

Figure 4.7: Additional nanorobot traces Only 5F nanorobots are depicted. All Figures show the distinct stepping behavior that is expected from the nanorobot mechanism. The arrangement of the different cluster points is strongly heterogenous due to the stochastic nature of the mechanism. Additional traces can be found in the Appendix. Scale bars, 10 nm

an idealized camera-based measurement. Environmental (vibrations, thermal drift) and sample internal (sample background, system flexibility) influences, that deteriorated the accuracy and precision of the MINFLUX localization certainly also affect camera-based localizations. Thus, in a comparison with the experimental performance of the camera-based localization approach, MINFLUX would even more evidently outperform.

4.4.3 MINFLUX Improves Spatio-Temporal Resolution of Kinesin Tracking

In the previous sections the theoretical and experimental advantages that MINFLUX tracking offers in comparison to established camera- or trap-based tracking methods were established. In this chapter we will present the application of MINFLUX tracking to a dynamic biological and complex macromolecular system. We investigated the movement of the Kinesin-1 motor protein (in the following referred to as kinesin) along microtubules under physiological conditions *in vitro*. We successfully demonstrated with this that the high localization efficiency of our MINFLUX microscope allowed us to observe details of the kinesin stepping behavior that were until now not accessible under physiological conditions.

Due to the size of and distances between intracellular compartments, many transport processes require a directed and driven transport along cytoskeletal filament systems. Kinesin-1 is responsible for the transport of cargo along microtubules [40]. It consists of a stalk domain connected to two head domains that bind individually to single tubulin monomors of a microtubule. According to the current state of knowledge, the two heads take alternating steps of 16.3 nm in a hand-over-hand mechanism [62, 63]. Cargo is bound to the stalk domain and dragged along microtubules by the heads taking alternating steps. During this transport process, ATP is hydrolyzed to fuel the movement. The ATP concentration in the medium surrounding kinesin and microtubules determines the stepping frequency [64]. Kinesin applies forces in the piconewton range and carries cargo like vesicles and organelles [65].

The stepping behavior of kinesin has already been intensively studied with various microscopy methods. As previously mentioned, optical trap measurements provide a high STR. They led to important insights into the mechanism of kinesin stepping [58, 66]. However, the elastic restoring forces that act on the load attached to the kinesin stalk domain are in the order of magnitude of the forces generated by kinesin itself, and thus disturbances of the biophysical processes cannot be excluded and recorded data might contain artifacts [58, 65]. Additionally, the method suffers from an elaborate experiment prepa-

ration as catching a kinesin with the optical trap is tedious excluding high-throughput measurements. As the probe has so far been only attached to the kinesin stalk domain all reported optical trap studies solely gained insight about the center-of-mass movement of kinesin. Information about the behavior of the individual heads stays in the dark.

In the field of kinesin research, one of the most important single molecule tracking studies was reported by Yildiz et al [62]. A single Cy3 fluorophore was attached to one of the head groups of kinesin and the fluorescence photons of the emitter were collected on an EMCCD to extract the position by centroid fitting. Due to the limited localization efficiency, the stepping process had to be slowed down significantly to collect sufficient photons at each step position for clear resolution of the stepping distance. A camera integration time of 330 ms was required and as a consequence, the concentration of ATP had to be reduced to 340 nM. Physiological ATP concentrations are in a range of 0.5 mM to 5 mM [67].

In contrast to fluorescence microscopy, dark-field microscopy enables a higher STR as it employs light scattering nanoparticles as position probe. Since photo-bleaching is not an issue, higher laser powers can be employed providing a high detection photon rate, which in turn results in a high localization precision with sampling rates up to 20 kHz. Dark-field microscopy experiments revealed that kinesin's feet occasionally take 8 nm steps [57, 68]. In the reported studies gold nanoparticles or quantum dots with sizes from 30 to some hundred nanometer had to be attached to the heads of kinesin to reach a sufficient scattering cross section for optical position detection. Considering the step size of 16 nm as well as the relatively compact conformation of kinesin when attached to microtubules it has to be assumed that probes of this size could impede the stepping process [69].

In contrast, MINFLUX is optimally suited for tracking measurements of the kinesin heads' stepping movement. When using fluorescent single molecules, MINFLUX permits a temporal resolution about 1000 times higher than the camera-based study of Yildiz et al [62]. At physiological ATP concentrations the steps are too fast respectively too small to be resolved by camera-based approaches. Due to the increased localization efficiency of MINFLUX, we successfully resolved 16 nm steps at physiological ATP concentrations. In this minimally invasive study, we additionally showed that previously reported substeps and backsteps also occur in a load-free (i.e. no cargo in the form of nanospheres) stepping process.

MINFLUX Tracking of Kinesin's Stepping Behavior

The samples were prepared by Lukas Scheiderer[1] according to the protocol in Section 2.5.5.

Kinesin was labeled at one foot with Atto647N and microtubules were stained with Alexa Fluor 488 to identify filaments and enable the kinesin prelocalization routine. For this purpose, we first performed a 20x20 µm confocal scan with a 488 nm laser at low power. Suitable microtubules were selected by hand and the scanner was positioned accordingly. We usually chose microtubules oriented along the x-axis of our scanner system, as the prelocalization was more precise in x direction due to the slight ellipticity of our excitation spot. After defining the selected filament as region of interest, we illuminated this region with a 642 nm laser at low power and monitored the fluorescence count rate in the red detection channel. As soon as the rate exceeded a certain threshold (depending on the excitation power and sample background between 8 and 15 kHz), a MINFLUX measurement was triggered and a trace was recorded according to the procedure described in Section 3.1.1. We used an iterative zoom-in process with $L = 100$ nm in the first and $L = 60$ nm in the second step. The size of L in the last step of a data set varied from 30 to 40 nm as it was chosen in dependence of the individually measured SBR for each sample. The presented data were mostly acquired with $L = 30$ nm in the last step. This last step was repeated between 500 and 3000 times depending mainly on laser power and bleaching behavior of the dyes. On the one hand, the higher the laser power was set, the better the STR typically became due to the higher fluorescence photon rate. On the other hand, photo-bleaching occurred faster thus trading the gained resolution for shorter trace lengths with less steps tracked overall. The traces were evaluated with the fixed-curvature estimator described in Section 2.3.2. We usually only applied a minimum photon filter ($N_{min} = 5$) to filter out localizations during which the emitter was in an intermittent off-state. The resulting trace was fitted with the Matlab function *ischange* which detects sustained changes in a discrete signal trace. The fitted step sizes were evaluated. For a more detailed description refer to Section 2.4.2.

Results

A representative example trace of the kinesin step tracking is displayed in Figure 4.8. The trace was recorded at an ATP concentration of 100 µM and the position trace follows the emitter along the microtubule. For this kind of presentation, the x and y trace were rotated to segment the trace into a component parallel and perpendicular to the stepping

[1] Department for Optical Nanoscopy, Max-Planck-Institute for Medical Research, Heidelberg, Germany

direction. A moving median filter of rank 10 was applied to the signal for smoothing. Figure 4.8 **B** shows a histogram of the step size distribution. The average step size is 15.9 nm and agrees very well with the previously reported step size of 16.3 nm [70]. The data were recorded at an ATP concentration of 100 µM. To the best of our knowledge, this is the first time individual kinesin steps could be resolved in a light microscope at such high ATP concentrations. For comparison, Yildiz et al used a concentration of 340 nM [18].

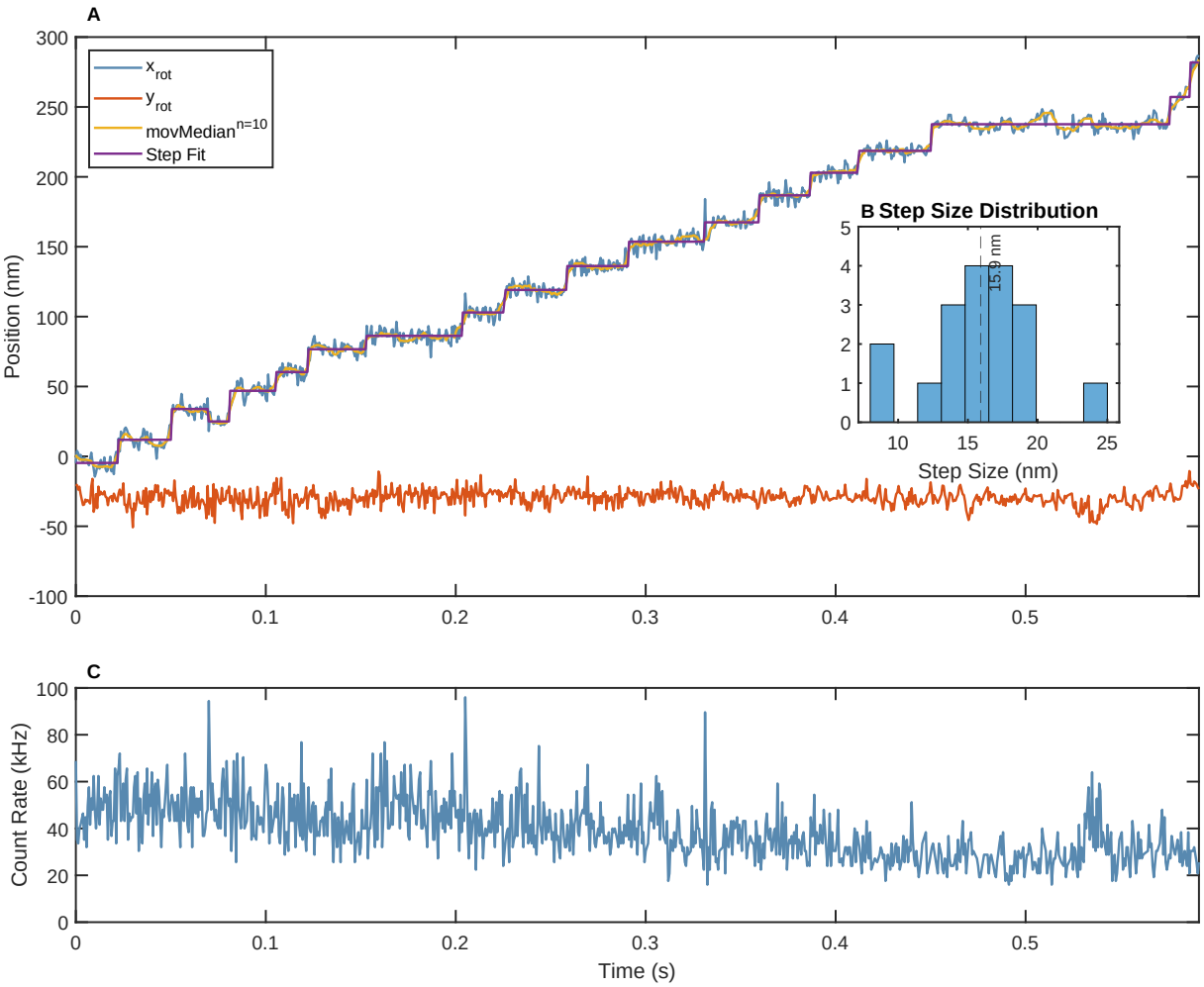

Figure 4.8: Representative trace of kinesin's stepping behavior The trace was recorded at an ATP concentration of 100 µM. **A** shows the trace components along and perpendicular to the microtubule orientation. As guidance, a moving median with a rank of 10 was added (yellow). To extract step sizes a step fit was added (purple). **B** Histogram of the step size distribution. The average step size is very close to the expected 16.3 nm. **C** Photon count rate. Due to the large range of movement of kinesin compared to the size of a diffraction limited spot, the counts decreased over time as the emitter moved to the edge of the phase scanner's FOV.

Additional traces are shown in Figure 4.9 and the Appendix. Overall, we collected and evaluated 68 traces with predominantly 16 nm steps and calculated the localization precision as well as the resulting STR. The detailed analysis is summarized in Table 4.3. The average fluorescence count rate was 38.9±9.7 kHz at an average photon count of 18.4 per

1D localization. The measurement time per 2D localization varied from 625 µs to 1260 µs with an average of 952 µs. With a measured mean SBR of 2.38, the best achievable localization precision was calculated to be 2.66 nm. Remarkably, the theoretical optimum was therefore only missed by a factor of two. Main sources of error are again vibrations coupling into the setup from the outside, sample drift during the measurement and internal system dynamics through flexible linkers.

Table 4.3: Localization precision and STR for Kinesin traces The achieved localization precision and STR are listed. The average detected count rate was 39.0 ± 9.7 kHz. This demonstrates the reliability and repeatablity of MINFLUX tracking of kinesin.

	MINFLUX Experimental Results	MINFLUX Theoretical Optimum	Expected Idealized Camera-based Localization
$\overline{\sigma}$ (nm)	5.19 ± 1.21 @N=18.3 (1D) @SBR=2.38	2.66 @N=18.4 (1D) @SBR=2.38	24.7 @N=36.8(2D) @SBR=∞
$\overline{STR}$ $(m\sqrt{s})$	$4.79 \cdot 10^{-10} \pm 1.2 \cdot 10^{-11}$	$2.46 \cdot 10^{-10}$	$2.29 \cdot 10^{-9}$

To compare our method to the established camera-based approach in this fluorescence rate regime, we calculated the localization precision for a background-free case and for a perfect camera. The theoretical localization precision and STR are a factor five worse than in the experimental MINFLUX case. This comparison highlights that even when comparing MINFLUX under experimental and camera-based localization at idealized conditions, MINFLUX heavily outperforms the latter. MINFLUX's superiority is especially pronounced at small photon counts per localization like it was the case in the presented experiment.

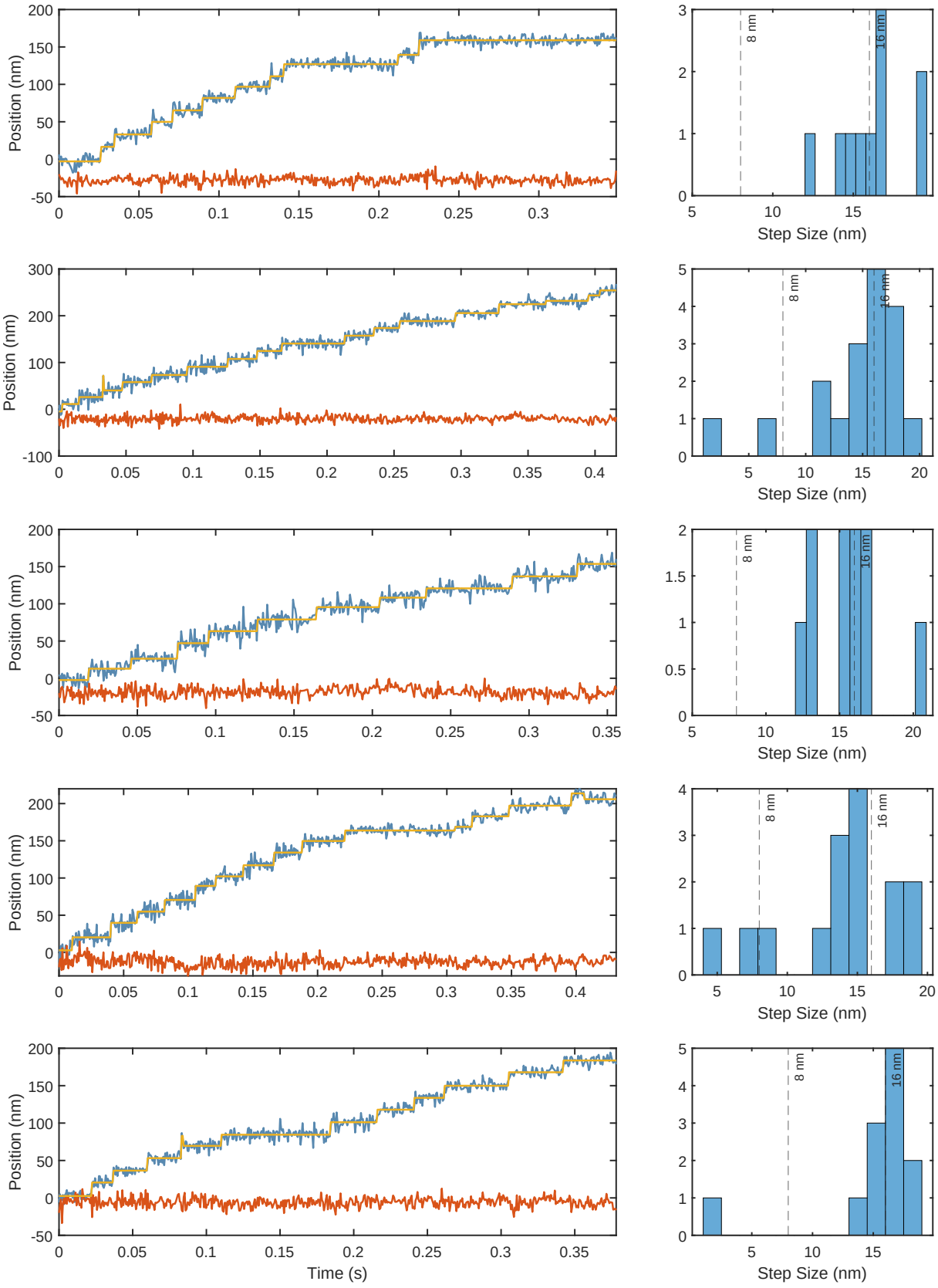

Figure 4.9: Additional traces showing kinesin's stepping behavior Analogous to Figure 4.8, the rotated postition traces, the median filtered position traces and the step fit with the *ischange* function are displayed for all traces. The second column of plots shows the distribution of the fitted step sizes.

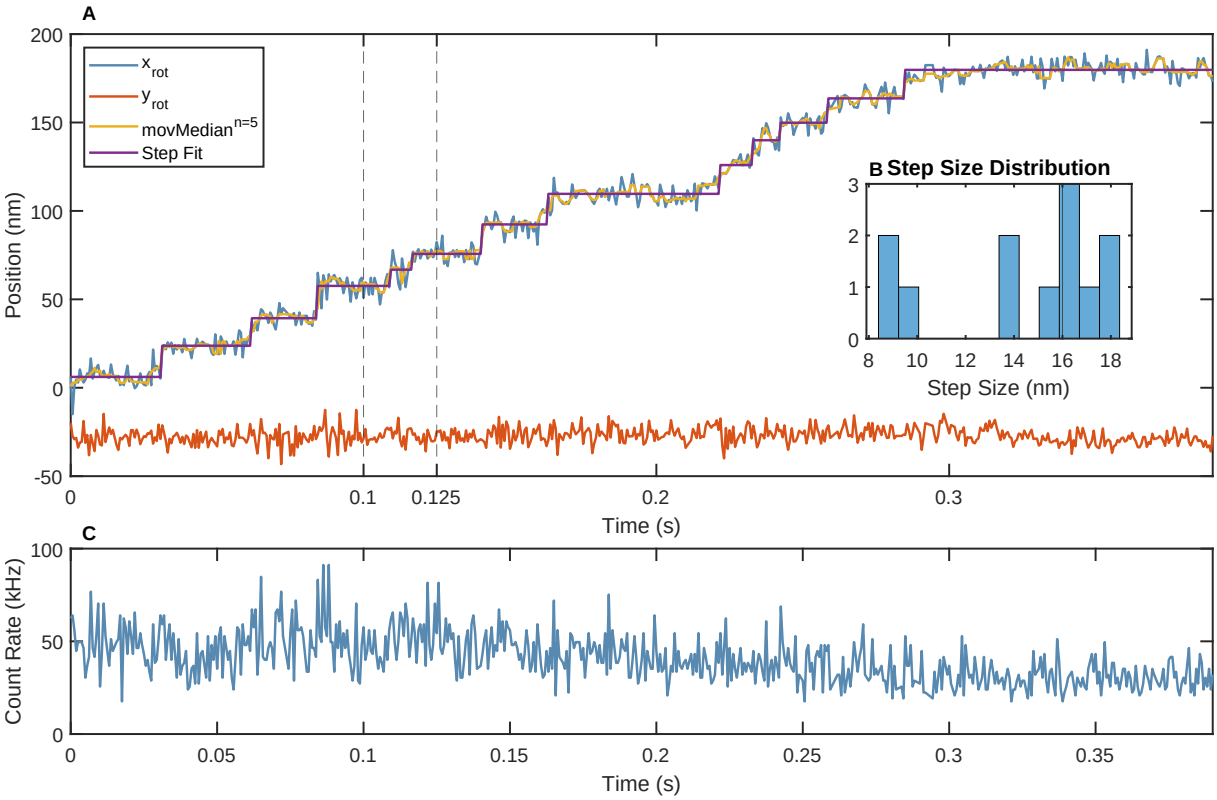

Figure 4.10: Representative trace of kinesin's stepping behavior including sub-steps The trace was recorded at an ATP concentration of 3 mM. **A** shows the trace components along and perpendicular to the MT orientation. A moving median with a rank of 5 was added to the figure. To extract step sizes a step fit with the *ischange* function was added. The step size distribution is shown in **B**. It indicates multiple steps with a size of $\sim$ 8 nm. Until now these steps were observed in dark-field or optical trap studies. These have the potential to disturb the native behavior of the motor protein. The detected count rate is shown in **C** and was $\sim$ 40 kHz.

In some cases, the labeled kinesin head takes an 8 nm step instead of an 16 nm one. The trace depicted in Figure 4.10 (recorded at an ATP concentration of 3 mM) shows two exemplary substeps between $t = 0.1$ s and $t = 0.125$ s. Additional traces with 16 and 8 nm steps are depicted in Figure 4.11. The occurrence of sub steps was previously reported for measurements where kinesin carried load or when it was attached to larger probing particles [57]. To the best of our knowledge, this is the first time that these sub-steps could be detected in a load-free, minimally invasive measurement under physiological ATP concentrations. Possible reasons for these sub-steps might be intermediate binding states during the stepping process [71–73]. However, an elaborate discussion of the underlying mechanism is outside the scope of this thesis.

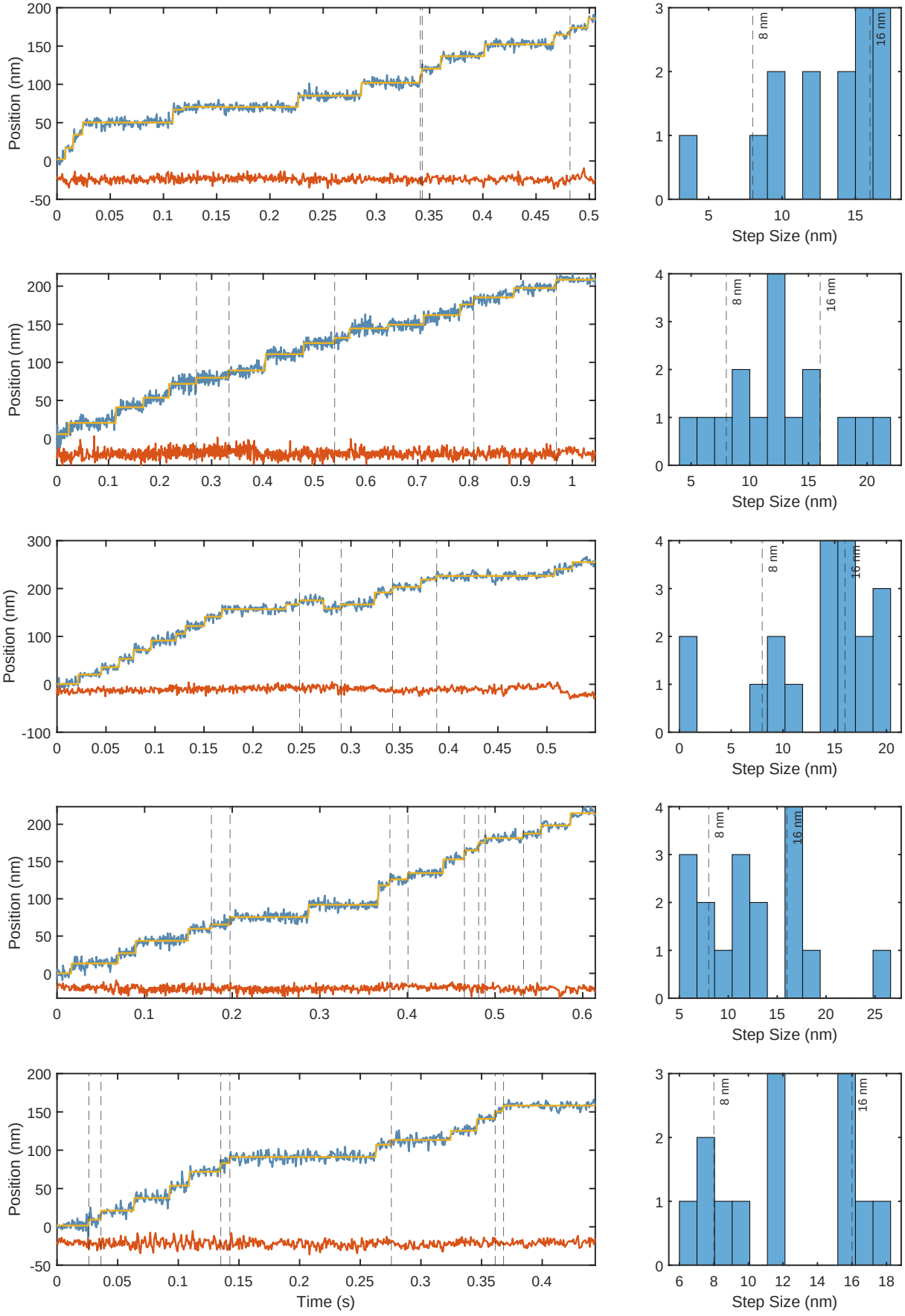

Figure 4.11: Additional kinesin traces with substeps confirming the reproducability
The plots display the data analogous to Figure 4.8 and 4.10. Steps in range from 6 nm to 12 nm are marked with a dashed line.

We demonstrated that by employing MINFLUX tracking we could observe and investigate the stepping behavior of Kinesin along microtubules. In agreement with previous reports, we found that Kinesin predominantly takes 16 nm steps and occasionally 8 nm sub-steps. Due to the high localization efficiency of MINFLUX, we were able to detect these steps at much higher STR than so far reported for any other SMT technique allowing us to be the first to acquire kinesin tracking data under physiological ATP concentrations. Due to the long dwell times that are necessary to detect steps of this size with camera-based tracking approaches, the stepping speed at physiological ATP concentrations excluded so far a measurement under these conditions.

4.5 Summary and Discussion

This chapter presented the application of the MINFLUX localization approach to study the dynamics of fluorescent single molecules in various samples. We used Atto 647N single molecules to show that MINFLUX enables tracking in a previously unreached STR regime.

We immobilized Atto647N on a coverslip surface and moved the sample in distinct nanoscopic patterns using the piezo-motorized stage. Tracking the fluorophores, we confirmed that the position trace recorded by our MINFLUX microscope resembles the target signal with high accuracy. We reached a localization precision of 2.43 to 2.67 nm at a photon rate of about 100 kHz. The STR varied between $1.83 \cdot 10^{-10}\ m\sqrt{s}$ and $2.02 \cdot 10^{-10}\ m\sqrt{s}$. Due to the influences discussed in Section 3.3 the experimental results deviate between 31 and 52% from the theoretical optimum. In comparison to the STR in a camera-based tracking experiment under ideal conditions, the STR of our experiments were between 5.8 to 6.4 times better.

As next level of complexity, we studied DNA nanorobots. Through stochastic break-up and formation of complementary base pairing with single-stranded track positions, the single-stranded nanorobot randomly explored the three-position wide track on a DNA baseplate. As the nanorobot was labeled with an Atto647N fluorescent single molecule, we were able to investigate this stepping between different track positions with our MINFLUX setup. We successfully resolved the steps ranging from ∼6 to ∼16 nm and followed the nanorobot movement of the nanobot over the DNA track for more than 5 s. The mean STR was high enough to detect the 6 nm steps on a time scale <4 ms. The localization precision was worse than the theoretical optimum due to multiple factors. From setup side the measurements suffered from a moderate sample drift and residual jitter of the galvanometer scanner both shifting localizations relative to each other. Additional in-

stabilities could have arisen from external vibrations and sound coupling into the setup. From sample side, a certain flexibility is required and implemented by design to enable the stepping of the nanobots from track position to track position. Thus, the fluorophore very likely explored the surrounding track position even if the nanorobot temporarily stood still, increasing the spread of localizations further. Detailed studies of the track position dynamics are necessary to quantify the contribution on the overall spread of the localizations.

To highlight that MINFLUX opens doors to novel insights in established biological fields, we performed tracking experiments studying the Kinesin-1 motor protein. By measuring the position of an Atto647N single molecule attached to one of the kinesin heads, we could repeatedly and reliably track kinesin's movement along microtubules. The predominantly detected step size of $\sim 16\,\mathrm{nm}$ coincides with the reported step sizes of 16.3 nm [70]. To the best of our knowledge, we are the first to additionally observe 8 nm sub-steps in a minimally invasive, no-load study and under physiological conditions. In comparison to the state-of-the-art SMT studies on kinesin, the here presented temporal resolution is over 300 times higher [18]. Even under ideal conditions for camera-based localizations, the experimentally achieved STR of MINFLUX would be unreachable with the camera-based appoach.

To improve the localization performance further, new methods to decrease background coming from the sample as well as the from the optical setup must be introduced. The stability of the setup can be increased by using a scanner with smaller position jitter. For a scanner with a piezo-electric driver, the feedback regulation can be turned off after the scanner is pointed at the molecule position. Then only the regulation precision of the high voltage amplifiers determines the pointing precision. This precision is expected to be below 0.1 nm. The resulting instability will be significantly smaller than for a galvanometer scanner. The sample stage is currently held by three piezo-electric motors attached in sequence to each other. This construction is connected via a single point of support to the microscope body, making the sample stage prone to resonant oscillations around this single point of support. A new stage construction using symmetrical points of support around the microscope objective would not only increase the vibration resistance, but also reduce the effects of thermal instabilities as thermal expansion would occur in a symmetric fashion around the objective and therefore largely compensate itself. By reconstructing the optical path of the setup in a more compact way, the influence of environmental factors like thermal drift and vibrations could be decreased further. Such an arrangement would also allow to implement a temperature stabilization for all essential components in a small compartment. Another important factor is the residual intensity in the PSFs minimum. The lower this intensity, the smaller the spatial multiplexing range L can be chosen. As the localization precision scales linearly with L, optimizing the quality

of the zero could lead to a significant improvement. An additional feature leaving room for improvement is the collected fluorescence rate. In our experiments we were rarely able to collect rates exceeding 100 kHz over an extended period of time. Newly developed dyes and anti-bleaching agents hopefully enable much higher rates in the future. Additionally, the detection efficiency could be increased by employing a 4π detection scheme [74]. With a second objective lens on top of the sample, the effective fluorescence rate could be increased by a factor of two. Details can be found in reference [37]. The obvious drawback would be a highly complex setup that requires more maintenance than our current MINFLUX microscope.

In conclusion, the presented experiments emphasize that our microscope and MINFLUX-based tracking methods in general have the unparalleled potential to establish new and groundbreaking life science research due to the increased localization efficiency. MINFLUX will be the first technique to introduce the new field of non-invasive nanoscale high-speed tracking in biological systems.

Chapter 5

Conclusion

Within this thesis, an architecturally new optical setup was envisioned and constructed to carry out MINFLUX localizations with high spatio-temporal resolution. To this end a simpler and more compact optical setup was built. Integral to its design was the development of the phase scanner, a single compact device that generates and scans various PSFs to perform MINFLUX localizations. To confirm the high localization efficiency of MINFLUX and the constructed setup test localizations on fluorescent single molecules were carried out. Tracking experiments in which these single molecules were moved by the motorized sample stage to test the agreement between target movement and the measured position trace were performed. The applicability to biomolecular research fields was verified by investigating the movement of DNA origami nanorobots over a track of predefined positions. Additionally, the stepping behavior of the Kinesin-1 motor protein along microtubules was studied.

MINFLUX offers a higher localization efficiency than conventional super-resolution microscopy techniques. Although the resolution of techniques like STED or PALM/STORM is in principle unlimited, in practice the localization precision and resolution rarely exceed 20 to 30 nm. MINFLUX on the other hand enables resolutions below 5 nm. To achieve this, the photons are rendered more informative by probing the molecule position with an excitation beam that features a local intensity minimum. The localization efficiency is optimal when the minimum is kept as close as possible to the molecule's position. To establish the position, the excitation beam is moved to multiple positions with spatial separation L close to the molecule. The smaller this separation becomes, the larger the information content that each photon carries will be. The established 2D localization approach was adapted to a fast sequence of 1D localizations with PSFs featuring a local minimum along one axis. Instead of a maximum likelihood estimator, a simple parabolic fit can serve as position estimator in this case. This simplified estimator can be readily

implemented in an FPGA board for real-time control of the measurement procedure. In a theoretical treatment it was shown that the remarkable localization efficiency of the established MINFLUX approach and the approach in which sequential 1D localizations are carried is equal.

The phase scanner is based on the concept of PSF synthesis by overlapping of individually phase controlled beamlets. The resulting curvature of the intensity around the probing minimum is higher than for the conventionally used donut beam. This improved curvature allows to measure with higher contrast at the same beam separation L and therefore reaches a higher precision, if all other parameters are held constant. Because the phase scanner is able to adapt to any wavelength in the visible spectrum only a single beam path is necessary. This permits the construction of a more compact and robust setup.

In this work, the phase scanner was used to carry out test localizations on fluorescent single molecules in two different excitation bands to assess the attainable localization precision and efficiency. Atto647N single molecules were localized in an iterative scheme by excitation with a laser wavelength of 640 nm. Here an average localization precision of 2.4 nm at 15 collected photons per dimension in the last MINFLUX step was reached. The investigation of Cy3B single molecules was carried out with an excitation wavelength of 561 nm. A localization precision of 3.5 nm with just 10 collected photons per dimension in the last step of the iterative procedure was achieved. Although deteriorating environmental influences were reduced by the design of the setup, they still contributed negatively to the achievable precision. The different contributions that prevented achieving the theoretically possible localization efficiency were discussed.

The information that can be gained from single molecule tracking depends decisively on the achieved spatio-temporal resolution (STR). For a set of experimental parameters (e.g. collected fluorescence rate, sampling time) it is defined as the product of spatial resolution and the square root of the sampling time. This relation reflects the inherent trade-off between spatial and temporal resolution. Increasing the sampling time to collect more photons in order to gain a higher spatial resolution diminishes the temporal resolution and vice versa. To evaluate the STR of our MINFLUX implementation, various single molecule tracking experiments were carried out.

Atto647N single molecules were immobilized on a coverslip surface and moved by the piezo-electric sample stage in preprogrammed patterns. The single molecules were tracked and the resulting tracking accuracy and precision was evaluated. Overall the agreement of the measured trace with the target signal was very high. A localization precision of 2.43 to 2.67 nm was reached at an average photon rate of ~ 100 kHz. The achieved STR was in range between $1.83 \cdot 10^{-10}\ m\sqrt{s}$ and $2.02 \cdot 10^{-10}\ m\sqrt{s}$. To compare the improvement, the

expected performance of an idealized camera-based tracking measurement was calculated. The MINFLUX measurement outperformed this hypothetical performance by about a factor of six.

To further demonstrate the improved STR, the stepping behavior of DNA origami nanorobots was studied. The DNA origami track was immobilized on the cover slip surface. It features discrete track positions where the feet of the nanorobot attach temporarily. By the design of the different DNA strands, the nanorobots can step between these track positions with step sizes between 6 and 16 nm. This movement was recorded for up to five-second-long traces. Discrete steps of the expected size were reliably resolved. The mean spatio-temporal resolution was high enough to detect 6 nm steps in less than four milliseconds. The achieved STR for the flattened trace was $3.6 \cdot 10^{-10}\ m\sqrt{s}$ and therefore 6.6 times better than possible in the case of idealized, camera-based tracking. Nevertheless, the localization precision in this experiment was about 35% reduced in comparison to the theoretical optimum at the measured SBR. Presumably, the precision was hampered by vibrations, sample drift and residual movement of the DNA nanorobots around the binding positions.

The motor protein kinesin-1 was investigated in a further tracking experiment. Kinesin takes discrete steps along microtubules to transport intracellular cargo. This movement is fueled by the hydrolyzation of ATP and the concentration of ATP in the medium surrounding kinesin determines the stepping frequency. When tracking the position of an Atto647N single molecule attached to one of the binding heads of kinesin, a localization precision of the flattened trace of about 5.19 nm at an average of 18.4 collected photons per dimension was reached. This resulted in a STR of $4.8 \cdot 10^{-10}\ m\sqrt{s}$ and was about 4.8 times better than an idealized camera-based tracking would enable. This extraordinarily high STR enabled us to observe the stepping under, until now inaccessible ATP concentrations. Previous fluorescence-based studies were carried out with ATP concentrations of below 1 µM. Due to the low localization efficiency of camera-based tracking methods the movement had to be slowed down significantly to be resolvable. In contrast to that, in this study discrete steps in the movement of kinesin were successfully detected at an ATP concentration up to 3 mM. To the best of our knowledge this represents the first time kinesin's stepping behavior was resolved at physiological ATP concentrations (0.5 mM – 5 mM) with a fluorescence microscope.

Notwithstanding the substantial localization and tracking performance MINFLUX offers, the theoretical limit of the localization precision could not be reached. Because of the high precision MINFLUX enables, environmental conditions and the stability of optical components that were previously tolerable are now a limiting factor. On top of the discussed, and partially addressed issues there are multiple further sources of noise.

To improve the localization performance, the passive stabilization of the optical setup should be advanced. This is possible by adding further layers of encapsulation. Arranging the necessary components on a custom-built monolithic design instead of the flexible, but more susceptible breadboard optics, would allow to reduce the size of the excitation beam path further. This would also make it possible to stabilize the temperature of all components connected by the monolith to a higher degree. Currently, the sample holder is attached to the microscope body by a single point of support. Replacing the current stage with a construction that is attached to the objective lens and arranged symmetrically around it would not only decrease the susceptibility to vibrations, but also limit thermal drift. In such an arrangement thermal drift would be largely compensated by symmetry. The sample drift in our setup typically amounted to $\sim 0.1\,\mathrm{nm}$ per second. As the recording times in the presented work rarely exceeded some seconds, the influence on the presented results is modest. However, for longer traces even such a small drift can become problematic, when the drift reaches into the realm of the desired resolution. Additionally to the discussed passive improvements, an active stabilization must be implemented to reach the highest possible precision and is in development at the time of writing this thesis.

Until now the localization precision in fluorescence microscopy and tracking studies typically was above 20 nm. Most labeling strategies for super-resolution were developed to work under these conditions. As MINFLUX reaches down to a single digit nanometer resolution, dye linkers with lengths in this range or larger can skew the accuracy and precision. The additional degrees of freedom for movement can decrease the SBR as the dye moves out of the PSF's local intensity minimum. Additionally, dyes attached to long linkers can temporarily stick to nearby molecules and feign a position multiple nanometer removed from the actual position of the complex of interest. The increased localization precision and resolution of MINFLUX demands the smallest possible distance between the investigated structure and the fluorescent marker. To be able to reach single digit nanometer resolution, the labeling density must be extremely high. To ensure a reliable localization of dense fluorophores, the potential of adjacent dye molecules to interact with each other must be studied in the future.

The single largest limiting factor for the attainable precision in an MINFLUX measurement is the SBR. To possibly reduce the background emission emerging from the sample, the phase scanner approach could be combined with a time gated detection. Currently, the phase scanner works best with single-frequency lasers because of their high coherence length. Whether the considerable technical effort to retool the setup to a pulsed excitation scheme is worthwhile should be investigated. Another possibility to reduce the background is to study the excitation wavelength dependence of the background contributions and consequently switch to the most promising excitation band. An important

factor limiting the SBR is non-zero intensity in the local minimum of the PSF. Calculations show that the main parameters governing the zero quality are the power balance and polarization of the interfering beamlets. While the polarization can be determined with high precision, fine tuning the power balance presents a significant challenge. The effective power balance and the zero quality are subject to significant drift over the course of a day. Due to this drift we refrained from optimizing the power balance further when an SBR of two was reached during test localizations with 20 nm fluorescent beads. Increasing the overall stability with the measures mentioned above might make it feasible to optimize the minimum intensity to a higher degree. Residual optical aberrations can further impair the quality of the local minimum. To limit their influence, in a future iteration of the setup all employed optical components must be examined for possible wavefront distortions and other beam imperfections. If these measures prove to be effective and a higher SBR may be reached, the beam separation L can be reduced. This would improve the efficiency of the localization process further. If fewer photons are necessary to reach the same precision, longer traces or higher precisions could become attainable. Addressing the issues mentioned above might allow to achieve a localization precision below a single nanometer with around 20 photons per dimension under experimental conditions.

By optimizing the iterative zoom-in process to decrease L continuously during a MINFLUX localization the efficiency could be increased further. Fewer photons would be needed until the optimal L for the molecule at hand is reached. The track length or the mean fluorescence rate could be increased to result in even more insightful data.

As the phase scanner is able to adapt to additional wavelengths by simply changing the applied voltages, an implementation of multi-color MINFLUX tracking is the logical next step. The advantage of excitation-based emitter separation is the possibility to track two non-blinking fluorophores with low experimental bleed-through by switching quickly between the two excitation wavelengths. This would enable dynamic colocalization studies with hitherto inaccessible spatio-temporal resolution.

In conclusion, the implementation of the interferometric phase scanner provided significant improvements to the required maintenance and the achievable spatio-temoral resolution of MINFLUX tracking. These improvements were demonstrated experimentally in various tracking experiments. Although advances have been made with this innovative setup, some factors still prevent theoretical limits from being reached. By implementing aspects of the strategies discussed above, together with advances in fluorescence labeling, it is realistic to think that true live tracking at molecular precision could soon be routinely measured using MINFLUX.

Appendix

Additional Nanorobot Traces

In this section additional nanorobot traces will be displayed. The collection of these selected shows how the heterogenity of the individual measurement results. Currently we are not able to disentangle the variance of the individual objects from the detrimental environmental influences that can lead to a distortion from the expected appearance described in Section 4.4.2.

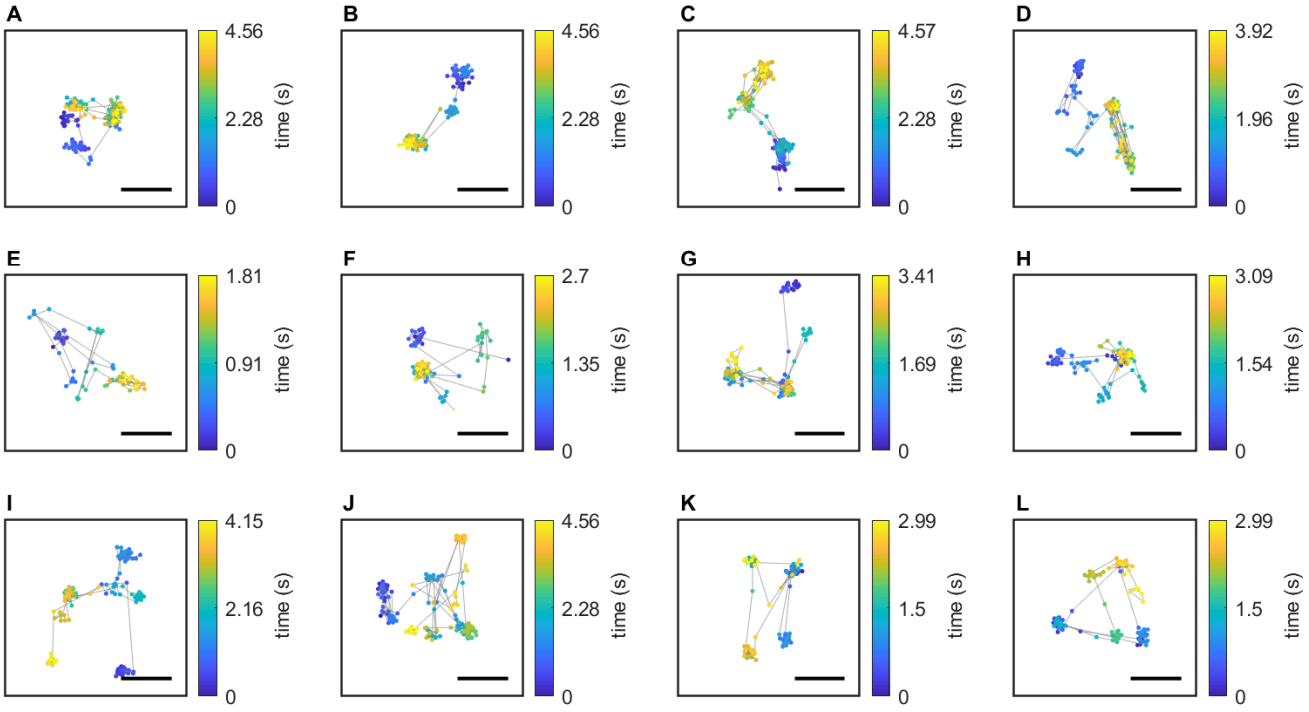

Figure 5.1: All Figures show MINFLUX tracking measurements. **A-C**: 3F nanorobots **D - L**: 5F nanorobots. The traces display the localizations color coded according to their time of localization. Scale bars, 10 nm

Additional Kinesin traces

Kinesin with 16 nm Steps

In the following additional Kinesin traces with predominantly 16 nm will be displayed. The large number of high quality traces shows the reproducability of MINFLUX tracking and the possibility to gain large statistics if the samples allow it.

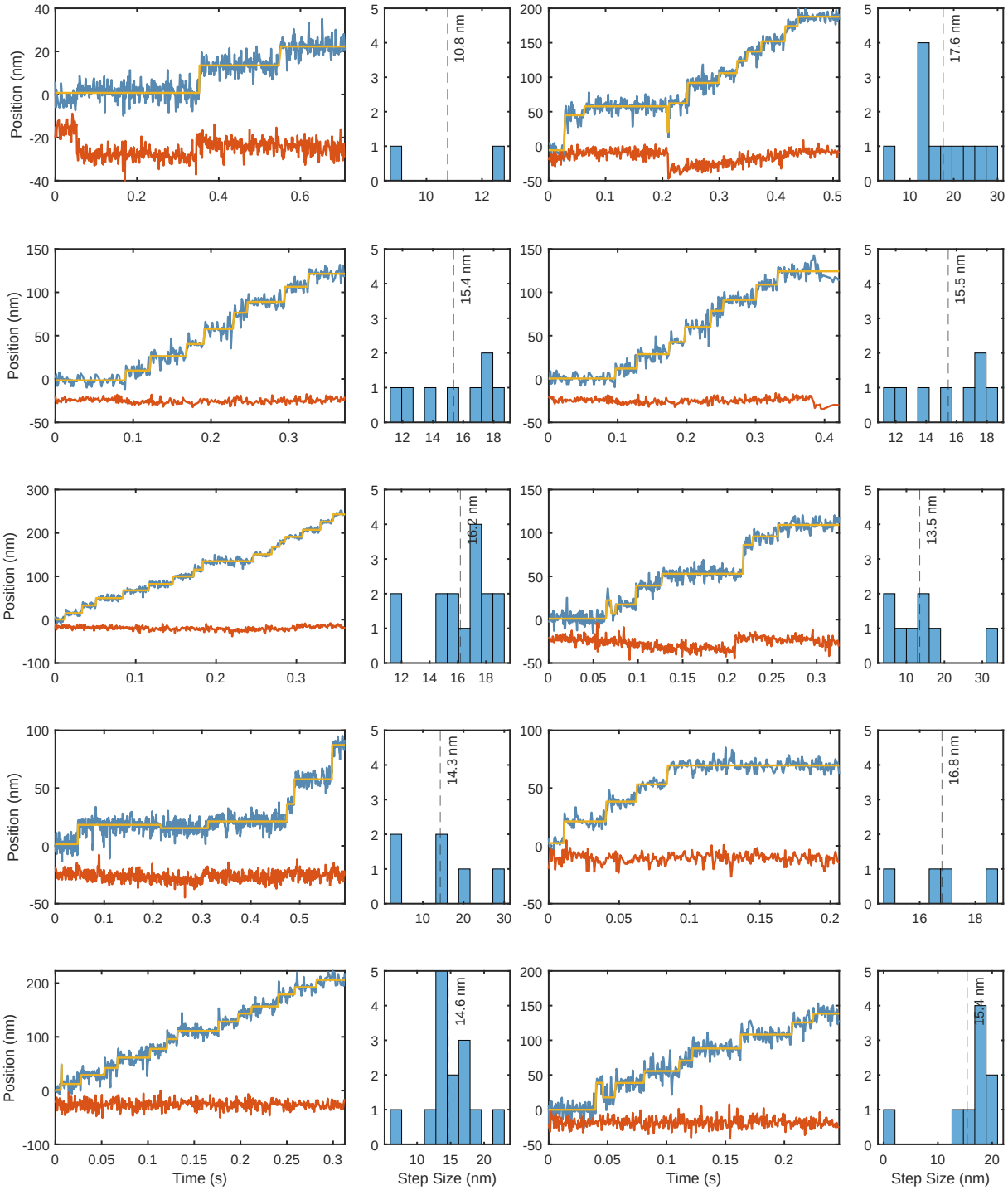

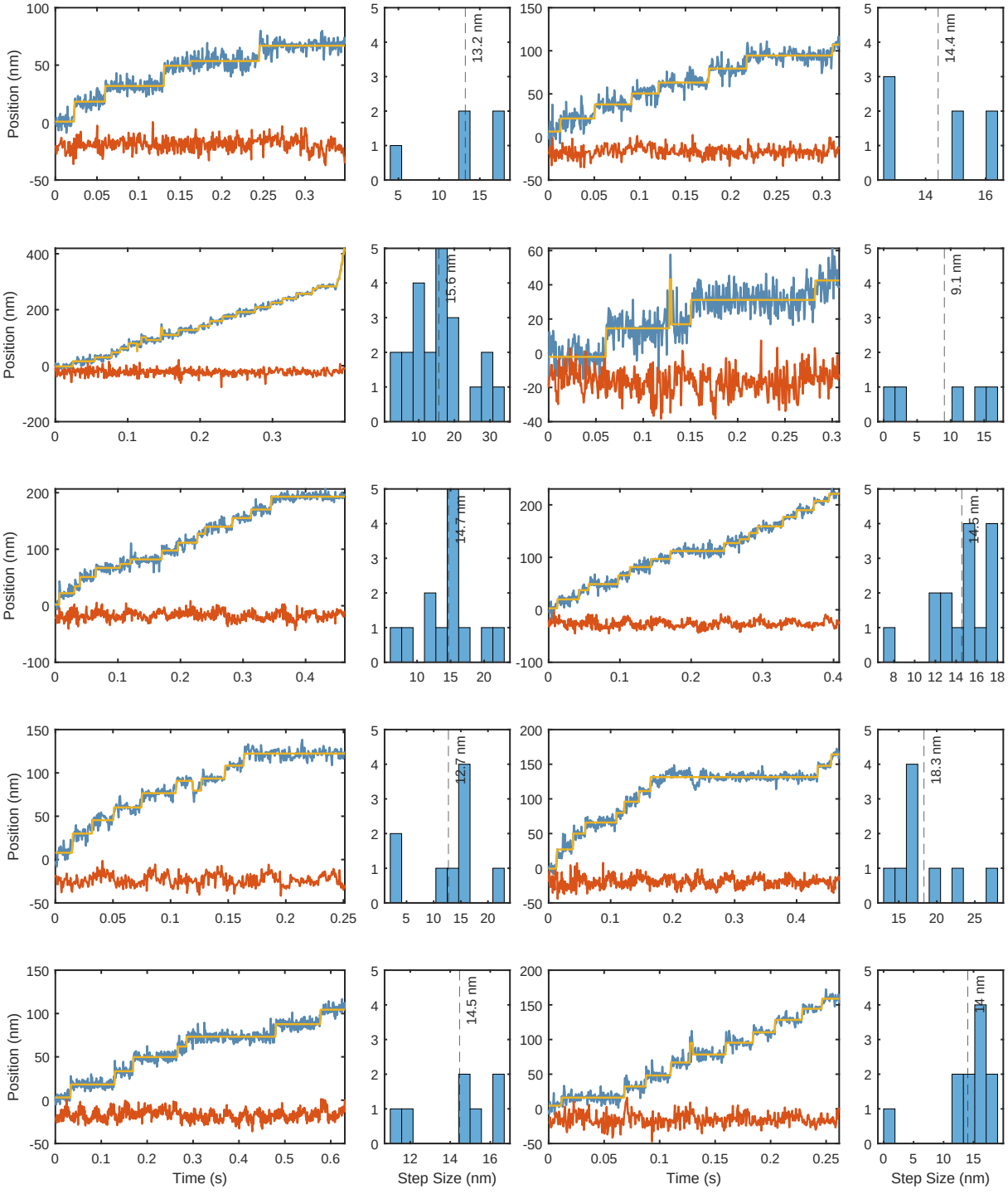
Position (nm)
13.2 nm
14.4 nm
15.6 nm
9.1 nm
14.7 nm
14.5 nm
12.7 nm
18.3 nm
14.5 nm
14 nm
Time (s)
Step Size (nm)
Time (s)
Step Size (nm)

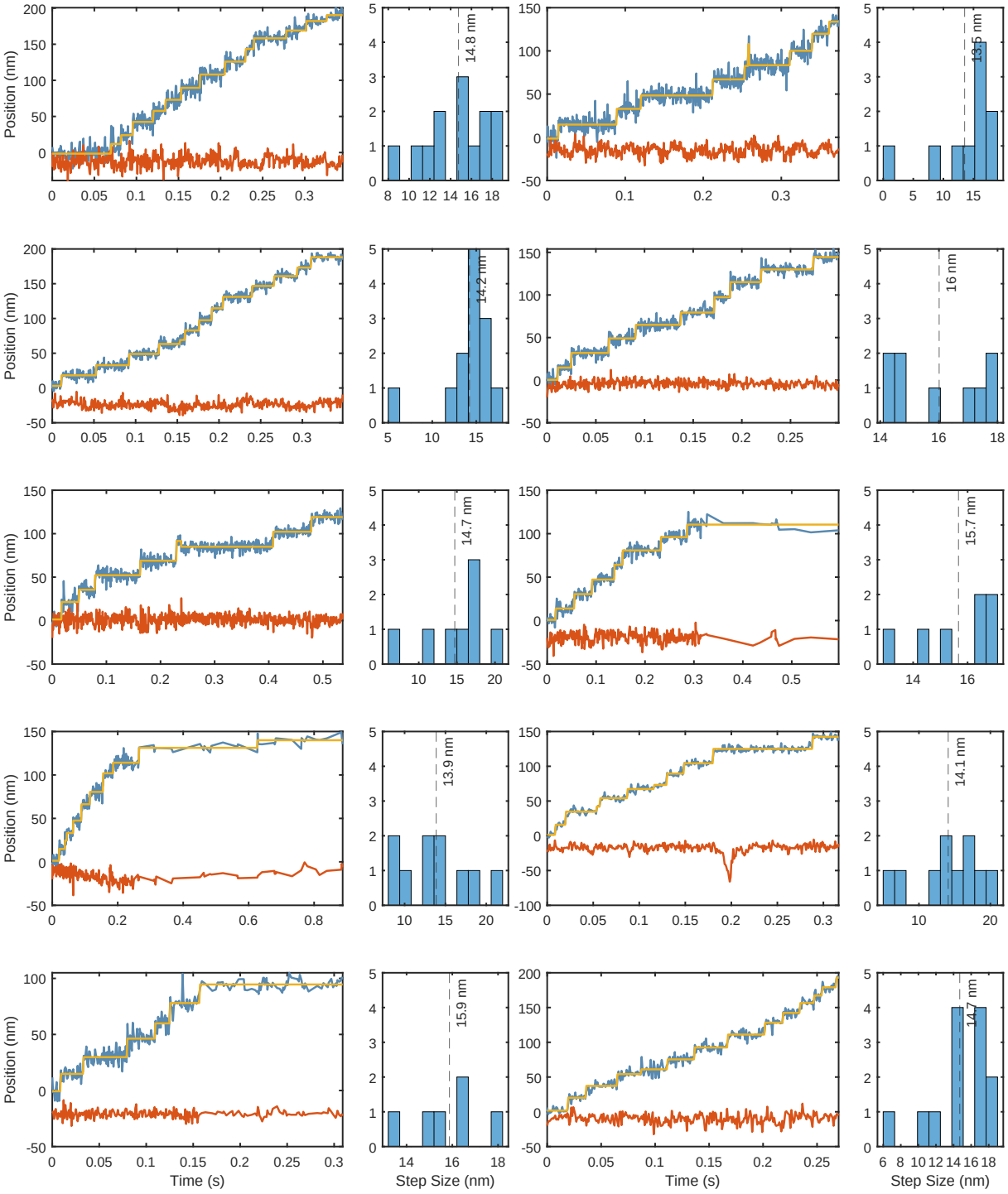
Position (nm)
14.8 nm
13.5 nm
14.2 nm
16 nm
14.7 nm
15.7 nm
13.9 nm
14.1 nm
15.9 nm
14.7 nm
Time (s)
Step Size (nm)
Time (s)
Step Size (nm)

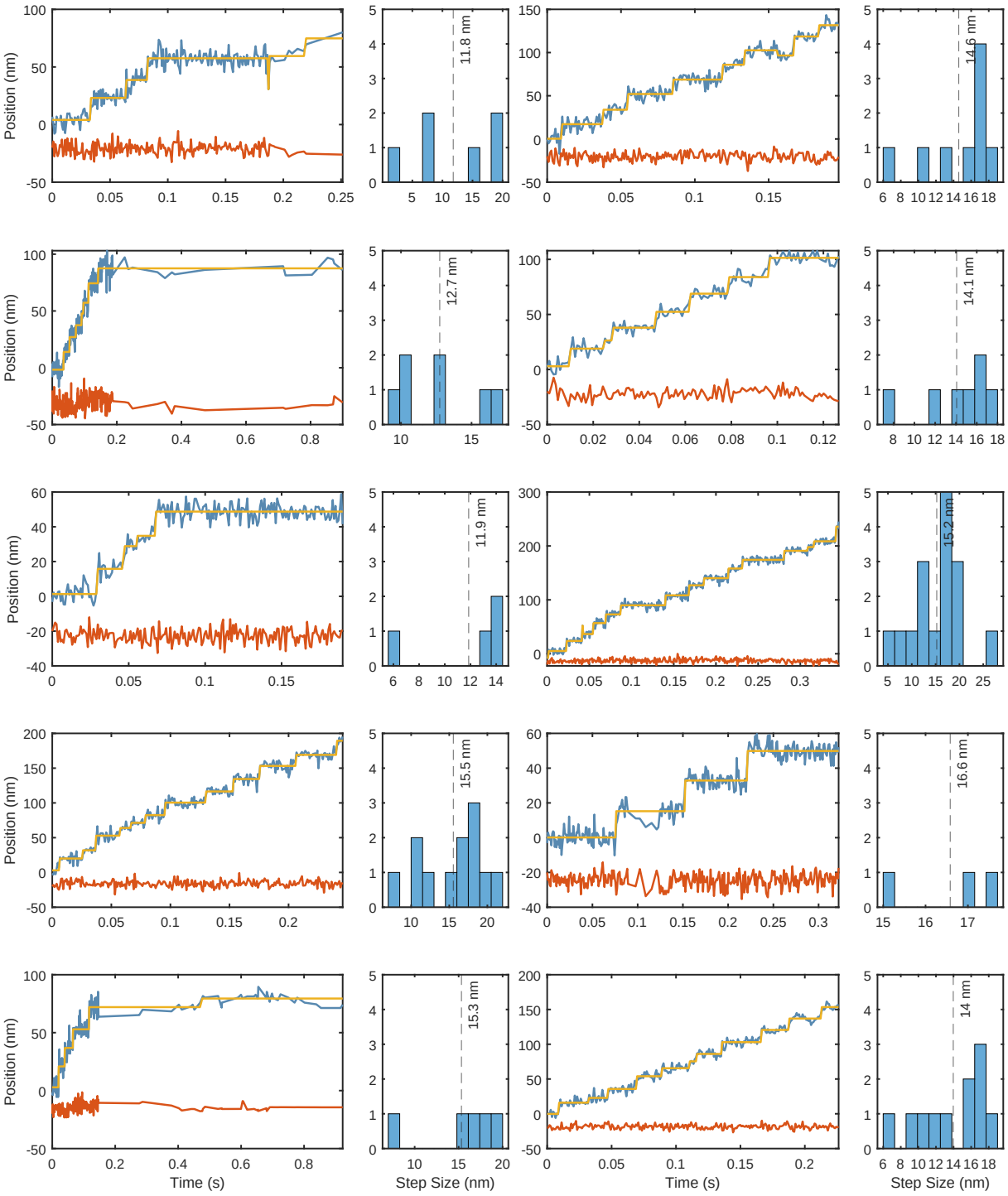
Position (nm)
11.8 nm
14.6 nm
12.7 nm
14.1 nm
11.9 nm
15.2 nm
15.5 nm
16.6 nm
15.3 nm
14 nm
Time (s)
Step Size (nm)

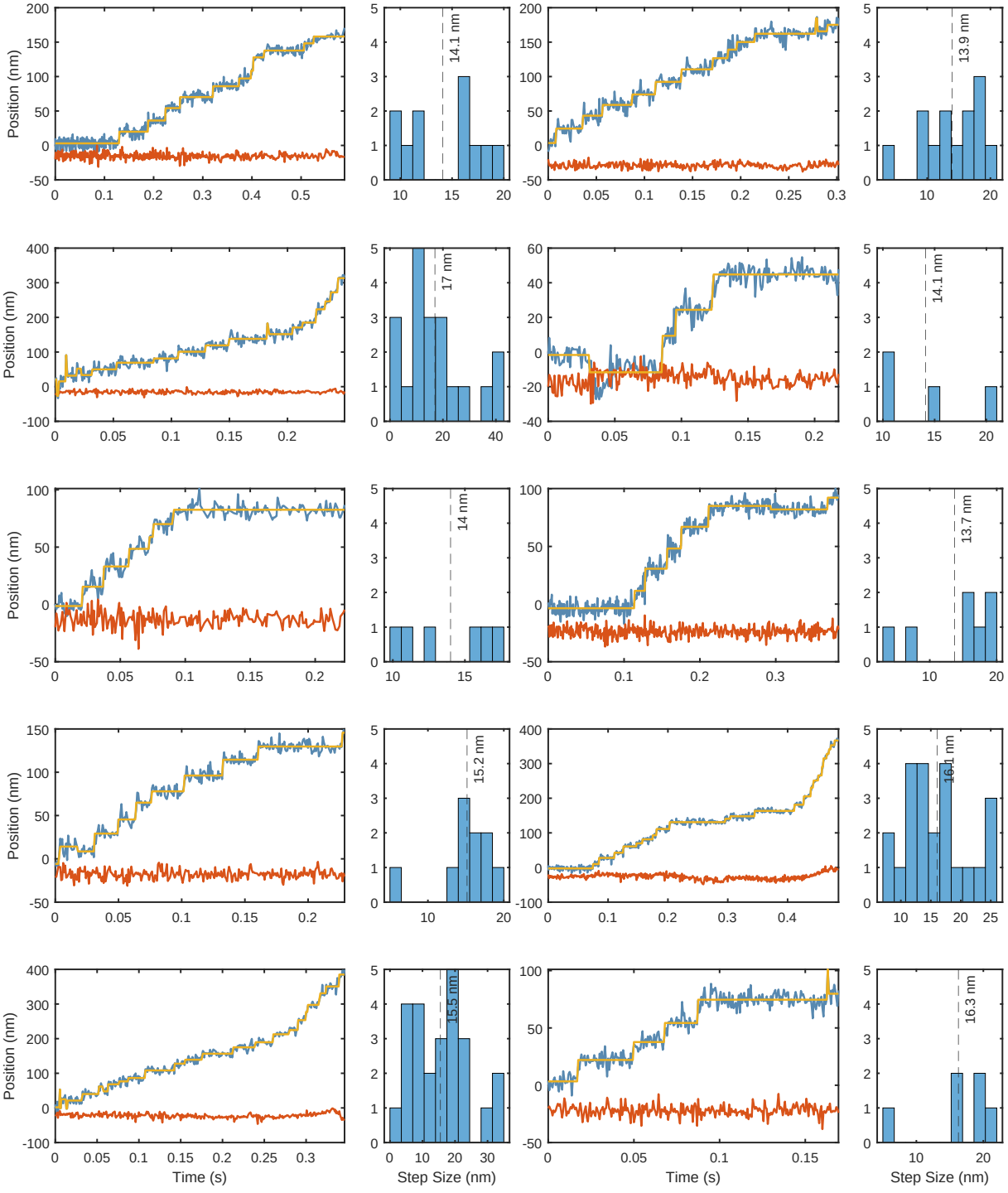
Position (nm)
14.1 nm
13.9 nm
17 nm
14.1 nm
14 nm
13.7 nm
15.2 nm
16.1 nm
15.5 nm
16.3 nm
Time (s)
Step Size (nm)
Time (s)
Step Size (nm)

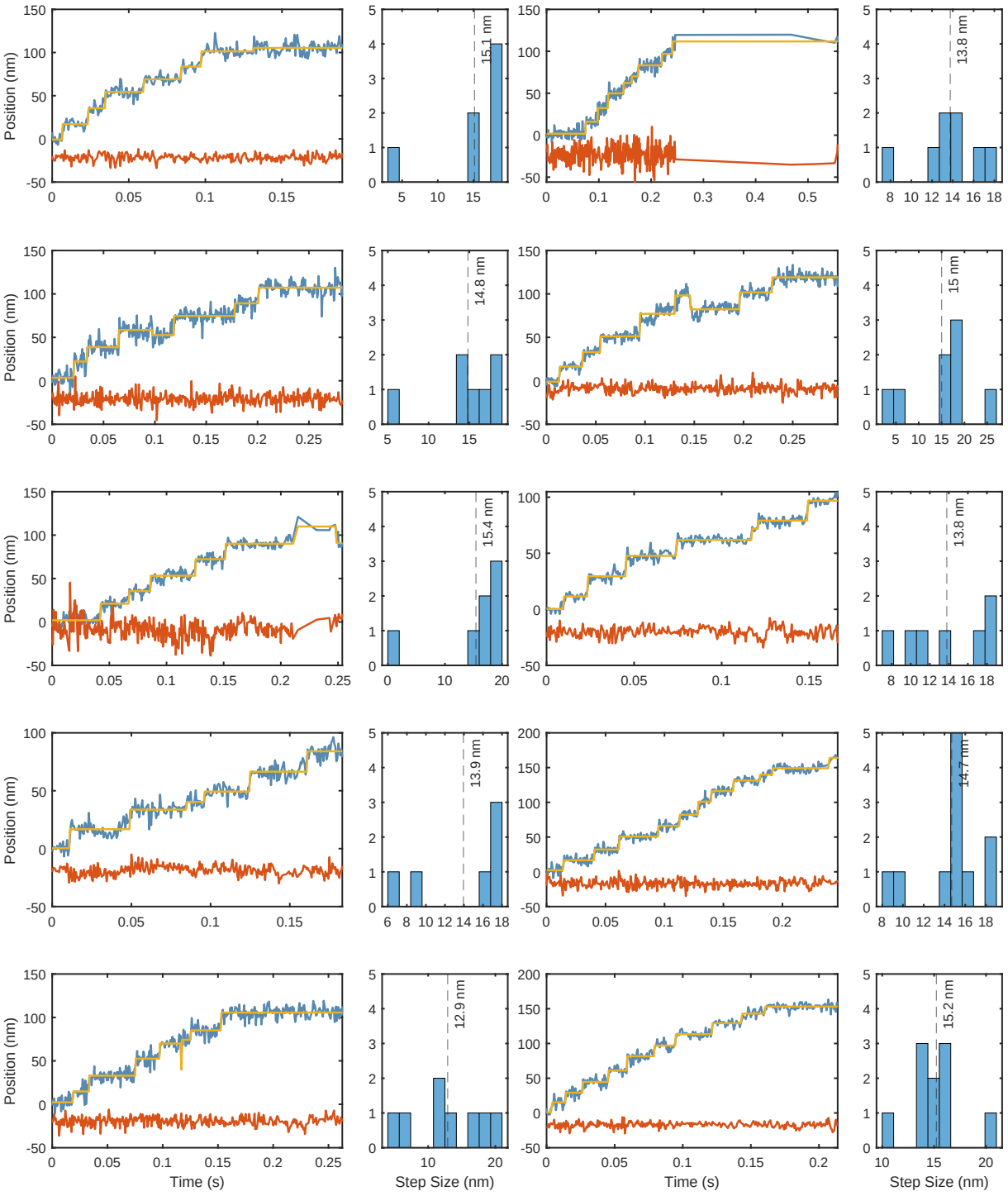
Position (nm)
Time (s)
Step Size (nm)
15.1 nm
13.8 nm
14.8 nm
15 nm
15.4 nm
13.8 nm
13.9 nm
14.7 nm
12.9 nm
15.2 nm

Kinesin with 16 nm and 8 nm Steps

In the following additional Kinesin traces with 16 nm and also 8 nm steps will be displayed.

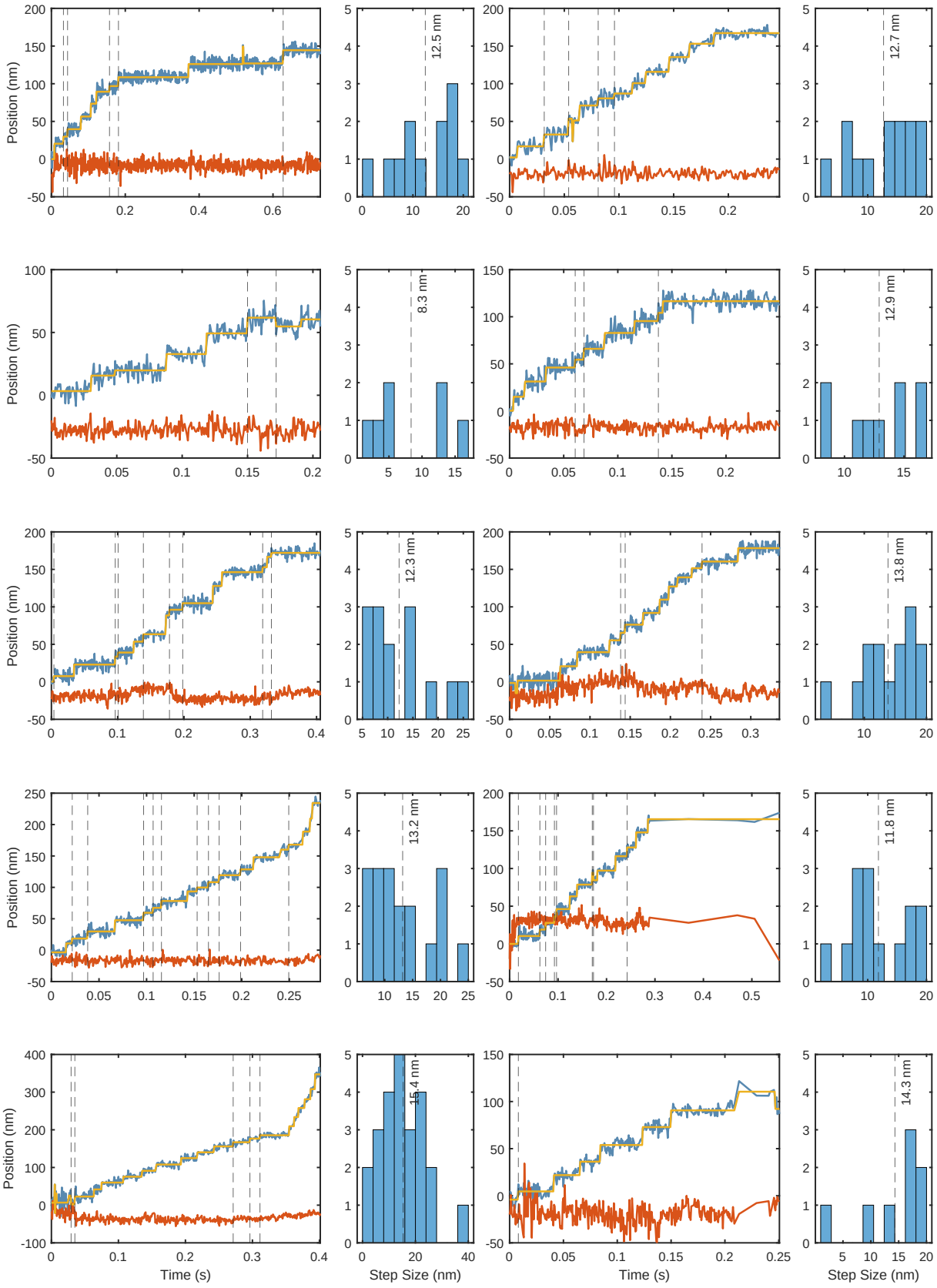

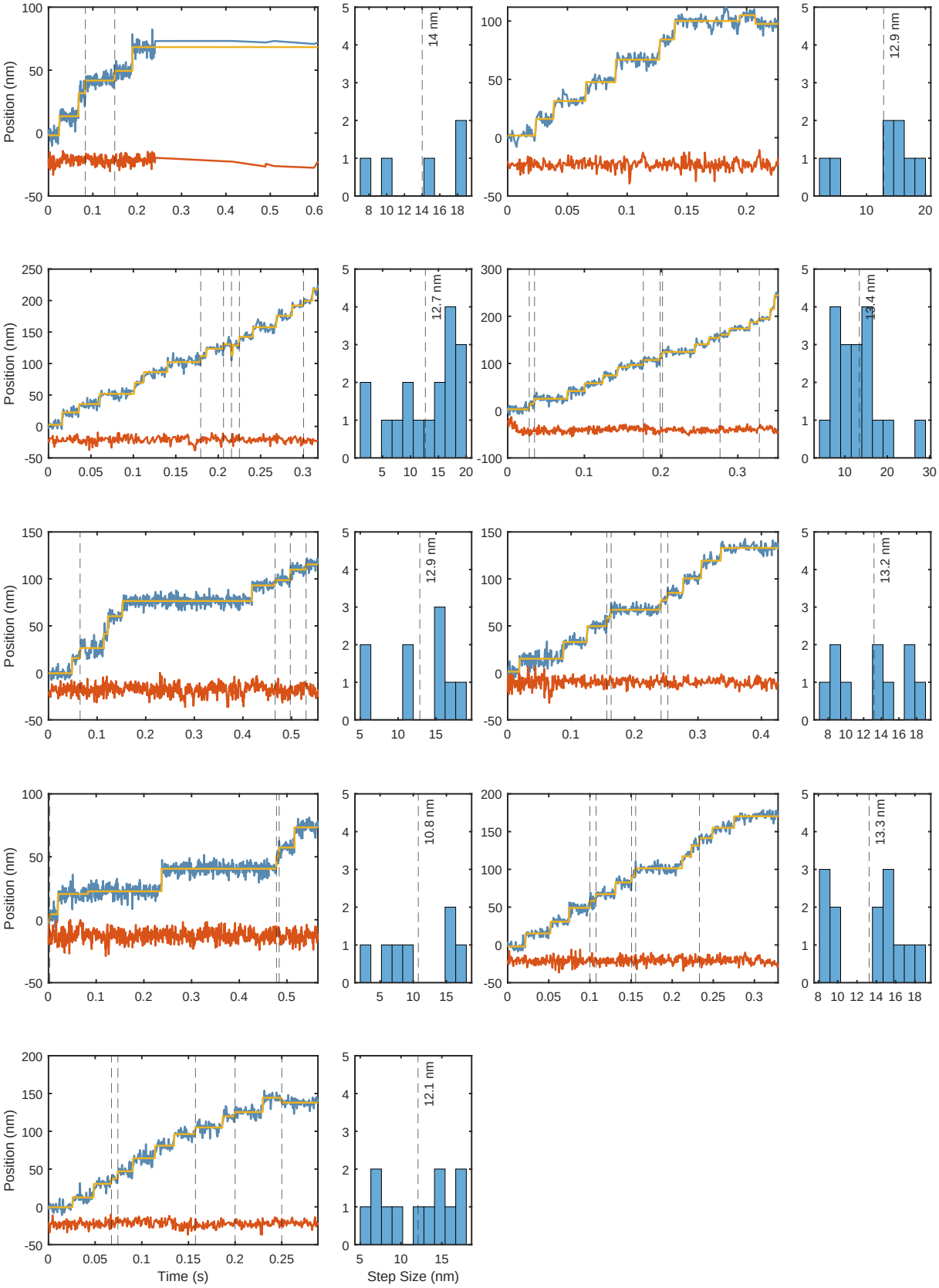
Position (nm)
14 nm
12.9 nm
12.7 nm
13.4 nm
12.9 nm
13.2 nm
10.8 nm
13.3 nm
12.1 nm
Time (s)
Step Size (nm)

List of Tables

List of Figures

Bibliography

[1] E. Abbe. Beiträge zur Theorie des Mikroskops und der mikroskopischen Wahrnehmung. *Archiv für Mikroskopische Anatomie 1873 9:1*, 9(1):413–468, dec 1873.

[2] Stefan W. Hell and Jan Wichmann. Breaking the diffraction resolution limit by stimulated emission: stimulated-emission-depletion fluorescence microscopy. *Optics Letters, Vol. 19, Issue 11, pp. 780-782*, 19(11):780–782, jun 1994.

[3] Thomas A. Klar, Egbert Engel, and Stefan W. Hell. Breaking Abbe's diffraction resolution limit in fluorescence microscopy with stimulated emission depletion beams of various shapes. *Physical Review E - Statistical Physics, Plasmas, Fluids, and Related Interdisciplinary Topics*, 64(6):9, 2001.

[4] Eric Betzig, George H. Patterson, Rachid Sougrat, O. Wolf Lindwasser, Scott Olenych, Juan S. Bonifacino, Michael W. Davidson, Jennifer Lippincott-Schwartz, and Harald F. Hess. Imaging Intracellular Fluorescent Proteins at Nanometer Resolution. *Science*, 313(5793):1642–1645, sep 2006.

[5] Michael J Rust, Mark Bates, and Xiaowei Zhuang. Sub-diffraction-limit imaging by stochastic optical reconstruction microscopy (STORM). *Nature Methods 2006 3:10*, 3(10):793–796, aug 2006.

[6] Samuel T. Hess, Thanu P. K. Girirajan, and Michael D. Mason. Ultra-High Resolution Imaging by Fluorescence Photoactivation Localization Microscopy. *Biophysical Journal*, 91(11):4258, 2006.

[7] Werner Heisenberg. The Physical Principles of the Quantum Theory. *Chicago Univ. Press*, 1930.

[8] Norman Bobroff. Position measurement with a resolution and noise-limited instrument. *Review of Scientific Instruments*, 57(6):1152, jun 1998.

[9] Russell E. Thompson, Daniel R. Larson, and Watt W. Webb. Precise Nanometer Localization Analysis for Individual Fluorescent Probes. *Biophysical Journal*, 82(5):2775–2783, may 2002.

[10] Kim I Mortensen, L Stirling Churchman, James A Spudich, and Henrik Flyvbjerg. Optimized localization analysis for single-molecule tracking and super-resolution microscopy. *Nature Methods 2010 7:5*, 7(5):377–381, apr 2010.

[11] J Vogelsang, R Kasper, R Steinhauer, B Person, M Heilemann, Markus Sauer, and P Tinnefeld. A reducing and oxidizing system minimizes photobleaching and blinking of fluorescent dyes. *Angewandte Chemie (International ed. in English)*, 47(29):5465–5469, jul 2008.

[12] Qinsi Zheng, Manuel F. Juette, Steffen Jockusch, Michael R. Wasserman, Zhou Zhou, Roger B. Altman, and Scott C. Blanchard. Ultra-stable organic fluorophores for single-molecule research. *Chemical Society Reviews*, 43(4):1044–1056, jan 2014.

[13] Soham Samanta, Wanjun Gong, Wen Li, Amit Sharma, Inseob Shim, Wei Zhang, Pintu Das, Wenhui Pan, Liwei Liu, Zhigang Yang, Junle Qu, and Jong Seung Kim. Organic fluorescent probes for stochastic optical reconstruction microscopy (STORM): Recent highlights and future possibilities. *Coordination Chemistry Reviews*, 380:17–34, feb 2019.

[14] Francisco Balzarotti, Yvan Eilers, Klaus C Gwosch, Arvid H Gynnå, Volker Westphal, and Stefan W. Hell. Nanometer resolution imaging and tracking of fluorescent. *Science*, 9913(December):1–13, 2016.

[15] Klaus C. Gwosch, Jasmin K. Pape, Francisco Balzarotti, Philipp Hoess, Jan Ellenberg, Jonas Ries, and Stefan W. Hell. MINFLUX nanoscopy delivers 3D multicolor nanometer resolution in cells. *Nature Methods*, 17(2):217–224, feb 2020.

[16] Jasmin K. Pape, Till Stephan, Francisco Balzarotti, Rebecca Büchner, Felix Lange, Dietmar Riedel, Stefan Jakobs, and Stefan W. Hell. Multicolor 3D MINFLUX nanoscopy of mitochondrial MICOS proteins. *Proceedings of the National Academy of Sciences*, 117(34):202009364, aug 2020.

[17] Roman Schmidt, Tobias Weihs, Christian A. Wurm, Isabelle Jansen, Jasmin Rehman, Steffen J. Sahl, and Stefan W. Hell. MINFLUX nanometer-scale 3D imaging and microsecond-range tracking on a common fluorescence microscope. *Nature Communications 2021 12:1*, 12(1):1–12, mar 2021.

[18] Ahmet Yildiz† And and † Paul R. Selvin*. Fluorescence Imaging with One Nanometer Accuracy: Application to Molecular Motors. *Accounts of Chemical Research*, 38(7):574–582, jul 2005.

[19] Stefan W. Hell. Far-field optical nanoscopy. *Science*, 316(5828):1153–1158, may 2007.

[20] Johann G. Danzl, Sven C. Sidenstein, Carola Gregor, Nicolai T. Urban, Peter Ilgen, Stefan Jakobs, and Stefan W. Hell. Coordinate-targeted fluorescence nanoscopy with multiple off states. *Nature Photonics 2016 10:2*, 10(2):122–128, jan 2016.

[21] Andreas Schönle, Benjamin Harke, Chaitanya K. Ullal, Jan Keller, Stefan W. Hell, and Volker Westphal. Resolution scaling in STED microscopy. *Optics Express, Vol. 16, Issue 6, pp. 4154-4162*, 16(6):4154–4162, mar 2008.

[22] Michael Hofmann, Christian Eggeling, Stefan Jakobs, and Stefan W. Hell. Breaking the diffraction barrier in fluorescence microscopy at low light intensities by using reversibly photoswitchable proteins. *Proceedings of the National Academy of Sciences*, 102(49):17565–17569, dec 2005.

[23] Sebastian van de Linde, Anna Löschberger, Teresa Klein, Meike Heidbreder, Steve Wolter, Mike Heilemann, and Markus Sauer. Direct stochastic optical reconstruction microscopy with standard fluorescent probes. *Nature Protocols 2011 6:7*, 6(7):991–1009, jun 2011.

[24] Joerg Schnitzbauer, Maximilian T Strauss, Thomas Schlichthaerle, Florian Schueder, and Ralf Jungmann. Super-resolution microscopy with DNA-PAINT. *Nature Protocols 2017 12:6*, 12(6):1198–1228, may 2017.

[25] Yvan Eilers, Haisen Ta, Klaus C Gwosch, Francisco Balzarotti, and Stefan W Hell. MINFLUX monitors rapid molecular jumps with superior spatiotemporal resolution. *Proceedings of the National Academy of Sciences of the United States of America*, page 201801672, may 2018.

[26] R. A. Minasian. MODULATORS | Modulation and Demodulation of Optical Signals. *Encyclopedia of Modern Optics, Five-Volume Set*, pages 129–138, jan 2005.

[27] Johann Engelhardt, Matthias Reuss, and Stefan W. Hell. Birefringent device converts a standard scanning microscope into a STED microscope that also maps molecular orientation. *Optics Express, Vol. 18, Issue 2, pp. 1049-1058*, 18(2):1049–1058, jan 2010.

[28] B. Richards and E. Wolf. Electromagnetic diffraction in optical systems, II. Structure of the image field in an aplanatic system. *Proceedings of the Royal Society of London. Series A. Mathematical and Physical Sciences*, 253(1274):358–379, dec 1959.

[29] Kenneth Levenberg. A method for the solution of certain non-linear problems in least squares. *Quarterly of Applied Mathematics*, 2:164–168, 1944.

[30] Donald. W. Marquardt. An Algorithm for Least-Squares Estimation of Nonlinear Parameters. *Journal of the Society for Industrial and Applied Mathematics*, 11(2):431–441, 1963.

[31] Frederik Gorlitz, Patrick Hoyer, Henning Falk, Lars Kastrup, Johann Engelhardt, and Stefan Hell. A STED Microscope Designed for Routine Biomedical Applications (Invited Paper). *Progress In Electromagnetics Research*, 147:57–68, 2014.

[32] Johann Engelhardt. Verfahren und vorrichtung zur dynamischen verlagerung eines lichtstrahls gegenüber einer den lichtstrahl fokussierenden optik, 2009.

[33] *Matlab 2021a Documentation*. The MathWorks, Inc, 2021.

[34] R. Killick, P. Fearnhead, and I. A. Eckley. Optimal Detection of Changepoints With a Linear Computational Cost. *http://dx.doi.org/10.1080/01621459.2012.737745*, 107(500):1590–1598, 2012.

[35] VectorLaboratories VectaCell Datasheet and Description, 2021.

[36] Michio Tomishige and Ronald D. Vale. Controlling Kinesin by Reversible Disulfide Cross-LinkingIdentifying the Motility-Producing Conformational Change. *Journal of Cell Biology*, 151(5):1081–1092, nov 2000.

[37] Marcus Oliver Held. *4Pi-MINFLUX localizations of fluorescent molecules*. Phd thesis, Max-Planck-Institute for medical research, 2021.

[38] Hugo Bachmann, Walter J. Ammann, Florian Deischl, Josef Eisenmann, Ingomar Floegl, Gerhard H. Hirsch, Günter K. Klein, Göran J. Lande, Oskar Mahrenholtz, Hans G. Natke, Hans Nussbaumer, Anthony J. Pretlove, Johann H. Rainer, Ernst-Ulrich Saemann, and Lorenz Steinbeisser. *Vibration Problems in Structures*. Birkhäuser Basel, Basel, 1995.

[39] Simon Sindbert, Stanislav Kalinin, Hien Nguyen, Andrea Kienzler, Lilia Clima, Willi Bannwarth, Bettina Appel, Sabine Müller, and Claus A. M. Seidel. Accurate Distance Determination of Nucleic Acids via Förster Resonance Energy Transfer: Implications of Dye Linker Length and Rigidity. *Journal of the American Chemical Society*, 133(8):2463–2480, mar 2011.

[40] Lawrence S. B. Goldstein and Alastair Valentine Philp. The Road Less Traveled1: Emerging Principles of Kinesin Motor Utilization. *http://dx.doi.org/10.1146/annurev.cellbio.15.1.141*, 15:141–183, nov 2003.

[41] Alex Carisey, Matthew Stroud, Ricky Tsang, and Christoph Ballestrem. Fluorescence Recovery After Photobleaching. *Methods in Molecular Biology*, 769:387–402, 2011.

[42] Yu Tian, Michelle M. Martinez, and Dimitri Pappas. Fluorescence Correlation Spectroscopy: A Review of Biochemical and Microfluidic Applications. *Applied spectroscopy*, 65(4):115, apr 2011.

[43] Nan Li, Rong Zhao, Yahong Sun, Zi Ye, Kangmin He, and Xiaohong Fang. Single-molecule imaging and tracking of molecular dynamics in living cells. *National Science Review*, 4(5):739–760, sep 2017.

[44] Darrell J. Irvine, Marco A. Purbhoo, Michelle Krogsgaard, and Mark M. Davis. Direct observation of ligand recognition by T cells. *Nature 2002 419:6909*, 419(6909):845–849, oct 2002.

[45] Rodrigo Reyes-Lamothe, David J. Sherratt, and Mark C. Leake. Stoichiometry and Architecture of Active DNA Replication Machinery in Escherichia coli. *Science*, 328(5977):498–501, apr 2010.

[46] Hurd DD and Saxton WM. Kinesin mutations cause motor neuron disease phenotypes by disrupting fast axonal transport in Drosophila. *Genetics*, 144(3):1075–1085, 1996.

[47] Evan Reid, Mark Kloos, Allison Ashley-Koch, Lori Hughes, Simon Bevan, Ingrid K. Svenson, Felicia Lennon Graham, Perry C. Gaskell, Andrew Dearlove, Margaret A. Pericak-Vance, David C. Rubinsztein, and Douglas A. Marchuk. A Kinesin Heavy Chain (KIF5A) Mutation in Hereditary Spastic Paraplegia (SPG10). *The American Journal of Human Genetics*, 71(5):1189–1194, nov 2002.

[48] Kai Y Soo, Manal Farg, and Julie D. Atkin. Molecular Motor Proteins and Amyotrophic Lateral Sclerosis. *International Journal of Molecular Sciences*, 12(12):9057, dec 2011.

[49] Nathan P. Wells, Guillaume A. Lessard, Peter M. Goodwin, Mary E. Phipps, Patrick J. Cutler, Diane S. Lidke, Bridget S. Wilson, and James H. Werner. Time Resolved 3D Molecular Tracking in Live Cells. *Nano letters*, 10(11):4732, nov 2010.

[50] Evan P. Perillo, Yen-Liang Liu, Khang Huynh, Cong Liu, Chao-Kai Chou, Mien-Chie Hung, Hsin-Chih Yeh, and Andrew K. Dunn. Deep and high-resolution three-dimensional tracking of single particles using nonlinear and multiplexed illumination. *Nature Communications 2015 6:1*, 6(1):1–8, jul 2015.

[51] Cong Liu, Yen-Liang Liu, Evan P. Perillo, Andrew K. Dunn, and Hsin-Chih Yeh. Single-Molecule Tracking and Its Application in Biomolecular Binding Detection. *IEEE journal of selected topics in quantum electronics : a publication of the IEEE Lasers and Electro-optics Society*, 22(4):64–76, jul 2016.

[52] Christian Hellriegel and Enrico Gratton. Real-time multi-parameter spectroscopy and localization in three-dimensional single-particle tracking. *Journal of the Royal Society Interface*, 6(Suppl 1):S3, feb 2009.

[53] L Lanzanò and E Gratton. Orbital single particle tracking on a commercial confocal microscope using piezoelectric stage feedback. *Methods and Applications in Fluorescence*, 2(2):024010, may 2014.

[54] Sahl SJ, Leutenegger M, Hilbert M, Hell SW, and Eggeling C. Fast molecular tracking maps nanoscale dynamics of plasma membrane lipids. *Proceedings of the National Academy of Sciences of the United States of America*, 107(15):6829–6834, apr 2010.

[55] Adam E. Cohen. Control of nanoparticles with arbitrary two-dimensional force fields. *Physical Review Letters*, 94(11):1–4, 2005.

[56] Karl Otto Greulich. Manipulation of cells with laser microbeam scissors and optical tweezers: a review. *Reports on Progress in Physics*, 80(2):026601, dec 2016.

[57] Hiroshi Isojima, Ryota Iino, Yamato Niitani, Hiroyuki Noji, and Michio Tomishige. Direct observation of intermediate states during the stepping motion of kinesin-1. *Nature Chemical Biology*, 12(4):290–297, apr 2016.

[58] Swathi Sudhakar, Mohammad Kazem Abdosamadi, Tobias Jörg Jachowski, Michael Bugiel, Anita Jannasch, and Erik Schäffer. Germanium nanospheres for ultraresolution picotensiometry of kinesin motors. *Science*, 371(6530):eabd9944, feb 2021.

[59] Erik W. Grafarend and Joseph L. Awange. Applications of linear and nonlinear models: Fixed effects, random effects, and total least squares. *Applications of Linear and Nonlinear Models: Fixed Effects, Random Effects, and Total Least Squares*, 9783642222:552–554, jul 2012.

[60] Anupama J. Thubagere, Wei Li, Robert F. Johnson, Zibo Chen, Shayan Doroudi, Yae Lim Lee, Gregory Izatt, Sarah Wittman, Niranjan Srinivas, Damien Woods, Erik Winfree, and Lulu Qian. A cargo-sorting DNA robot. *Science*, 357(6356), sep 2017.

[61] Jing Wang, Daniel K. Schreiber, Nathan Bailey, Peter Hosemann, and Mychailo B. Toloczko. The Application of the OPTICS Algorithm to Cluster Analysis in Atom Probe Tomography Data. *Microscopy and Microanalysis*, 25(2):338–348, apr 2019.

[62] Ahmet Yildiz, Michio Tomishige, Ronald D. Vale, and Paul R. Selvin. Kinesin Walks Hand-Over-Hand. *Science*, 303(5658):676–678, jan 2004.

[63] Karel Svoboda, Christoph F. Schmidt, Bruce J. Schnapp, and Steven M. Block. Direct observation of kinesin stepping by optical trapping interferometry. *Nature 1993 365:6448*, 365(6448):721–727, 1993.

[64] Mark J. Schnitzer and Steven M. Block. Kinesin hydrolyses one ATP per 8-nm step. *Nature 1997 388:6640*, 388(6640):386–390, 1997.

[65] Karel Svoboda and Steven M. Block. Force and velocity measured for single kinesin molecules. *Cell*, 77(5):773–784, jun 1994.

[66] Masayoshi Nishiyama, Etsuko Muto, Yuichi Inoue, Toshio Yanagida, and Hideo Higuchi. Substeps within the 8-nm step of the ATPase cycle of single kinesin molecules. Technical report, 2001.

[67] Hongbiao Huang, Xiaoyan Zhang, Shujue Li, Ningning Liu, Wen Lian, Emily McDowell, Ping Zhou, Canguo Zhao, Haiping Guo, Change Zhang, Changshan Yang, Guangmei Wen, Xiaoxian Dong, Li Lu, Ningfang Ma, Weihua Dong, Q. Ping Dou, Xuejun Wang, and Jinbao Liu. Physiological levels of ATP negatively regulate proteasome function. *Cell Research 2010 20:12*, 20(12):1372–1385, aug 2010.

[68] C M Coppin, J T Finer, J A Spudich, and R D Vale. Detection of sub-8-nm movements of kinesin by high-resolution optical-trap microscopy. *Proceedings of the National Academy of Sciences*, 93(5):1913–1917, mar 1996.

[69] Jacob Kerssemakers, Jonathon Howard, Henry Hess, and Stefan Diez. The distance that kinesin-1 holds its cargo from the microtubule surface measured by fluorescence interference contrast microscopy. *Proceedings of the National Academy of Sciences*, 103(43):15812–15817, oct 2006.

[70] Nicholas R. Guydosh and Steven M. Block. Direct observation of the binding state of the kinesin head to the microtubule. *Nature 2009 461:7260*, 461(7260):125–128, aug 2009.

[71] Steven M. Block. Kinesin Motor Mechanics: Binding, Stepping, Tracking, Gating, and Limping. *Biophysical Journal*, 92(9):2986, 2007.

[72] DD Hackney. Evidence for alternating head catalysis by kinesin during microtubule-stimulated ATP hydrolysis. *Proceedings of the National Academy of Sciences of the United States of America*, 91(15):6865–6869, 1994.

[73] DD Hackney. Processive motor movement. *Science*, 316(5821):58–59, apr 2007.

[74] Stefan Hell and Ernst H. K. Stelzer. Properties of a 4Pi confocal fluorescence microscope. *Journal of the Optical Society of America A*, 9(12):2159, dec 1992.

Acknowledgment

Here I would like to thank all the people that helped me and supported me to make this PhD possible.

I want to thank Prof. Dr. Stefan Hell for giving me the opportunity to do my PhD in his lab and for providing my colleagues and me we with supervision and everything useful for our work that we could think about. I also want to thank him for challenging us to constantly have a goal in mind to direct the work we are doing. I want thank Prof. Dr. Joachim Spatz for taking the responsibility of being the second referee for my thesis. I would like to thank Prof. Dr. Selim Jochim and Prof. Dr. Ulrich Schwarz for being part of the examination board.

I want to thank Dr. Jade Cottam-Jones for her scientific guidance and for proof-reading my thesis.

I want to thank Dr. Johann Engelhardt for co-supervising and advising me over the course of my PhD.

I would like to thank Dr. Jessica Matthias for helping me with all her experience in various scientific matters, explaining me how to properly use protocols, preparing samples for our measurements and spending many hours proof-reading my thesis draft. I want to thank Lukas Scheiderer for investing many hours into developing the kinesin protocols and preparing the samples for our experiments.

Lots of thanks go to my office and setup partner Otto Wolff for building the setup with me, making essential contributions to the work presented in this thesis, challenging me to really think ideas until the end and teaching me a lot about Matlab.

Additionally I want to thank Mr. Michael Remmler, M.Sc. for his valuable input, the interesting experiments we carried out together and for being an exceptional acquaintance.

Paying due respect I want to thank the other physics boys Julian Rickert and Marcus Held. Physical discussions were always interesting and fruitful with you guys.
Especially I want to thank you for the great times we had together, be it at the Tischkicker, on the roof terrace of the administration building or at the Heidelberger Schloss.

Now, I also want to thank all members of the Disc-Golf-Treff Ochsenkopf Heidelberg n.e.V.

I want to thank the current and former members of the ON department, Ricky, Ayse, Lukas H., Jonas, Viktor, Elisa, Clara, Alena, Angel, Jasmine, Mariano, Alexey, Rifka, Felix, Fabi and Jonas M. for being an awesome group. I learned at lot from you and often when I had a phase of low motivation because of the scientific side of my PhD, knowing to have such a great group of people to fall back on helped me regain my motivation.

I want to thank the colleagues at the mechanical workshop, especially Martin Lukat and Daniel Berndt for managing to build all the constructions that I produced in CAD. I also would like to thank Chris Roome and the whole IT department for their help with everything computer and file server related.

I want to thank some more or less public figures that inspired or motivated me and therefore helped finish my PhD: Cd.Chris Hadfield, Robert Pantano, Willhelm Blumberg and Ryan Holiday.

I want to thank my former flatmates and friends Jojo, Bene, Sepp, Krami, Philma, Tim, Carlo and Carlos for all the great times we had and all the support you gave me during my PhD.

Finally, I want to thank my family for supporting me. I knew you always had my back which gave me strength to finish my PhD. I want to thank Rina for all her love and picking me up when I was down from the setbacks during this time.